A new twist on black holes: the role of black hole spin in galaxy formation.

Nikolaos Fanidakis

Abstract

We study the coevolution of black holes (BHs) and their host galaxies through cosmic time. The calculation is embedded in the GALFORM semi-analytic model which simulates the formation and evolution of galaxies in a cold dark matter (CDM) universe. The BH and galaxy formation models are coupled: during the evolution of the host galaxy, hot and cold gas are added to the BH by flows triggered by halo gas cooling, disc instabilities and galaxy mergers. This builds up the mass and spin of the BH, and the resulting accretion power regulates gas cooling and subsequent star formation. Using the Blandford–Znajek mechanism for jet production to calculate the jet power, our model reproduces the radio loudness of radio galaxies, LINERS and Seyferts, suggesting that the jet properties of active galactic nuclei (AGN) are a natural consequence of *both* the accretion rate onto *and* the spin of the central BH. The model also reproduces the observed luminosity functions (LF) of AGN (optical, soft and hard X-ray, and bolometric) for a wide range of redshifts ($0 < z < 6$). We find downsizing in the AGN population, in terms of the differential growth with redshift of the space density of faint and bright AGN. This arises naturally from the interplay between the different accretion channels that drive the growth of BHs. The predictions of our model are extended to $6 < z < 20$ to study the early growth of BHs. Our model predicts that the first 10^8 $\mathrm{M}_\odot$ BHs appear at $z = 14$, along with the first luminous quasars. Finally, we explore the dependence of AGN activity and luminosity on environment. We find that quasars inhabit haloes with masses $10^{12} - 10^{13}$ $\mathrm{M}_\odot$. Quasar activity in more massive haloes in suppressed due to AGN feedback. In contrast, radio galaxies occupy the centres of the most massive haloes. Our model represents the first consistent demonstration that the phenomenology and evolution of AGN can be naturally explained by the coeval evolution of galaxies and BHs, coupled by AGN feedback, in a CDM universe.

A new twist on black holes: the role of black hole spin in galaxy formation

by Nikolaos Fanidakis

A thesis submitted to the University of Durham
in accordance with the regulations for
admittance to the Degree of Doctor of Philosophy.

Department of Physics
University of Durham
December 2010

Contents

List of Figures

List of Tables

Declaration

The work described in this thesis was undertaken between 2007 and 2010 while the author was a research student under the supervision of Prof. Carlos Frenk and Prof. Carlton Baugh in the Department of Physics at the University of Durham. This work has not been submitted for any other degree at the University of Durham or any other University.

Chapter 2 has been submitted in the form of a paper and accepted for publication

- N. Fanidakis, Baugh C. M., Benson A. J., Bower R. G., Cole S., Done C., Frenk C. S., "Grand unification of AGN activity in the ΛCDM cosmology", MNRAS, 1547, 2010

The first three sections from Chapter 2 have also been published as conference proceedings

- N. Fanidakis, C. M. Baugh, S. Cole, C. S. Frenk, "Black hole spin evolution in hierarchical cosmologies", Journal of Physics Conference Series, 189, 012013, 2009

Chapter 3 has been submitted in the form of a paper

- N. Fanidakis, Baugh C. M., Benson A. J., Bower R. G., Cole S., Done C., Frenk C. S., Hickox R. C., Lacey C., Lagos C. del P., "The evolution of AGN across cosmic time: what is downsizing?", MNRAS submitted

Chapter 4 has been submitted in the form of a paper

- N. Fanidakis, Baugh C. M., Benson A. J., Bower R. G., Cole S., Done C., Frenk C. S., "On the nature of the first quasars", MNRAS submitted

Acknowledgements

I am heartily thankful to my supervisors, Carlos Frenk and Carlton Baugh, whose encouragement and support from the initial to the final level enabled me to develop an understanding of the subject. This dissertation would not have been possible without their perpetual enthusiasm and immense knowledge.

I also owe my deepest gratitude to my collaborators Shaun Cole, Richard Bower, Chris Done, Cedric Lacey and Ryan Hickox for giving me the opportunity to work with them. Their assistance and guidance in getting my research career started was truly precious. Furthermore, I would like to thank Ian Smail and Andrew King (my thesis committee members) for their insightful comments and hard questions during my thesis examination.

I am also very grateful to the European Commissions Framework Programme 6, for funding my research through a Marie Curie Early Stage Training fellowship.

My friends and colleagues in Durham have my gratitude for being so wonderful. In particular, I would like to thank Claudia Lagos, Nikos Nikoloudakis, Raul Angulo, Elise Jennings, Alex Merson, Gabriel Altay, Violeta Gonzalez, Ioannis Taxidis, Juan Gonzalez and Marios Garganourakis. Special thanks to Alvaro Orsi for the stimulating discussions about science and life, and for being such an amazing flatmate.

Last but not the least, I thank those closest to me: Violette Debarbouille for her love and support and my family for everything.

Chapter 1 | *Introduction*

1.1 Motivation

Reproducing the observed galaxy luminosity function (LF) is a *crucial* test for any galaxy formation model. The basic physical mechanisms that determine the shape of the LF were first described by Rees and Ostriker (1977) and White and Rees (1978). These studies showed that the break of the LF arises naturally from the long cooling time of the gas in very massive haloes. With this physics, early semi-analytic models of galaxy formation accounted successfully for the shape of the LF. However, these models required a very low baryon density of $\Omega_{\rm b} \simeq 0.02$, almost half of that indicated by WMAP (Spergel et al., 2003, 2007; Sánchez et al., 2006). Assuming a WMAP cosmology, the sharp cut-off in the galaxy LF can only be explained if cooling in massive halos is strongly suppressed.

Recent observations have established that supermassive black holes (SMBHs) are likely to reside at the centres of all galactic spheroids (Richstone et al., 1998). Remarkably these observations show that the mass of the central SMBH and host spheroid are tightly correlated: the mass of the black hole (BH) is usually estimated to be a thousandth of the mass of the stars in the spheroid (the $M_{\rm BH} - M_{\rm Bulge}$ relation, Magorrian et al. 1998; McLure and Dunlop 2002b; Marconi and Hunt 2003; Häring and Rix 2004. The mass of the BH has been found to correlate also with the stellar kinematics (the $M_{\rm BH} - \sigma_\star$ relation, where $\sigma_\star$ is the stellar velocity dispersion, Ferrarese and Merritt 2000; Gebhardt et al. 2000; Tremaine et al. 2002 and luminosity of the bulge (the $M_{\rm BH} - L_{\rm Bulge}$ relation: McLure and Dunlop 2002b; Wandel 2002; Bentz et al. 2009). These relations strongly suggest that the growth of SMBHs and galactic bulges are driven by common physical processes.

In this framework, active galactic nuclei (AGN) are thought to represent a natural

stage in the evolution of galaxies in which the SMBH is growing prodigiously through accretion of gas via a radiatively efficient disc (Hopkins et al. 2005, Di Matteo et al. 2005). However, AGN release enormous amounts of energy to their surroundings, in the form of jets or outflows (King, 2010). Such feedback provides a natural mechanism for heating the gas in haloes and preventing cooling. By implementing the effects of AGN feedback in galaxy formation models the observed break in the LF can be reproduced (Croton et al. 2006, Bower et al. 2006, Lagos et al. 2008).

1.2 BHs and the nature of AGN

The solutions of the Einstein-Maxwell field equations are subject to the no-hair theorem which states that a BH can be completely characterised by only three classical parameters: the mass-energy, $M_{\rm BH}$, the angular momentum, J and the electric charge, Q. All other information is hidden from external observers by the event horizon of the BH. Therefore, BHs can be considered as the simplest astrophysical objects. BH solutions to the field equations of astrophysical relevance are usually considered to be the Schwarzschild and Kerr. Schwarzschild BHs are spherically symmetric and non-rotating, while Kerr BHs are axially symmetric and rotating. Since the Schwarzschild BH is simply the limiting case of zero rotation, and also as all astrophysical bodies are expected to have some angular momentum, we will refer only to the Kerr solution hereafter. Astrophysical BH candidates span a wide range of masses: from a few $\rm M_{\odot}$ (with $\rm M_{\odot}$ being the mass of the Sun, $\rm M_{\odot} = 1.98 \times 10^{30}\,Kg$) in galactic X-ray binaries to $10^6 - 10^{10}$ $\rm M_{\odot}$ in AGN. The latter mass range usually refers to SMBHs.

An important quantity associated with every BH is the Eddington luminosity,

$$L_{\rm Edd} = \frac{4\pi G M_{\rm BH} m_{\rm p} c}{\kappa} = 1.4 \times 10^{46} \left(\frac{M_{\rm BH}}{10^8\ \rm M_{\odot}} \right)\ {\rm erg\,s^{-1}}, \tag{1.1}$$

where $\kappa \sim 0.3$ cm^{2}g^{-1} is the electron scattering opacity and $m_{\rm p}$ is the proton mass. The Eddington luminosity has an associated accretion rate which is expressed as

$$\dot{M}_{\rm Edd} = L_{\rm Edd}/\epsilon c^2, \tag{1.2}$$

where ϵ is the accretion efficiency and c is the speed of light. This is the accretion rate at

which the BH radiates at the Eddington luminosity. The accretion efficiency is assumed to be determined by the spin of the BH (Novikov & Thorne 1973). It is convenient to express the physical accretion rate, $\dot{M}$, in units of the Eddington accretion rate, $\dot{m} \equiv \dot{M}/\dot{M}_{\rm Edd}$, in order to introduce a dependence on the BH mass.

The main concepts of a radiatively-efficient accretion disc are reviewed by Balbus & Hawley (1998). In brief, given that the accreting gas has formed a geometrically thin disc, as gas parcels spiral in towards the BH the strong gravitational gradient gives rise to intense frictional heating of the flowing material. Assuming that the dissipated energy is radiated away as a black body spectrum, the maximum temperature of an accretion disc scales as $M_{\rm BH}^{-1/4}$ (Shakura & Sunyaev 1973). For that reason, accretion onto SMBHs in AGN is characterised by a gas temperature of $kT << 1\,$keV (in contrast to stellar BH systems where the gas temperature can be as high as $1\,$keV) and thus, the emitted radiation is expected in the optical and UV part of the electromagnetic spectrum.

However, X-ray spectra from AGN display the presence of a power law component extending up to very high energies ($\sim 250 - 300\,$keV), beyond which the spectrum exponentially cuts off. The basic mechanism behind the power law continuum emission is believed to be the inverse Compton scattering of photons. This occurs when photons are scattered by electrons. Soft photons originating from the accretion disc interact with energetic electrons located close to the disc and have their energy amplified through subsequent scatterings. The origin of the electron distribution is still unclear. The current best-bet is an accretion-disc coronae, perhaps powered by magnetic processes, whose geometry is still uncertain. There are suggestions that the Comptonising corona enfolds the accretion disc (referred to as *sandwich* geometry) or that it has a sphere-like geometry embracing uniformly the BH (Churazov et al., 2001; Done and Kubota, 2006; Done et al., 2007; Schnittman and Krolik, 2010).

The radiative efficiency of an accretion disc is set by ϵ, which determines the fraction of the gravitational energy of the accreted gas that is converted into luminous energy. The value of ϵ is expressed as a function of BH spin, $a = J/M$, namely the angular momentum in units of BH mass (Novikov and Thorne, 1973). For a non-rotating BH ($a = 0$) the accretion efficiency equals 5.7%. If the BH has a non-zero spin the efficiency

increases significantly, reaching 42.3% for maximal rotation ($a = 1$). Hence, the spin of a BH can have a significant impact on the luminosity output of an AGN.

Apart from its significance in regulating the accretion-disc luminosity, the spin of a BH is considered to be the power source of the radio jets seen in AGN. AGN can be classified according to the importance of the radio emission from their nucleus. Objects showing strong emission at radio wavelengths belong to the *radio-loud* class, whereas those with negligible emission belong to the *radio-quiet* class. Radio-loud AGN are associated with large-scale radio-emitting jets while radio-quiet AGN show very little or negligible jet activity. Sikora et al. (2007) found that AGN have a bimodal distribution on the radio-optical luminosity plane, with radio-loud objects being about 10^3 times brighter in radio than radio-quiet objects (see also Kellermann et al. 1989; Xu et al. 1999). The origin of this dichotomy remains unknown. However, it has been proposed in many studies that a first step towards explaining why only some AGN launch prominent jets is to understand the nature of the central engine, the accreting BH.

AGN jets are believed to extract rotational energy from the BH and accretion disc through magnetic fields. Analytical studies have contributed to an understanding of the nature of the jets (Blandford & Znajek 1977; Macdonald & Thorne 1982; Blandford & Payne 1982; Begelman, Blandford & Rees 1984), but a breakthrough has come recently from magneto-hydrodynamical (MHD) simulations of the accretion flow. These self-consistently calculate the turbulent magnetic field dynamo which is the physical origin of the stresses which transport angular momentum outwards, allowing material to accrete onto the BH (Balbus & Hawley 1998). Embedding such calculations in a fully general relativistic framework produces relativistic jets from the accretion flow, and the collimation and jet power depend on the BH spin (McKinney & Gammie 2004; De Villiers et al. 2005; Hawley & Krolik 2006).

Thus, it now seems clear that the jet power depends on the vertical (poloidal) magnetic field strength close to the BH, but the simulations are still not yet at the level where they can predict this *ab initio* (e.g. Beckwith et al. 2008), so analytic models are still required. The most popular of these, the Blandford–Znajek (hereafter BZ) mechanism, uses the magnetic field as a means to tap the spin of the BH. This model suggests a strong

dependence of the jet power on the BH spin. Indeed, many authors have proposed spin as the physical parameter that determines the radio loudness of an AGN (see Wilson & Colbert 1995; Hughes & Blandford 2003). The spin paradigm, as this idea is called, offers a plausible theoretical explanation for the wide range of jet luminosities in AGN and could be the basis for understanding the observed dichotomy between radio-loud and radio-quiet AGN.

Alternatively, the radio–loud, radio–quiet switch may just be the physical state of the accretion flow. Stellar–mass BH binary systems in our galaxy show a clear spectral transition at about 1% of the Eddington luminosity ($L \sim 0.01 L_{\rm Edd}$) from a hot, optically thin accretion flow at low luminosities (e.g. an advection-dominated accretion flow or ADAF; Narayan & Yi 1994) to a cool, geometrically thin disc (Shakura & Sunyaev 1973) at higher luminosities (Esin et al. 1997, see e.g. the review by Done, Gierlinski & Kubota 2007). The collapse of the radio jet observed across this transition clearly relates to the large drop in pressure (and hence scale height, H) between the hot and cool flow (e.g. Fender, Belloni & Gallo 2004). Even without BH spin, this produces a clear dichotomy of radio properties (e.g. Jester 2005).

It seems most plausible that *both* these mechanisms, along with the mass accretion rate, affect jet power. The BZ mechanism has a *hidden* dependence on mass accretion rate and the scale height of the flow because the magnetic field strength close to the BH saturates, due to the dynamo, into rough equipartition with the pressure in the flow. This depends on the mass accretion rate for either the disc or the hot flow, but the pressure in the hot flow is much larger than that in the cool disc so the field strength and hence jet power abruptly drop at this transition (Meier 2001; 2002)

Sikora et al. (2007) used these ideas to interpret observations of radio galaxies and concluded that the data could be explained if the jet power depends on mass accretion rate, accretion model and spin. However, they also required a mass-spin correlation, such that the most massive BHs, which, according to the $M_{\rm BH} - M_{\rm bulge}$ relationship reside in massive elliptical galaxies, have higher spin than lower mass BHs, which reside in spirals. They speculated that this could occur through the hierarchical growth of structure, where the major mergers which give rise to giant elliptical galaxies trigger

large amounts of gas accretion with a given angular momentum direction onto the BH, spinning it up to the maximal value. In contrast, spiral galaxies have not experienced a recent major merger, and grow mainly through smooth accretion and multiple minor mergers with gas with randomly oriented angular momentum, resulting in low spin and hence weak jet luminosities.

Some of these ideas have recently been explored by Berti and Volonteri (2008), using simplified models, where BHs grow via accretion of gas and BH-BH mergers. Berti and Volonteri (2008) studied the cosmological evolution of BH spin and find that successive mergers during the evolution of BHs result in a population of rotating BHs with $a \sim 0.7$. When considering also the effect of accretion the final spin distributions seem to be solely determined by the manner in which the gas is accreted. If accretion occurs via an aligned accretion disc (Volonteri et al., 2007) the resulting BH spin distribution is characterised by very high spins, $a \sim 0.9$. In contrast, if the gas is accreted via many short-lived, uncorrelated accretion events (King et al., 2005, 2008) then BH spins tend to be modestly low, $a \sim 0.2$. In a more sophisticated approach, (Lagos et al., 2009) implemented the Berti and Volonteri (2008) recipes in their semi-analytic galaxy formation model in order to provide more robust correlations between BH spin and host galaxy properties. Lagos et al. obtain a strong BH mass–spin correlation: more massive BHs tend to have higher spins than less massive BHs. Hence, since massive BHs tend to inhabit more massive galaxies, their model suggests a possible correlation between galaxy morphology and BH spin.

1.3 Coupled BH-galaxy formation models

The study of the cosmological evolution of BHs in galaxy formation models has been a very active field of research in the last decade. The enigmatic nature of the observed BH scaling relations has motivated numerous studies. These studies employ several techniques, such as semi-analytics and hydrodynamical simulations to model BH evolution and the associated AGN activity in the standard Λ cold dark matter (CDM) model of galaxy formation. The first generation of galaxy formation models has been devised

which link the properties and evolution of galaxies to the growth of their central BH. The energy radiated during AGN activity triggered by accretion onto the BH regulates the amount of gas that cools in the host dark matter (DM) halo (Dalla Vecchia et al., 2004; Springel et al., 2005a; Croton et al., 2006; Bower et al., 2006; Hopkins et al., 2006; Thacker et al., 2006; Somerville et al., 2008; Lagos et al., 2008). As a consequence, the energy feedback which accompanies the growth of BHs regulates star formation, and hence the number of bright galaxies. Similarly, energy feedback from AGN is a key ingredient in determining the X-ray properties of the intracluster medium (Bower et al., 2008; McCarthy et al., 2010). These studies suggest that not only are AGN an important component of the Universe, they are also seem to play a key role in the evolution of their host galaxies.

So far, the models have invoked AGN feedback to control the formation of bright galaxies without considering the implied consequences for the AGN population. By extending the model to predict emission from AGN, much tighter constraints are placed on the amount of AGN activity. Early surveys demonstrated that quasi-stellar objects (QSOs) undergo significant evolution from $z \sim 0$ up to $z \sim 2 - 2.5$ (Schmidt and Green, 1983; Boyle et al., 1988; Hewett et al., 1993; Boyle et al., 2000). Beyond $z \sim 2$, the space density of QSOs starts to decline (Warren et al., 1994; Schmidt et al., 1995; Fan et al., 2001; Wolf et al., 2003). Recently, there has been much progress in pinning down the evolution of faint AGN in the optical. Using the 2-degree-field (2dF) QSO Redshift survey, the LF was probed to around one magnitude fainter than the break of the LF at $z \sim 2$ (2QZ, Croom et al., 2001, 2004). This limit was extended by the 2dF-SDSS luminous red galaxy and QSO (2SLAQ) survey (Richards et al., 2005; Croom et al., 2009a). The estimate of the LF from the final 2SLAQ catalogue reached $M_{b_{\rm J}} \simeq -19.8$ at $z = 0.4$ (Croom et al., 2009b). With the 2SLAQ LF, Croom et al. (2009b) demonstrated that in the optical, faint quasars undergo mild evolution, with their number density peaking at lower redshifts than is the case for bright quasars (see also Bongiorno et al., 2007).

Faint AGN can be selected robustly in X-rays (Hasinger et al., 2001; Giacconi et al., 2002; Alexander et al., 2003; Barcons et al., 2007, see also the review by Brandt and Hasinger 2005), which means that a wider range of AGN luminosity can be probed in

X-rays than is possible in the optical. This permits the study of the evolution of a wider variety of AGN in addition to QSOs (e.g., Seyfert galaxies) and thus provides a more representative picture of the various AGN populations. The evolution of the AGN LF in X-rays has been investigated by many authors by employing data from the *Chandra*, *ASCA*, *ROSAT*, *HEAO*-1 and *XMM-Newton* surveys (Miyaji et al., 2001; La Franca et al., 2002; Cowie et al., 2003; Fiore et al., 2003; Ueda et al., 2003; Barger et al., 2005; Hasinger et al., 2005). These studies show that in both soft ($0.5 - 2\mathrm{keV}$) and hard ($2 - 10\mathrm{keV}$) X-rays, faint AGN are found to evolve modestly with redshift. In contrast, bright AGN show strong evolution, similar to that seen for quasars in the optical. In addition, observations in soft X-rays suggest that the comoving space density of bright AGN peaks at higher redshifts ($z \sim 2$) than faint AGN ($z < 1$, Hasinger et al., 2005).

The differential evolution of bright and faint AGN with redshift has been described as *downsizing* (Barger et al., 2005; Hasinger et al., 2005). This implies that AGN activity in the low-z universe is characterised by high-mass BHs accreting at low rates or low-mass BHs growing rapidly. Hopkins et al. (2005b) proposed that the faint end of the LF is composed of high mass BHs experiencing quiescent accretion (see also Hopkins et al., 2005a,b; Babić et al., 2007). The bright end, on the other hand, in this picture corresponds to BHs accreting near their Eddington limit. In the Hopkins et al. model, quasar activity is short-lived and is assumed to be driven by galaxy mergers (Di Matteo et al., 2005).

The mass of accreting BHs can be estimated using the spectra of quasars. The BH mass in quasars is calculated using empirical relations derived from optical or UV spectroscopy. In particular, mass-scaling relations between the widths of different broad emission lines and continuum luminosities that have been calibrated against reverberation mapping results (Vestergaard, 2002; Vestergaard and Peterson, 2006) have allowed BH mass estimates in several large, unobscured (type-1) quasar samples. When translating quasar luminosities into BH masses using the width of broad lines, a similar downsizing is seen in BH mass (Vestergaard and Osmer, 2009; Kelly et al., 2010), suggesting that the most massive BHs ($M_{\mathrm{BH}} > 10^9\,\mathrm{M}_\odot$) were already in place at $z > 2$, whereas the growth of the less massive ones is delayed to lower redshifts.

In addressing the observational estimation of the BH mass, it is important to dis-

cuss the effects of obscuration. AGN exhibit evidence of obscuration at both optical and soft X-ray wavelengths. The obscuration may be linked to the existence of a geometrical torus around the accretion disc whose presence is invoked in the AGN unification scheme (Antonucci, 1993; Urry and Padovani, 1995) or to intervening dust clouds related to physical processes within the host galaxy (Martínez-Sansigre et al., 2005), such as star formation (SF) activity (Ballantyne et al. 2006a, but also Goulding and Alexander 2009). As a consequence, a large fraction of AGN could be obscured and thus missing from optical and soft X-ray surveys. Hence, when applying the scaling relations to estimate the mass of accreting BHs, the absence of obscured (type-2) quasars from the AGN samples may introduce significant biases into the inferred evolution of BH mass. Only hard X-rays can directly probe the central engine by penetrating the obscuring medium, therefore providing complete and unbiased samples of AGN (Ueda et al. 2003; La Franca et al. 2005; Barger et al. 2005). However, even in hard X-rays, a population of Compton-thick sources, namely AGN with hydrogen column densities exceeding $N_{\rm H} \simeq 10^{24}\,{\rm cm}^{-2}$, would still be missing (Comastri, 2004; Alexander et al., 2005, 2008; Goulding et al., 2010).

A further challenge faced by hierarchical model is to explain observations of high redshift quasars. Quasars are ideal for probing the evolution of the actively growing BH mass back into the early Universe since their high brightness allows them to be detected up to very high redshifts. The advent of large surveys such as the SDSS initiated the quest for finding very distant quasars in the Universe. The large size of SDSS and its ability to detect objects across five measured colour bands allowed the detection of quasars up to $z \sim 6$ (Fan et al., 2001, 2003, 2004; Jiang et al., 2009). Interestingly, the detection of $10^{48}\ {\rm erg\,s}^{-1}$ luminous quasars at $z \sim 6$ in the SDSS suggests the existence of $\sim 10^9\ {\rm M}_\odot$ BHs less than $1\,$Gyr after the Big Bang (Jiang et al., 2006; Kurk et al., 2007, 2009). Together with the quasars found in the Canada-France High-z Quasar Survey (CFHQS, Willott et al. 2005, 2010b) the total number of $z \sim 6$ quasars today amounts to 41 ($5.74 < z < 6.44$). Recently, Willott et al. (2010a) derived the first observation estimation of the $z \sim 6$ BH mass function (MF), providing compelling insight into the early evolution of these massive BHs.

The presence of the $\sim 10^9\ {\rm M}_\odot$ BHs imposes strong constraints on the BH evolution

in galaxy formation models. Many theoretical studies have tried to address how can enough BH mass be assembled such a short time after Big Bang. These studies suggest that the predicted $z = 6$ BH masses depend strongly on the nature of the initial mass of the BH seed. A wide range of suggestions and proposals can be found in the literature for the nature and initial mass of the BH seeds. The seeds could, for example, form from the direct collapse of pre-galactic gas discs at very high redshifts ($z > 20$, Koushiappas et al., 2004; Begelman et al., 2006; Lodato and Natarajan, 2006; Spaans and Silk, 2006; Volonteri et al., 2008) or they could be the remnants of the first stars (Population III) that form in the Universe (Volonteri and Rees, 2005; Shapiro, 2005). Many authors have also discussed the possibility that primordial BHs (Novikov et al., 1979), growing initially via the accretion of DM, could be viable candidates for the seeds of the massive BHs found today in the centres of galaxies (Mack et al., 2007).

Volonteri and Rees (2005) suggested an evolutionary scenario in hierarchical merger models invoking supercritical quasi-spherical accretion onto seed BHs with a flat initial MF in the mass range $20\ \mathrm{M}_\odot < \mathrm{M}_{\mathrm{BH,seed}} < 70\ \mathrm{M}_\odot$ and $130\ \mathrm{M}_\odot < \mathrm{M}_{\mathrm{BH,seed}} < 600\ \mathrm{M}_\odot$. In their model, the BHs in the most massive haloes can grow efficiently to masses $10^9\ \mathrm{M}_\odot$ by $z = 6$. Many authors have also addressed the importance of multiple mergers between seed BHs on the early build up of SMBHs (Haiman, 2004; Bromley et al., 2004; Shapiro, 2005; Volonteri and Rees, 2006; Li et al., 2007; Tanaka and Haiman, 2009). Sijacki et al. (2009), using hydrodynamical simulations, resimulated the most massive DM halo in the Millennium simulation (Springel et al., 2005b) with very high resolution in order to to study the growth of BHs at high redshifts. Their simulations show that in a hierarchical universe, $10^9\ \mathrm{M}_\odot$ BHs at $z = 6$ can be found in the most massive haloes given that the initial BH seeds have a relatively high mass of $M_{\mathrm{BH,seed}} \sim 10^5\ \mathrm{M}_\odot$. Such high mass seeds could be produced by the direct-collapse mechanism.

In spite of the theoretical models and suggestions in the literature, the formation and early growth of BHs is still a mystery. This motivates the search of quasars at redshifts greater than $z = 6$ to probe directly the first stages of BH evolution. Current and future infrared missions and surveys, whose scientific goal is to observe the most distant objects in the universe, will be essential for accomplishing this task. In particular, the James

Webb Space Telescope (JWST, to be launched in 2014-2015) will provide unique insight into the the first stars, galaxies and quasars. In addition, the Spitzer Warm Mission programme and ground-based near-IR surveys such as the UKIRT Infrared Deep Sky Survey(UKIDSS) and the Visible and Infrared Survey Telescope for Astronomy (VISTA) are expected to yield important information on the $z \sim 6 - 7$ Universe and also provide distant-quasar targets for more detailed follow-up with JWST.

In this thesis, we use a coupled galaxy-BH model to study the evolution of BHs and associated AGN. The calculation is embedded in the `GALFORM` semi-analytic model which simulates the formation and evolution of galaxies in a CDM universe. The model calculates the growth of BHs by accretion and mergers, their acquisition of spin and their accretion rates. We incorporate several accretion and jet-launching models from the literature which allows us to perform a quantitative comparison with observations of AGN. Our predictions reproduce the observed LFs in the radio, optical, X-ray and bolometric bands and the optical-radio properties of AGN in the local Universe. This thesis explicitly demonstrates that hierarchical cosmological models for galaxy formation and evolution are able to provide a robust framework in which AGN can be studied. The ability of our galaxy formation model to reproduce the evolution and diversity of the AGN populations strengthens the powerful capabilities of semi-analytic modelling and shows that the level of AGN activity implied by AGN feedback is compatible with observations.

1.4 Thesis outline

The outline of the remainder of this thesis is as follows. In Chapter 2 we calculate the growth of BHs by accretion and mergers, their acquisition of spin and their accretion rates within a coupled BH-galaxy formation model in a CDM cosmology and we explore the importance of BH spin in determining the radio loudness of AGN. The good agreement of our theoretical predictions with the observations motivates us to propose a *grand unification of AGN activity*, in which the accretion flow and jet luminosity determine the AGN type through the BH mass, spin and mass accretion rate. In Chapter 3 we present a study of the AGN evolution in the redshift range $0 < z < 6$ within the same

coupled BH-galaxy formation model. We show predictions for the evolution of the LF of AGN in the optical, X-rays and bolometric bands and provide a robust framework for understanding the downsizing of AGN within a self-consistent model. In Chapter 4 we extend the predictions of our model to redshifts $6 < z < 20$ to unravel the properties of the first BHs and associated quasars. In this chapter, we explore the early evolution of BH mass and determine the epoch of the *first quasars*. In Chapter 5 we present a clustering analysis to elucidate the dependence of AGN activity and luminosity on environment. We show the predictions of our model for the clustering of quasars and radio galaxies and explore the typical DM environments in which these AGN are found. Finally, in the epilogue, Chapter 7, we summarise and discuss the findings of this thesis and briefly present ideas for future projects.

Chapter 2

AGN radio loudness and the spin paradigm

2.1 Introduction

In this chapter we describe the cosmological processes that initiate and regulate the growth of SMBHs and outline the modelling of the spin evolution due to gas accretion and mergers in hierarchical cosmologies. The calculation of the joint evolution of BHs and galaxies is self-consistent and incorporates several accretion and jet-launching models from the literature which allows us to perform a quantitative comparison with observations of the radio loudness of AGN.

We use the `GALFORM` semi-analytical galaxy formation code (Cole et al. 1994, 2000, also Baugh et al. 2005; Bower et al. 2006; Font et al. 2008) and the extension to follow the evolution of BH mass introduced by Malbon et al. (2007). `GALFORM` simulates the formation and evolution of galaxies and BHs in a hierarchical cosmology by modelling a wide range of physical processes, including gas cooling, AGN heating, star formation and supernovae (SN) feedback, chemical evolution, and galaxy mergers.

Our starting point is the Bower et al. (2006) galaxy formation model. This model invokes AGN feedback to suppress the cooling of gas in DM haloes with quasi-static hot atmospheres and has been shown to reproduce many observables, such as galaxy colours, stellar masses and LFs remarkably well. The model adopts a BH growth recipe based on that introduced by Malbon et al. (2007), and extended by Bower et al. (2006). In brief, during starbursts triggered by a disc instability (Efstathiou et al., 1982) or galaxy merger, the BH accretes a fixed fraction, $f_{\rm BH}$, of the cold gas that is turned into stars

in the burst, after taking into account SN feedback and recycling. The value of $f_{\rm BH}$ is chosen to fit the amplitude of the local observed $M_{\rm BH} - M_{\rm bulge}$ relation. In addition to the cold gas channel, quiescent inflows of gas from the hot halo during AGN feedback also contribute to the mass of the BH (see White and Frenk, 1991; Cole et al., 2000; Croton et al., 2006, for the cooling properties of gas in haloes). Finally, mergers between BHs, which occur when the galaxies which host the BHs merge, redistribute BH mass and contribute to the build up of the most massive BHs in the universe. We describe in detail the modelling of BHs in GALFORM in Section 2.2.

For the purposes of this analysis we introduce an updated version of the Bower et al. 2006 model. The changes relative to the original model are the following. Firstly, the fraction, $f_{\rm Edd}$, of the Eddington luminosity of an accreting SMBH that is available for heating the halo during an episode of AGN feedback is set to 0.01 (Bower et al. 2006 use, $f_{\rm Edd} = 0.04$[1]). Secondly, in starbursts triggered by galaxy mergers or disc instabilities, we assume that the fraction, $f_{\rm BH}$, of the cold gas available to turn into stars that is accreted onto the BH is 0.01 (Bower et al. 2006 use $f_{\rm BH} = 0.017$). These changes are introduced to improve the modelling of BHs and *do not* affect the fundamental predictions of the Bower et al. model. A correction to the amount of gas that is accreted is applied in order to account for the fraction of gas that turns into radiation during the accretion process. Finally, we note that we do not take into account BH ejection via gravitational-wave recoils during galaxy mergers (Merritt et al., 2004). This omission is not expected to have a significant impact on the evolution of BH mass in our model (Libeskind et al., 2006).

GALFORM calculates a plethora of properties for each galaxy including disc and bulge sizes, luminosities, colours and metallicities to list but a few. In this analysis, we are primarily interested in the properties that describe the BHs. Specifically, we output the BH mass, $M_{\rm BH}$, the amount of gas accreted in a starburst or during the hot-halo mode, $M_{\rm acc}$, the time that has passed since the last burst of star formation experienced by the

[1]Note that due to an error in Bower et al. (2006), cooling luminosities were overestimated by a factor of 4π. Thus, while the paper quotes the efficiency parameter $f_{\rm BH}$ as 0.5, this should have been $0.5/4\pi = 0.04$. With this correction, the rest of the parameters and results are unchanged.

host galaxy and the BH spin (discussed in more detail below). The time since the last burst is necessary to determine the beginning of the active phase of BH growth in the starburst mode.

In the following sections we describe in detail how we model the BH mass and spin in GALFORM. Our simulations study the cosmological mass and spin evolution of SMBH seeds of a total of $\sim 4.2 \times 10^6$ galaxies identified in the Millennium N-body simulation (co-moving volume of $1.25 \times 10^8\ h^{-3}$ Mpc^3) from redshift 127 to redshift zero. Here h is defined by $H_0 = h \times 100$ km s^{-1} Mpc^{-1}, where H_0 is the Hubble constant at redshift zero. The cosmology adopted in the simulations is $h = 0.70$, $\Omega_{\rm m} = 0.25$, $\Omega_{\rm b} = 0.045$, $\Omega_\Lambda = 0.75$ and $\sigma_8 = 0.9$[2].

2.2 The growth of BHs in GALFORM

The evolution of BH mass fits naturally in the CDM model of galaxy formation (Kauffmann and Haehnelt 2000; Malbon et al. 2007), where structures grow hierarchically. Small structures form first, then evolve through mergers into large ones. In the event of a galaxy merger, the less massive galaxy (satellite) sinks into the gravitational potential of the massive central galaxy as a result of dynamical friction (Binney & Tremaine 1987). In our model we assume that if the mass of the satellite galaxy is comparable to that of the central galaxy, the merger disrupts the galaxies and resulting in the formation of an elliptical galaxy (major merger). This event is accompanied by a burst of star formation as the available cold gas from both progenitors is transferred to the centre and transformed into stars. Some of this cold gas reservoir feeds the central SMBH. An additional process of cold gas accretion that contributes to the SMBH mass is the collapse of galaxy discs triggered by dynamical instabilities (Efstathiou et al. 1982). When the self-gravity of the galactic disc becomes sufficiently large, the disc equilibrium is disrupted resulting in the formation of a bar which enables gas to be transferred towards the centre as the disc. A fraction of that gas is directly fed into the BH through an accretion disk

[2] $\Omega_{\rm m}$, $\Omega_{\rm b}$ and Ω_Λ express the present density of the baryonic, total matter and dark energy components of the Universe relative to the critical density ($\rho_{\rm crit} = 3H^2/8\pi G$). σ_8 measures the rms mass fluctuations in spheres of radius $8\ h^{-1}$ Mpc linearly extrapolated to the present day.

and powers an AGN (Lynden-Bell 1969), while the rest undergoes star formation. For highly efficient accretion activity, the disc/BH system dominates the energetics of the nucleus, and the galaxy becomes visible as a quasar.

The consequence of a minor merger, namely, the accretion of satellites of low mass compared to the central galaxy, is usually less dramatic. During a minor merger in our model, cold gas and stellar content of the satellites are added to the central galaxy, and a merger-driven starburst may supply fresh gas to the central BH.

SMBHs acquire part of their mass merging with other SMBHs. The formation of a BH-BH binary and the subsequent coalescence of the BHs is a natural evolutionary stage for a SMBH if the host galaxy experiences a merger. As the galaxies merge, we assume that the SMBHs sink to the centre by dynamical friction from distant stars or by viscous effects from the surrounding gas. The transition to a bound binary state after the galaxy merger is an open issue (Milosavljević and Merritt 2001). However, it is believed that once the separation of the two BHs becomes small enough, gravitational radiation carries away the remaining angular momentum of the binary. The removal of energy from a SMBH binary due to gravitational wave emission leads to a gradual shrinkage of the relative separation of the two members. There is a point where the eccentricity reaches zero and the orbit circularises. At that time, the two BHs are very close to each other, and gravitational waves are emitted copiously. The radiated energy is so large, that two SMBHs, which are a few AU apart, lose all their potential energy within a couple of minutes and inevitably coalesce. After the coalescence is complete the binary enters the *ringdown* phase, where the merged members settle into a quiescent remnant hole.

A third channel for SMBH growth in our model is provided by diffuse gas in DM haloes undergoing quasi-hydrostatic cooling. When a massive halo collapses gas is shock heated out to a radius comparable to the virial radius of the DM halo. These haloes have a cooling time that is longer than the free-fall time of the gas and, thus, the gas settles into a quasi-static atmosphere surrounding the galaxy rather than simply falling towards the centre (White and Frenk 1991). This atmosphere – the "hot halo" regime – is in pressure supported hydrostatic equilibrium and extends beyond the virial

radius of the DM halo. The galaxy is then supplied with cold gas by cooling flows at the disc centre, which also feed the central SMBH.

The formation of massive hot haloes would lead to the growth of very massive galaxies unless a heating mechanism regulates the cooling flow. Bower et al. (2006) invoke energy injection from the central SMBH during the quiescent accretion of gas from the hydrostatically supported hot halo (see also De Lucia et al. 2006; Cattaneo et al. 2007; Lagos et al. 2008). The cooling flow stops when the power from the SMBH is sufficient to offset the rate at which energy is being radiated away. Such energy feedback suppresses star formation due to the suppression of cooling flows and the subsequent drop in the gas reservoir.

Bower et al. adopt a BH growth model in which during a disc instability or galaxy merger, the BH accretes a fixed fraction of the gas available to turn into stars in the burst taking into account processes such as feedback and recycling in the galaxy (Malbon et al. 2007). The amount of gas deposited onto the BH is set by $f_{\rm Edd}$, which determines the fraction of the available gas reservoir for star formation that is accreted by the hole. The value of $f_{\rm Edd}$ is chosen to fit the normalisation of the local $M_{\rm BH} - M_{\rm bulge}$ relation.

To distinguish between the two accretion channels, we refer to the accretion triggered by disc instabilities and galaxy mergers as the *starburst mode* and the accretion from quasi-hydrostatic hot haloes as the *hot-halo mode*. These correspond to the "quasar" and "radio" modes, respectively, in the terminology used by Croton et al. (2006).

2.3 Astrophysical processes affecting BH spin evolution

SMBHs are expected to possess angular momentum $J_{\rm BH} = |a|GM_{\rm BH}^2/c$, where a is the spin parameter, $0 \leq |a| \leq 1$. The spin has a significant impact in the close vicinity of the BH. For example, it determines the efficiency for converting matter into radiation in an accretion disc (Novikov & Thorne 1973) and it is believed to influence the formation and direction of the radio jets in AGN (Blandford and Znajek 1977; MacDonald and Thorne 1982; Begelman et al. 1984). In addition, it is of special interest in the modelling of gravitational waves from BH-BH binaries (Merritt et al. 2005; Baker et al. 2006a, 2007;

Campanelli et al. 2007; Buonanno et al. 2007). For an introduction to the physics of rotating BHs we refer the reader to Appendix 1.

The evolution of spin is closely related to the channels that contribute to the growth of the BH. Each mechanism for BH growth is associated with different spin evolution. For example, accretion of gas that co-rotates with the BH should spin up the hole (Bardeen 1970), whereas, the merger of two equal-mass non-spinning BHs results in a final spin of 0.69 (Baker et al. 2006b; Berti et al. 2007, Hinder et al. 2008). We explain below how these mechanisms that influence the spin of a BH are included in our model.

2.3.1 Gas accretion

After the SMBH seed forms at the centre of a galaxy, accretion usually initiates the growth era. We assume that an accretion disc is formed in the equatorial plane of the hole. As proposed by Lynden-Bell (1969), gas parcels in the disc gradually lose angular momentum due to viscous torques exerted by magnetic fields and drift radially inwards until they reach the inner edge of the accretion disc. The inner edge of the disc is usually taken as the location of the last stable orbit (LSO) around the BH. The LSO is a function of the hole's angular momentum and can be written as (Bardeen et al. 1972):

$$\hat{r}_{\rm lso} \equiv r_{\rm lso}/R_{\rm g} = \{3 + Z_2 \pm [(3 - Z_1)(3 + Z_1 + 2Z_2)]^{1/2}\}, \tag{2.1}$$

where the gravitational radius, $R_{\rm g}$, is defined as half of the Schwarzschild radius of the BH, $R_{\rm Schw} = 2R_{\rm g} = 2GM_{\rm BH}/c^2$, and Z_1, Z_2 are defined in terms of the spin, a, as

$$\begin{aligned} Z_1 &\equiv 1 + \left(1 - a^2\right)^{1/3} \left[(1 + a)^{1/3} + (1 - a)^{1/3}\right], \\ Z_2 &\equiv \left(3a^2 + Z_1^2\right)^{1/2}. \end{aligned} \tag{2.2}$$

Note that when the spin parameter has a negative sign the BH is counter-rotating with respect to the orbit of a particle around it. Then, for counter-rotating orbits ($-1 \leqslant a < 0$) $9 \leqslant \hat{r}_{\rm lso} < 6$ and, for co-rotating orbits ($0 < a \leqslant 1$), $6 < \hat{r}_{\rm lso} \leqslant 1$.

An important property is the binding energy of the gas at the LSO, defined as the difference between the rest energy of a gas parcel at infinity and its energy at the LSO as measured by an observer at infinity. If $\tilde{e}$ expresses the energy per unit rest mass, we can

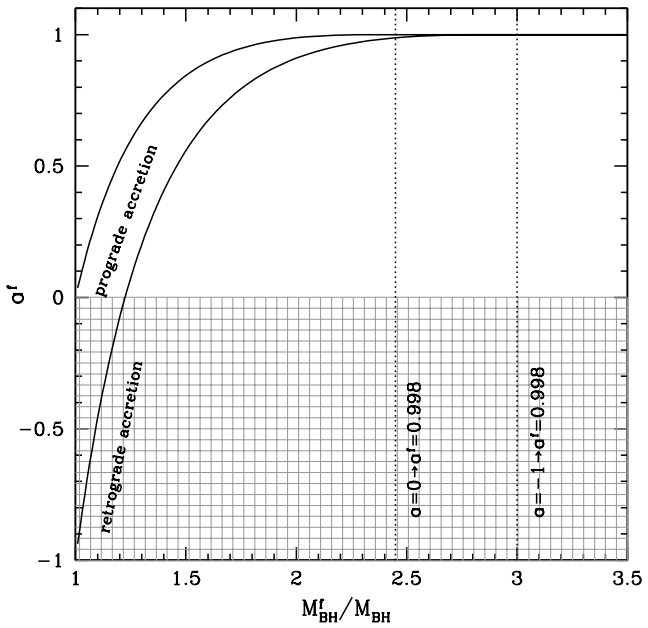

Figure 2.1: The final BH spin after the accretion of gas in a counter- and co-rotating configuration. The dotted lines indicate the final mass needed to spin up a non-rotating and maximally counter-rotating BH to $a^f = 0.998$.

define the binding energy as $1 - \tilde{e}/c^2$. This provides a simple relation for the accretion efficiency,

$$\epsilon \equiv 1 - \tilde{e}_{\rm lso}/c^2 = 1 - \sqrt{1 - \frac{2}{3}\frac{1}{\hat{r}_{\rm lso}}}, \tag{2.3}$$

(Novikov & Thorne 1973) which corresponds to the fraction of the energy released by matter spiralling in towards the BH through a succession of almost circular orbits. Eq. (2.3) shows that accretion of matter onto slowly rotating BHs has moderate efficiency. For non-rotating BHs ($a = 0$, $\hat{r}_{\rm lso} = 6$) this is just $1 - \sqrt{8/9}$ or 5.7%. However, for co-rotating matter around rapidly rotating BHs, the efficiency increases significantly reaching $1 - 1/\sqrt{3}$ or 42.3% as $a \to 1$. This sets an upper limit to the efficiency of the accretion onto BHs, a process obviously much more efficient than thermonuclear burning.

Once the gas reaches the LSO, we assume that it falls directly into the BH. In this way, the accretion carries into the BH the energy per unit mass, $\tilde{e}$, and angular momentum per unit mass, $\tilde{l}$, that the gas has at the LSO. Thus, accretion of a rest mass $\mathrm{d}M_0$ leads to a

change in the hole's total mass, $M_{\rm BH}$, and angular momentum, $J_{\rm BH}$, equal to,

$$\mathrm{d}M_{\rm BH} = (\tilde{e}_{\rm lso}/c^2)\mathrm{d}M_0, \;\; \mathrm{d}J_{\rm BH} = \tilde{l}_{\rm lso}\mathrm{d}M_0. \tag{2.4}$$

The change in the hole's spin induced by the accretion of dM_0 is governed by the differential equation

$$\frac{\mathrm{d}a}{\mathrm{d}\ln M_{\rm BH}} = \frac{1}{M_{\rm BH}}\frac{c^3}{G}\frac{\tilde{l}_{\rm lso}}{\tilde{e}_{\rm lso}} - 2a. \tag{2.5}$$

This was integrated by Bardeen (1970) using the explicit expressions for $\tilde{e}$ and $\tilde{l}$, resulting in the following solution,

$$a^{\rm f} = \frac{1}{3}\hat{r}_{\rm lso}^{1/2}\frac{M_{\rm BH}}{M_{\rm BH}^f}\left[1 - \left\{3\hat{r}_{\rm lso}\left(\frac{M_{\rm BH}}{M_{\rm BH}^f}\right)^2 - 2\right\}^{1/2}\right] \tag{2.6}$$

when $M_{\rm BH}^f/M_{\rm BH} \leq \hat{r}_{\rm lso}^{1/2}$. Here, $M_{\rm BH}^f$ and a^f are the final mass and spin parameter of the BH. If $M_{\rm BH}^f/M_{\rm BH} > \hat{r}_{\rm lso}^{1/2}$, then the final spin is always equal to unity. The expression in Eq. (3.6) governs the evolution of a during accretion from an initial state of a co-rotating or counter-rotating disc. According to this, a non-rotating BH will be spun up to a maximum rotation ($a = 1$, $\hat{r}_{\rm lso} = 1$) after increasing its mass by $1.44M_{\rm BH}$ (see Fig. 2.1). For a maximally rotating BH in a counter-rotating accretion disc ($a = -1$, $\hat{r}_{\rm lso} = 9$), an increase in mass of $2M_{\rm BH}$ is required in order for the BH to be spun down to $a = 0$ and subsequently spun up to maximum rotation. As implied by Eq. (3.6), further accretion onto the BH keeps a equal to unity.

Bardeen's calculations are limited to the process of angular momentum transport between the accreted matter and the BH, without taking into account any other processes. In fact, Thorne (1974) argued that the accretion disc radiates and that some of this radiation will be accreted by the hole. Capture of photons with angular momentum opposite to that of the BH will then produce a counteracting torque that prevents spin up beyond the limiting value of $a = 0.998$ ($\hat{r}_{\rm lso} = 1.23$, $\epsilon \simeq 0.32$). In addition, axial relativistic outflows of matter in the form of jets may have strong implications for the upper spin limit, since these outflows are accelerated by magnetic fields that are powered by the extraction of the rotational energy of the BH (Hawley & Krolik 2006; Benson & Babul 2009).

2.3.2 Gas accretion through a misaligned disc

In the general case where the accretion disc does not lie on the equatorial plane of the BH but has a random orientation relative to the angular momentum of the BH, the evolution of the spin is a complicated process. Following the discussion in King et al. (2005), we assume that a thin disc is inclined at some random angle θ relative to the orientation of the hole's angular momentum vector, $\boldsymbol{J}_{\rm BH}$. We denote the angular momentum of the disc as $\boldsymbol{J}_{\rm d}$ (see King et al. 2005 and Volonteri et al. 2007 for a discussion of the nature of $\boldsymbol{J}_{\rm d}$), and define the total angular momentum vector $\boldsymbol{J}_{\rm tot}$ as

$$\boldsymbol{J}_{\rm tot} = \boldsymbol{J}_{\rm BH} + \boldsymbol{J}_{\rm d}. \tag{2.7}$$

The angle θ between $\boldsymbol{J}_{\rm BH}$ and $\boldsymbol{J}_{\rm d}$ is defined such that $0 \leq \theta \leq \pi$; the values $\theta = 0$ and $\theta = \pi$ correspond to full alignment and anti-alignment respectively. $\boldsymbol{J}_{\rm tot}$ is a constant vector i.e. has fixed orientation as well as magnitude for a given accretion event. Its magnitude is given by

$$J_{\rm tot}^2 = J_{\rm BH}^2 + J_{\rm d}^2 + 2J_{\rm BH}J_{\rm d}\cos\theta. \tag{2.8}$$

We further introduce the angle θ_t as the angle between $\boldsymbol{J}_{\rm BH}$ and $\boldsymbol{J}_{\rm tot}$.

When the vectors $\boldsymbol{J}_{\rm BH}$ and $\boldsymbol{J}_{\rm d}$ are misaligned, the tilted orbits of the gas parcels in the accretion disc experience a torque due to the Lense–Thirring effect, which causes the plane of the accretion disc to precess about the rotational axis of the BH (Lense & Thirring 1918; Wilkins 1972; Bardeen & Petterson, 1975; Scheuer & Feiler, 1996). If viscosity is strong enough this can force the inner parts of the disc to rotate into the equatorial plane of the hole resulting in a "warped disc" (see Fig. 2.2).

The Lense–Thirring torque can be expressed as

$$\frac{\partial \boldsymbol{L}}{\partial t} = \boldsymbol{\Omega_{\rm p}} \times \boldsymbol{L}, \tag{2.9}$$

where $\boldsymbol{L}$ is the angular momentum per unit area of the disc and $\boldsymbol{\Omega_{\rm p}}$ is the precession rate and is given by

$$\boldsymbol{\Omega_{\rm p}} = \frac{2G\boldsymbol{J}_{\rm BH}}{c^2 R^3}, \tag{2.10}$$

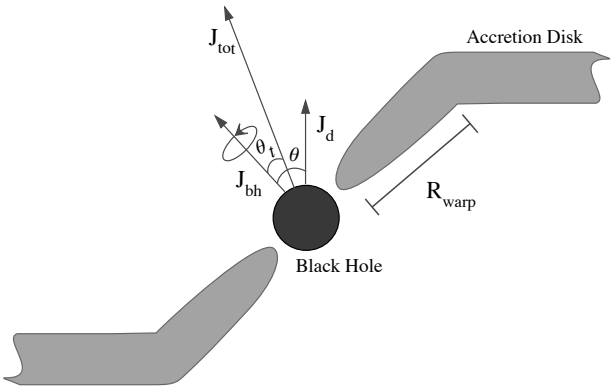

Figure 2.2: Schematic illustration of a warped accretion disc. $\boldsymbol{J}_{\rm BH}$ is the angular momentum of the BH ($|\boldsymbol{J}_{\rm BH}| = |a|GM_{\rm BH}^2/c$), $\boldsymbol{J}_{\rm d}$ is the angular momentum of the disc given by Eq. (2.19) and $\boldsymbol{J}_{\rm tot}$ represents the total angular momentum of the system, $\boldsymbol{J}_{\rm BH} + \boldsymbol{J}_{\rm d}$.

where R is the distance from the BH (Pringle 1992). The precession timescale is therefore defined as,

$$t_{\rm prec} \equiv \frac{2\pi}{\Omega_{\rm p}(R)}, \tag{2.11}$$

which is proportional to R^3 and thus is much shorter closer to the BH. Other timescales relevant to this problem are the viscous timescales of accretion, t_{ν_1}, and warp propagation, t_{ν_2},

$$t_{\nu_{1,2}} \equiv \frac{R^2}{\nu_{1,2}(R)}. \tag{2.12}$$

Here, ν_1 and ν_2 are the kinematic viscosities acting on velocity gradients parallel and normal to the plane of the disc respectively. The balance between the timescales $t_{\rm prec}$ and t_{ν_2} determines whether the Lense – Thirring torque is able to align the inner disc with the spin axis. The condition for alignment is $t_{\rm prec} \lesssim t_{\nu_2}$ (Natarajan & Armitage 1999). In other words, the disc will be aligned with the spin at radii where the precession timescale is much shorter than the timescale of radial diffusion of the warp. The characteristic radius, $R_{\rm warp}$, of the aligned part of the disc follows from the condition $t_{\rm prec} = t_{\nu_2}$.

The evolution of $\boldsymbol{J}_{\rm BH}$ and $\boldsymbol{J}_{\rm d}$ during the precession is determined by the conditions (King et al. 2005):

$$\frac{\rm d}{{\rm d}t} J_{\rm BH}^2 = 0, \quad \frac{\rm d}{{\rm d}t} J_{\rm d}^2 \leq 0 \quad \text{and} \quad \frac{\rm d}{{\rm d}t} \cos\theta_t \geq 0. \tag{2.13}$$

As can be inferred by the first two conditions, the magnitude of $\boldsymbol{J}_{\rm BH}$ remains constant while the angle θ_t decreases with time, which implies that $\boldsymbol{J}_{\rm BH}$ always aligns with $\boldsymbol{J}_{\rm tot}$. In contrast, $\boldsymbol{J}_{\rm d}$ decreases in magnitude as $\boldsymbol{J}_{\rm BH}$ aligns, which is to be expected, since the total angular momentum has to remain constant.

The end result of the Lense – Thirring precession is a BH which is aligned or anti-aligned with the surrounding accretion disc. The expression for the magnitude of $\boldsymbol{J}_{\rm tot}$ allows us to examine the final configuration of the system. Obviously, if $J_{\rm BH}^2 > J_{\rm tot}^2$ anti-alignment occurs, which requires

$$\cos\theta < -\frac{J_{\rm d}}{2J_{\rm BH}}. \tag{2.14}$$

Hence, a BH with $\theta > \pi/2$ *and* $2J_{\rm BH} > J_{\rm d}$, eventually anti-aligns with the accretion disc. This means that if $J_{\rm d} > 2J_{\rm BH}$ then alignment always happens as the disc angular momentum completely overwhelms that of the BH.

Further investigation of the warped discs requires knowledge of the accretion flow properties. We use the thin disc solution of Shakura & Sunyaev (1973) for our analysis. In the standard Shakura-Sunyaev disc model, the analytic expression for the warp radius depends on the values of $J_{\rm BH}$, $M_{\rm BH}$, and the accretion rate $\dot{M}$ of the BH. In terms of the Schwarzschild radius, $R_{\rm warp}$ is written as (Volonteri et al. 2007)

$$\frac{R_{\rm warp}}{R_{\rm Schw}} = 3.6\times10^3 a^{5/8}\left(\frac{M_{\rm BH}}{10^8\ {\rm M}_\odot}\right)^{1/8}\lambda^{-1/4}\left(\frac{\nu_2}{\nu_1}\right)^{-5/8}\alpha^{-1/2}. \tag{2.15}$$

Here α is the Shakura-Sunyaev viscosity parameter and $\lambda = L/L_{\rm Edd}$ is the Eddington ratio. The accretion luminosity, L, is defined as

$$L = \epsilon\dot{M}c^2, \tag{2.16}$$

with ϵ denoting the accretion efficiency, $\dot{M}$ the physical accretion rate and c the speed of light.

Given that the accretion is characterised by a timescale t_{ν_1}, the mass of the disc inside the radius $R_{\rm warp}$ is

$$M_{\rm d}(R_{\rm warp}) = \dot{M}t_{\nu_1}(R_{\rm warp}), \tag{2.17}$$

where the accretion timescale is given by

$$t_{\nu_1} = \frac{R_{\rm warp}^2}{\nu_1} = 3 \times 10^6 \, a^{7/8} \left(\frac{M_{\rm BH}}{10^8 \ {\rm M}_\odot} \right)^{11/8} \lambda^{-3/4} \left(\frac{\nu_2}{\nu_1} \right)^{-7/8} \alpha^{-3/2} \ {\rm yr}. \tag{2.18}$$

We can write the total angular momentum, $J_{\rm d}$, passing through $R_{\rm warp}$ as,

$$J_{\rm d}(R_{\rm warp}) \lesssim M_d(R_{\rm warp})(GM_{\rm BH}R_{\rm warp})^{1/2}. \tag{2.19}$$

In terms of the anti-alignment criterion this gives,

$$\frac{J_{\rm d}}{2J_{\rm BH}} = \frac{M_{\rm d}}{aM_{\rm BH}} \left(\frac{R_{\rm warp}}{R_{\rm Schw}} \right)^{1/2} = 10^{-9} \lambda \left(\frac{t_{\nu_1}}{1 \ {\rm yr}} \right) \left(\frac{R_{\rm warp}}{R_{\rm Schw}} \right)^{1/2} a^{-1}. \tag{2.20}$$

Evaluation of this quantity determines whether or not the anti-alignment condition in a misaligned disc is satisfied.

2.3.3 The case of self-gravity limited discs

The BH growth process in AGN environments involves vast amounts of accreted gas, often comparable to the initial mass of the accreting hole. This amount of mass settles onto the accretion disc around the hole, which often extends to several thousands of gravitational radii. It is usually assumed that the available mass fuel, $M_{\rm acc}$, is consumed in a single accretion episode, thus providing a supply of constant angular momentum (Volonteri et al. 2007). In this case, the amount of mass consumed is enough to spin up the hole up to $a = 0.998$, even if the BH initially was maximally spinning in a counter-rotating direction. Inevitably, repeated accretion episodes during major galaxy mergers act to spin up the BH to maximum rotation.

Recently, however, King et al. (2008) argued that the end result of the accretion growth channel might be completely different if we take into account the fact that an accretion disc becomes self-gravitating at some radius, $R_{\rm sg}$, where its mass exceeds $M_{\rm sg} \sim (H/R)M_{\rm BH}$. As a result, the mass of the disc is limited by its self-gravity to $\Delta M_{\rm episode} \ll M_{\rm acc}$, which gives rise to a series of $N \simeq M_{\rm acc}/\Delta M_{\rm episode}$ well separated accretion episodes. King et al. suggest that these accretion episodes are randomly oriented around the BH, an assumption supported by observations indicating that there is no apparent relation between the accretion disc (or radio jet) orientation and the host galaxy disc (Nagar &

Wilson 1999; Kinney et al. 2000). They further argue that this could be the result of intense star formation outside $R_{\rm sg}$ randomising the input gas direction, which could provide a qualitative explanation for the ring of stars seen in the near vicinity of the central BH in the Milky Way (Genzel et al. 2003).

The much smaller angular momentum associated with each accretion episode means that, in general, $J_{\rm d} < 2J_{\rm BH}$, so in the chaotic accretion model counteralignment occurs in a fraction (King et al. 2005)

$$f = \frac{1}{2}\left(1 - \frac{J_{\rm d}}{2J_{\rm BH}}\right) \simeq 1/2 \tag{2.21}$$

of the accretion episodes. Therefore, counter- and co-alignment are equally likely outcomes of the Lense – Thirring effect. However, accretion of gas in a counter-rotating disc is more efficient in spinning up the BH since the gas is being dumped onto the BH from a larger distance and, thus, carries more angular momentum into the BH. Hence, a succession of counter-aligned and co-aligned accretion episodes with equal frequency should systematically spin down the BH, resulting in a global spin distribution oscillating around zero.

The physics of self-gravitating accretion discs is described by Pringle (1981). Briefly, the criterion that the self-gravity of a disc be negligible is the requirement that the gravitational force along the $\hat{z}$ direction be dominated by the central BH. This can be expressed as the surface density of the disc, Σ, being negligible compared to the quantity $M_{\rm BH}H/R^3$, or in terms of the disc mass,

$$M_{\rm d}(< R) \ll \frac{H}{R} M_{\rm BH}. \tag{2.22}$$

The self-gravity becomes marginally important when $M_{\rm d} \simeq (H/R)M_{\rm BH}$, which defines the self-gravity radius, $R_{\rm sg}$, given by

$$\frac{R_{\rm sg}}{R_{\rm Schw}} = 1.5 \times 10^3 \, \epsilon^{8/27} \left(\frac{M_{\rm BH}}{10^8 \ {\rm M}_\odot}\right)^{-26/27} \lambda^{-8/27} \alpha^{14/27}. \tag{2.23}$$

The semi-thickness of the disc in the Shakura-Sunyaev model is given by,

$$\frac{H}{R} = 1.36 \times 10^{-3} \epsilon^{-1/5} \left(\frac{M_{\rm BH}}{10^8 \ {\rm M}_\odot}\right)^{-1/10} \lambda^{1/5} \left(\frac{R}{R_{\rm Schw}}\right)^{1/20} \alpha^{-1/10}. \tag{2.24}$$

Hence, by replacing R with $R_{\rm sg}$ in expression (2.24), we obtain an analytic expression for the disc mass within $R_{\rm sg}$,

$$M_{\rm sg} = \frac{H}{R} M_{\rm BH}\Big|_{R=R_{\rm sg}} = 2.13 \times 10^5 \ \epsilon^{-5/27} \left(\frac{M_{\rm BH}}{10^8 \ {\rm M}_\odot}\right)^{23/27} \lambda^{5/27} \ \alpha^{-2/17} \ {\rm M}_\odot. \qquad (2.25)$$

As we described in Section 2.3.2, once the disc forms with a non-zero misalignment angle about the spin axis of the hole, it will be subject to the Lense – Thirring precession. If the radius, $R_{\rm sg}$, is greater than $R_{\rm warp}$, then

$$J_{\rm d} = J_{\rm d}(< R_{\rm warp}). \qquad (2.26)$$

If, however, $R_{\rm sg} < R_{\rm warp}$, then the entire disc will be subject to Lense – Thirring precession, thus aligning itself in the equatorial plane of the BH.

2.3.4 BH-BH binary coalescence

We now examine the evolution of spin during BH binary coalescence. During the merger of the two binary members, the smaller BH adds its spin and orbital angular momentum at the LSO to the spin of the larger one. Even if the progenitor holes do not possess any orbital angular momentum, the final remnant will preserve the residual orbital momentum of the binary (i.e. the angular momentum that has not been radiated away). Thus, the remnant will always be a Kerr BH.

Recent breakthroughs in numerical relativity have provided robust simulations of BH mergers by solving directly the Einstein equations in a fully relativistic frame (Campanelli et al. 2007; Herrmann et al. 2007; Marronetti et al. 2007). These simulations have explored the parameter space for different configurations of initial masses and spins, allowing accurate measurements of the final spin. For example, a merger of two equal mass BHs both with $a = 0$ in a circular orbit results in a Kerr BH with $a^f \simeq 0.69$ (Baker et al. 2006b). This a robust prediction and is also valid for eccentric orbits with eccentricities smaller than 0.4 (Hinder et al. 2008).

Analytic fits extend the predictions for a^f to the entire space of parameters and reproduce closely all the available numerical data. In the case where the masses are unequal

but the spins are zero, the final spin can be estimated by the analytic expression

$$a^f \simeq 2\sqrt{3}\frac{q}{(1+q)^2} - 2.029\frac{q^2}{(1+q)^4}, \tag{2.27}$$

where $q = M_2/M_1 \leqslant 1$ is the mass ratio of the progenitor BHs (Berti et al. 2007).

A more general analytic fitting formula for predicting the final spin of any given binary configuration has been provided by Rezzolla et al. (2008a,b). In their analysis, they assume that the final spin parameter vector can be expressed as

$$\boldsymbol{a}^f = \frac{1}{(1+q)^2}(\boldsymbol{a_1} + \boldsymbol{a_2}q^2 + \boldsymbol{\ell}q), \tag{2.28}$$

where $\boldsymbol{a_{1,2}} = c\mathbf{J}^{1,2}_{\rm bh}/(GM^2_{1,2})$ and $\boldsymbol{\ell} = \boldsymbol{\ell'}/(M_1M_2)$, with $\boldsymbol{\ell'}$ defining the difference between the orbital angular momentum, $\boldsymbol{l}$, when the binary is widely separated, and the angular momentum radiated away in gravitational waves before the merger, $\boldsymbol{j}_{\rm rad}$, namely,

$$\boldsymbol{\ell'} = \boldsymbol{l} - \boldsymbol{j}_{\rm rad}. \tag{2.29}$$

The vector $\boldsymbol{\ell'}$ is taken to be parallel to the orbital momentum vector throughout the evolution of the binary, an assumption which is not strictly valid since the system could radiate away angular momentum in a non-symmetric way. However, the error introduced by this assumption is relatively small for the binary configurations studied in the simulations of Rezzolla et al. A further assumption is that the mass radiated away in gravitational waves is negligible, as it accounts for only a small fraction $(5-7\%)$ of the total mass-energy of the binary configurations analysed. Under these assumptions, Rezzolla et al. (2008a,b) proposed an analytic expression for the magnitude of the final spin, given by

$$\begin{aligned}|\boldsymbol{a}^f| = \frac{1}{(1+q)^2}\Big[&|\boldsymbol{a}_1|^2 + |\boldsymbol{a}_2|^2q^4 + 2|\boldsymbol{a}_2||\boldsymbol{a}_1|q^2\cos\varphi \\ &+2\left(|\boldsymbol{a}_1|\cos\vartheta + |\boldsymbol{a}_2|q^2\cos\xi\right)\boldsymbol{\ell}q + \boldsymbol{\ell}^2q^2\Big]^{1/2},\end{aligned} \tag{2.30}$$

with the cosine angles φ, ϑ and ξ defined as

$$\cos\varphi \equiv \hat{\boldsymbol{a}}_1\cdot\hat{\boldsymbol{a}}_2, \quad \cos\vartheta \equiv \hat{\boldsymbol{a}}_1\cdot\hat{\boldsymbol{\ell}}, \quad \cos\xi \equiv \hat{\boldsymbol{a}}_2\cdot\hat{\boldsymbol{\ell}}. \tag{2.31}$$

The norm of $\boldsymbol{\ell}$ is given by,

$$
\begin{aligned}
|\boldsymbol{\ell}| = & \frac{s_4}{(1+q^2)^2}\left(|\boldsymbol{a}_1|^2 + |\boldsymbol{a}_2|^2 q^4 + 2|\boldsymbol{a}_1||\boldsymbol{a}_2| q^2 \cos\varphi\right) \\
& + \left(\frac{s_5\mu + t_0 + 2}{1+q^2}\right)\left(|\boldsymbol{a}_1|\cos\vartheta + |\boldsymbol{a}_2| q^2 \cos\xi\right) \\
& + 2\sqrt{3} + t_2\mu + t_3\mu^2 .
\end{aligned} \tag{2.32}
$$

Here μ expresses the symmetric mass ratio, $\mu = q/(1+q)^2 = M_1 M_2/(M_1+M_2)^2$, and the coefficients take the values $s_4 = -0.129$, $s_5 = -0.384$, $t_0 = -2.686$, $t_2 = -3.454$, $t_3 = 2.353$. The final spin as given by Eq. (2.30) is in good agreement with numerical data, with residuals of less than 3%.

2.4 Modelling the spin evolution GALFORM

In this section we describe our method for calculating the evolution of BH spin in GALFORM. During the formation history of the BHs we take into account spin changes due to the accretion of gas and mergers, as described in Section 2.3. The initial population of seeds is assumed to be non-rotating. These seeds grow through accretion of gas during disc instabilities, galaxy mergers, and hot-halo mode accretion and through BH-BH mergers.

2.4.1 Thin discs

To model the physics of the accreted gas, we assume that when $\dot{m} \geqslant 0.01$ the gas forms an accretion disc around the BH whose physics is described by the standard Shakura-Sunyaev disc model. We assume that the gas available to be fed into the BH after a galaxy merger or the collapse of a dynamically unstable disc is accreted over a timescale $t_{\rm acc}$, proportional to the dynamical timescale of the galactic bulge that hosts the BH, $t_{\rm acc} = f_{\rm q}\, t_{\rm Bulge}$. A fixed proportionality factor, $f_{\rm q} = 4$, is used in this analysis resulting in typical accretion timescales of the order of $10^7 - 10^8$ yr. Note that, this factor is ~ 10 longer than the one chosen by Malbon et al. (2007). The new value is introduced in order to match the local quasar luminosity function and does not affect the galaxy-formation model. The timescale for accretion during the hot-halo mode is computed directly by the galaxy formation model and depends on the cooling timescale of the gas in the hot halo.

The accretion disc is assumed to be randomly oriented relative to the spin axis of the hole. If $\theta \neq 0^\circ, 180^\circ$, we assume that the disc precesses around the BH as described in Section 2.3.2. In brief, for a given BH mass, $M_{\rm BH}$, we determine the numerical values of the warp parameters, $R_{\rm warp}$, $M_{\rm d}(R_{\rm warp})$, and the angular momenta $J_{\rm d}(R_{\rm warp})$ and $J_{\rm BH}$. The ratio $J_{\rm d}/2J_{\rm BH}$ allows us, through the criterion in Eq. (2.14), to check if anti-alignment or alignment occurs. We then allow the BH to accrete an amount of gas equal to $M_{\rm d}(R_{\rm warp})$ and evolve the spin using Eq. (3.6). Finally, we update the mass of the BH and estimate the hole's new spin and the disc precession by calculating the new angles θ and θ_t. This process is repeated until: (a) the disc aligns or counteraligns ($\theta = 0^\circ$ or 180°) with the hole's spin, in which case we just consume the rest of the available gas and evolve the spin according to Eq. (3.6), or (b) the accretion disc is entirely consumed, without being able to align or counteralign itself with the spin. In almost all cases we find that the accretion disc ultimately aligns (or anti-aligns) itself on the equatorial plane of the BH.

In addition to the case where the entire gas reservoir is consumed within one accretion episode with constant angular momentum orientation (prolonged accretion), we test the model proposed by King et al. (2008) in which the mass of the accretion disc is limited by its self-gravity (chaotic accretion). We repeat the same steps as before. However, in this case $M_{\rm d} = M_{\rm sg}$. Once $M_{\rm sg}$ is consumed, we update the mass of the hole and determine the mass of the new disc, $M'_{\rm sg}$, computed from the updated BH mass. At this point we make the assumption that the disc retains no memory of the angular momentum of the initial flow and that it settles into a random orientation around the BH with $M_{\rm d} = M'_{\rm sg}$. We then add the next $M_{\rm sg}$ until the disc is consumed.

It is important to clarify at this point that the two accretion models considered here serve as a means for studying the effect of accretion on BH spin. The forthcoming analysis that follows and results do not rely on any specific model for the physical processes that drive the gas flows towards the vicinity of the BH. Several mechanisms for feeding the SMBH with gas could result to similar spin distributions to the chaotic accretion case considered here (see for example, Heller et al. 2001 for the properties of non self-gravitating gaseous bars in barred disc galaxies and Hobbs et al. 2010 for an investiga-

tion of the effect of supernova-driven turbulence on the fuelling of SMBHs in galactic bulges). Here, our main goal is to explore the effect of different SMBH spin distributions on properties of the host galaxy.

2.4.2 ADAFs

Many of the accretion events in our simulations are characterised by low, sub-Eddington, accretion rates, with $\dot{m} \leqslant 0.01$. For such low accretion rates, the gas flow has low density and is unable to cool efficiently since radiative cooling does not balance the energy generated by viscosity. Thus, the viscous energy is trapped in the gas as entropy and ultimately advected into the hole. This type of accretion is known as an advection dominated accretion flow (ADAF: Rees 1982; Narayan and Yi 1994; Abramowicz et al. 1995).

ADAFs have a number of distinct properties that some of them will be essential for the analysis in later sections. For example, for an ADAF around a BH, only a fraction of the standard accretion luminosity, $L = \epsilon \dot{M} c^2$, is emitted as radiation. The remainder of the viscously dissipated energy is stored in the gas as entropy, resulting in hot flows with almost virial temperatures. We note that, as shown by Ichimaru (1977), the ions and the electrons in an ADAF are not thermally coupled and, thus, reach different temperatures. This two-temperature virialised plasma flow is optically thin and, for high viscosity parameters ($\alpha \sim 0.2 - 0.3$), it acquires a quasi-spherical geometry around the BH ($H \sim R$), which resembles spherical Bondi accretion. However, despite the geometrical similarity, the dynamics of the ADAF are fundamentally different, since the accretion is entirely due to dissipation via viscous forces rather than gravity.

In general, the accretion flow can have a rather complicated structure. For example, it is possible that a thin disc dominates the geometry of the outer parts, then switches to an ADAF as the flow approaches the BH (Esin et al. 1997). The transition to the thick flow depends on the accretion rate and usually occurs closer to the BH for higher accretion rates. Such a complex disc model for describing the accretion flows during the hot-halo mode is, however, beyond the scope of this work. Here, we assume a simple configuration of a quasi-spherical corona around the hole with any transition to a thin disc occurring far from the BH. Precession effects due to misalignment between the disc

and the BH are modelled as in the thin disc case.

2.4.3 Binary mergers

Finally, we consider the spin changes due to binary coalescence. Following the merger of two galaxies in GALFORM, each harbouring a SMBH, the one hosted by the satellite sinks towards the SMBH of the central galaxy and eventually form a binary. In our model, BH mergers tend to occur in gas-poor environments, and thus, we assume that torques from accreting flows that might be present during the formation of the binary do not influence the orientation of the BH spins prior the merger. We therefore take the BH spin vectors in Eq. (2.30) to be randomly oriented relative to each other and the orbital angular momentum. In addition, we assume that all binaries will ultimately merge on a very short timescale, effectively right after the host galaxies merger and induced accretion have been completed.

During the merger, the smaller BH plunges into the larger one carrying along its angular momentum at the LSO. At this point we neglect any mass loss due to gravitational wave emission, as it corresponds to a small fraction of the total mass-energy of the system. In addition, we do not take into account the effects of gravitational recoil due to asymmetric emission of gravitational waves in binary mergers. In our model, mergers with recoil velocities as high as $v_{\rm recoil} \sim 500$ km s^{-1} (Libeskind et al. 2006) could displace BH remnants. However, we assume that dynamical friction relocates them in the galactic centre. Therefore, we do not expect gravitational recoil to have a significant impact on the spin distribution of the remnant BHs. The spin of the final remnant is finally estimated using the fitting formulae in Eqns. (2.30) & (A.13), as described in Section 2.3.4.

2.5 The cosmological evolution of BH mass and spin

2.5.1 Evolution of BH mass

We now briefly present our main predictions for BH growth, using our updates (see Section 2.1) to the model developed by Bower et al. (2006) and Malbon et al. (2007). In

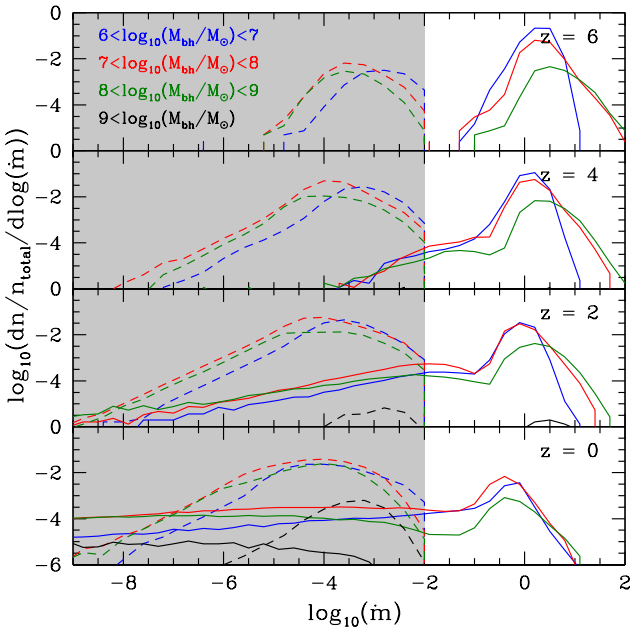

Figure 2.3: The distribution of accretion rates for selected BH mass ranges at various redshifts. Line styles represent two different accretion modes: solid lines for the starburst mode and dashed lines for the hot-halo mode. The shaded area represents the regime where the accretion flow is described by an ADAF. The accretion rates in the hot-halo mode are truncated at $\dot{m} = 0.01$, in accordance with our model of AGN feedback. In the present Universe, the starburst mode accretion peaks at $\dot{m} \simeq 0.5$. However, the peak shifts to higher values at higher redshifts, indicating that accretion was more efficient in the past.

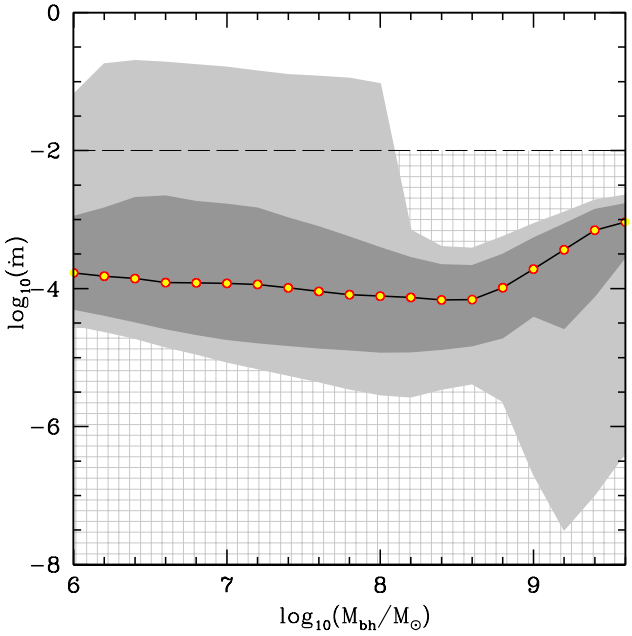

Figure 2.4: The correlation of accretion rate with BH mass at redshift zero. The median (red-yellow points), $20-80$ percentiles (dark grey) and $5-95$ percentiles (light grey) are shown. The shaded background indicates the region were the accretion disc is modelled as an ADAF. Only lower mass BHs ($< 10^8$ $\mathrm{M}_\odot$) i.e. those hosted by lower mass galaxies (typically spirals) have enough gas left to trigger accretion via a thin disc ($\dot{m} > 0.01$). More massive BHs have little cold gas and undergo hot-halo mode accretion which (by construction) has $\dot{m} < 0.01$.

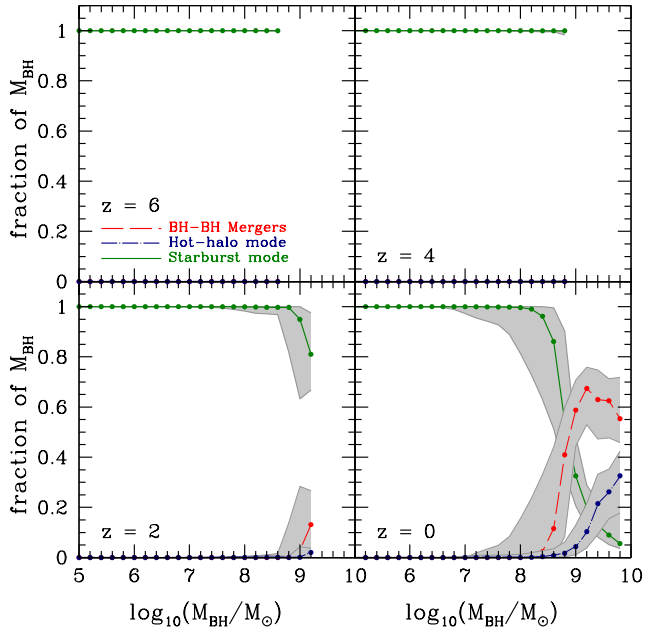

Figure 2.5: Contribution to the final BH mass at different redshifts from gas accretion in starburst mode (solid green line), hot-halo mode (dashed blue line) and BH-BH mergers (dashed-dotted red line) in the updated Bower et al. (2006) model. The lines represent the medians and the shaded region the 20-80 percentiles of the distributions. The dominant channel of BH growth for BHs with $M_{\rm BH} \lesssim 10^8$ $\rm M_\odot$ is the starburst mode. Above that mass, mergers and hot-halo mode become the dominant growth channels.

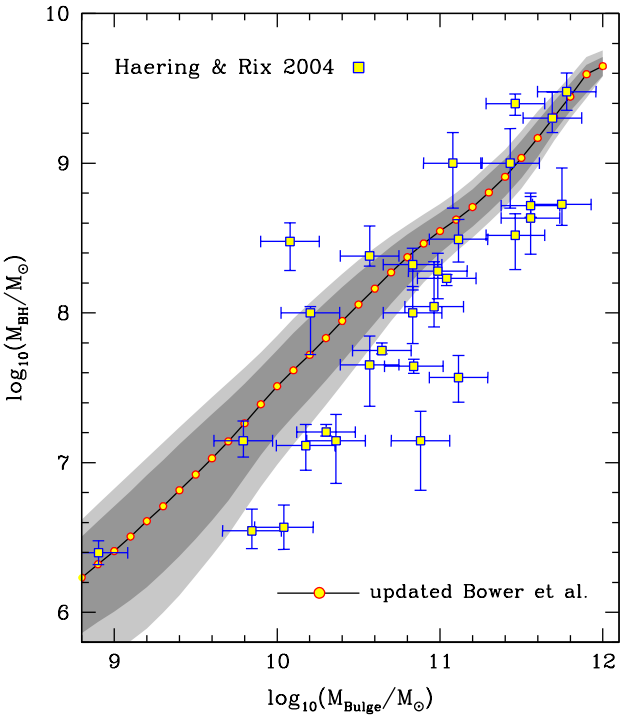

Figure 2.6: The $M_{\rm BH} - M_{\rm bulge}$ relation predicted by the updated Bower et al. (2006) model (solid line). The shaded areas indicate the $10-90$ (light) and $20-80$ (dark) percentile spread of the theoretical predictions. The observational data is taken from Haering & Rix (2004).

Fig. 2.3 we show the fraction of all BHs that accrete at a given rate in the starburst and hot-halo modes, at different redshifts. All BHs that accrete in the hot-halo mode during the redshift bin are included, but the starburst mode is episodic so we only include objects which experience a starburst within a given redshift bin. Our updated parameters give a longer duration for the accretion episode in the starburst mode (4 times rather than 0.5 times the dynamical timescale of the bulge) than assumed in Malbon et al. 2007. This results in the majority of BHs with mass $10^6 - 10^8$ $\rm M_\odot$ which accrete in the starburst mode at $z = 0$ having $\dot{m} \simeq 0.5$, as observed (Heckman et al. 2004). At higher redshift the distributions shift to higher mass accretion rates, with a mean $\dot{m} \simeq 3$ at $z = 6$. This implies that in a hierarchical universe, accretion of gas was more efficient at early epochs, so the rate of growth of BHs is faster in the past. By contrast, accretion activity during

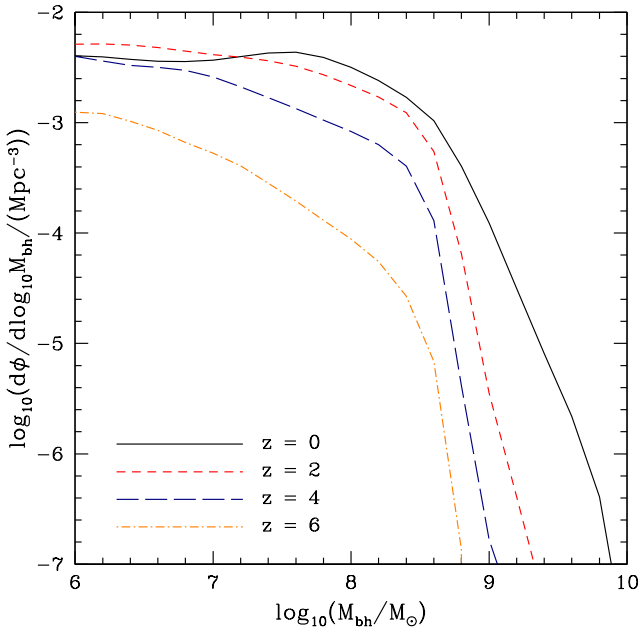

Figure 2.7: The predicted mass functions at $z = 0, 2, 4$ and 6 for the BH population in our simulation.

the hot-halo mode peaks at very low accretion rates ($\dot{m} \approx 10^{-4}$) at $z = 0$, with a long tail to lower values together with some spread to the maximum allowed value of 0.01 (imposed by the AGN feedback model). This upper limit to the mass accretion rate limits the shift to higher $\dot{m}$ at higher z, so the main evolutionary trend is that there are fewer very low $\dot{m}$ radio mode objects at high z.

This model results in a *bimodal* mass accretion rate distribution for all BH masses and redshifts. Activity triggered by accretion of cold gas from the galaxy disc, replenished by galaxy mergers, has a mean mass accretion rate which is ~ 1000 times higher than that of activity fed by hot-halo mode accretion. However, the relative importance of these two modes varies with BH mass. This is shown in more detail in Fig. 2.4 which shows the $20 - 80$ and $5 - 95$ percentile mass accretion rates as a function of BH mass at $z = 0$. More than 5 per cent of the lower mass AGN have accretion via a thin disc ($\dot{m} > 0.01$). However, this fraction drops with mass at BH masses of $\sim 10^8$ $\mathrm{M}_\odot$. More massive galaxies are hosted by large ellipticals which are gas poor and are dominated by hot-halo mode accretion.

Fig. 2.5 shows the contribution from the different growth channels to the final BH mass at different redshifts. At high redshifts, SMBHs with masses up to $\sim 10^8$ $\mathrm{M}_\odot$ build their mass almost exclusively through the accretion of cold gas (starburst mode). This forms either a thin disc or an ADAF depending on $\dot{m}$ (see also Fig. 2.3). Accretion of gas from the hot halo of massive galaxies during the hot-halo mode always occurs with $\dot{m} \leq 0.01$ by construction, thus giving rise to an ADAF. This low upper limit to the mass accretion rate in this mode means that it makes comparatively little impact on BH growth, except for masses greater than 10^8 $\mathrm{M}_\odot$. Note that in the original Bower et al. (2006) model, the hot-halo mode is responsible for building most of the BH mass above 10^8 $\mathrm{M}_\odot$, while in the updated version presented here, both BH mergers and hot-halo mode contribute significantly for high mass BHs.

In Fig. 2.6 we compare the relationship between the BH mass and host bulge mass predicted by our model to the observational data. The model predicts an almost linear relation and reproduces the observations reasonably well. The scatter in BH mass is ~ 1 dex for bulge masses below 10^{11} $\mathrm{M}_\odot$ and becomes gradually smaller for higher bulge masses. The resulting BH mass functions are shown in Fig. 2.7. These show that the present day Universe is dominated by BHs with masses of $\sim 10^7 - 10^8$ $\mathrm{M}_\odot$ which is in good agreement with the recent results from the Sloan Digital Sky Survey (SDSS) of Heckman et al. (2004). The shape of the mass functions are fairly similar at all redshifts. The main difference occurs at the high-mass end where the BH mass function extends to higher masses at low redshifts. For $M_{\mathrm{BH}} \lesssim 10^8$ $\mathrm{M}_\odot$ the mass function is almost constant and flat up to $z = 2$. This indicates that these BH are already in place at $z = 2$. Above that mass, there is a sharp decrease in the space density of BH at $z = 2$ and $z = 4$. At $z = 0$, the mass function has a shallower slope.

2.5.2 Evolution of BH spin

The histograms in Fig. 2.8 show the distributions of BH spins at different redshifts (left panel) and for different mass ranges (right panel) for all galaxies that host BHs with $M_{\mathrm{BH}} \geqslant 10^6$ $\mathrm{M}_\odot$. The top and bottom panels correspond to the chaotic and prolonged accretion models respectively. The BH spin distributions predicted by the two accretion

models are already established at $z = 6$ and do not change appreciably with time. The major channel for BH growth at $z = 6$ is the starburst mode and this generally takes place via a thin disc. The accreted mass in each episode is generally larger than the mass of the BH, so this spins it up to maximal in the prolonged accretion model. The break up of the accretion into much smaller individual events in the chaotic model leads to a random walk spin distribution around a low spin value. Nonetheless, the plots in Fig. 2.5 show that BH-BH mergers contribute to the most massive BHs at late redshifts, as does accretion with $\dot{m} < 0.01$ in both the radio and starburst mode. In order to gain further insight into the effect of these growth channels we show the different spin distributions as a function of BH mass at $z = 0$ in the right hand panels.

As already mentioned, low mass BHs are built via thin-disc accretion in the starburst mode (Fig. 2.5) with mean $\dot{m} \sim 0.5$. For a BH of mass 10^6 $\mathrm{M}_\odot$ a typical accretion event in the starburst mode contains 10^6 $\mathrm{M}_\odot$ of gas, so in the prolonged accretion model this will spin the BH up to maximal. However, in the chaotic accretion model in which the size of the disc is limited by its self-gravity, the mass of the gas that settles on the disc cannot be more than $\sim (H/R) \times 10^6$ $\mathrm{M}_\odot$ $\sim 10^4$ $\mathrm{M}_\odot$. Thus, a 10^6 $\mathrm{M}_\odot$ accretion event consist of ~ 100 accretion episodes with $\Delta M_{\rm episode} \ll M_{\rm BH}$, all randomly oriented around the BH. As a consequence, $10^6 - 10^8$ $\mathrm{M}_\odot$ BHs experience a net spin-down to modest values centred around $a^f \sim 0.15$.

The growth channel for more massive BHs ($M_{\rm BH} > 10^8$ $\mathrm{M}_\odot$) includes a large fraction of objects which accrete in the hot-halo mode or starburst mode with $\dot{m} < 0.01$ i.e. via a geometrically thick ADAF. However, we do not include full modelling of this process as our spin evolution calculations always assume a Shakura-Sunyaev thin disc rather than the appropriate ADAF equations. We do not expect this to have a large effect on the spin distributions as most of the BH mass and spin are built up from high mass accretion rates.

The mergers between massive BHs have a significant impact on the final spin distributions. According to the analytic fitting formula, Eqn. (2.30) from Rezzolla (2008, 2009), the post-merger spin of the final remnant depends strongly on the masses of the progenitors. For example, BHs acquiring a final spin greater than 0.69 after a merger are

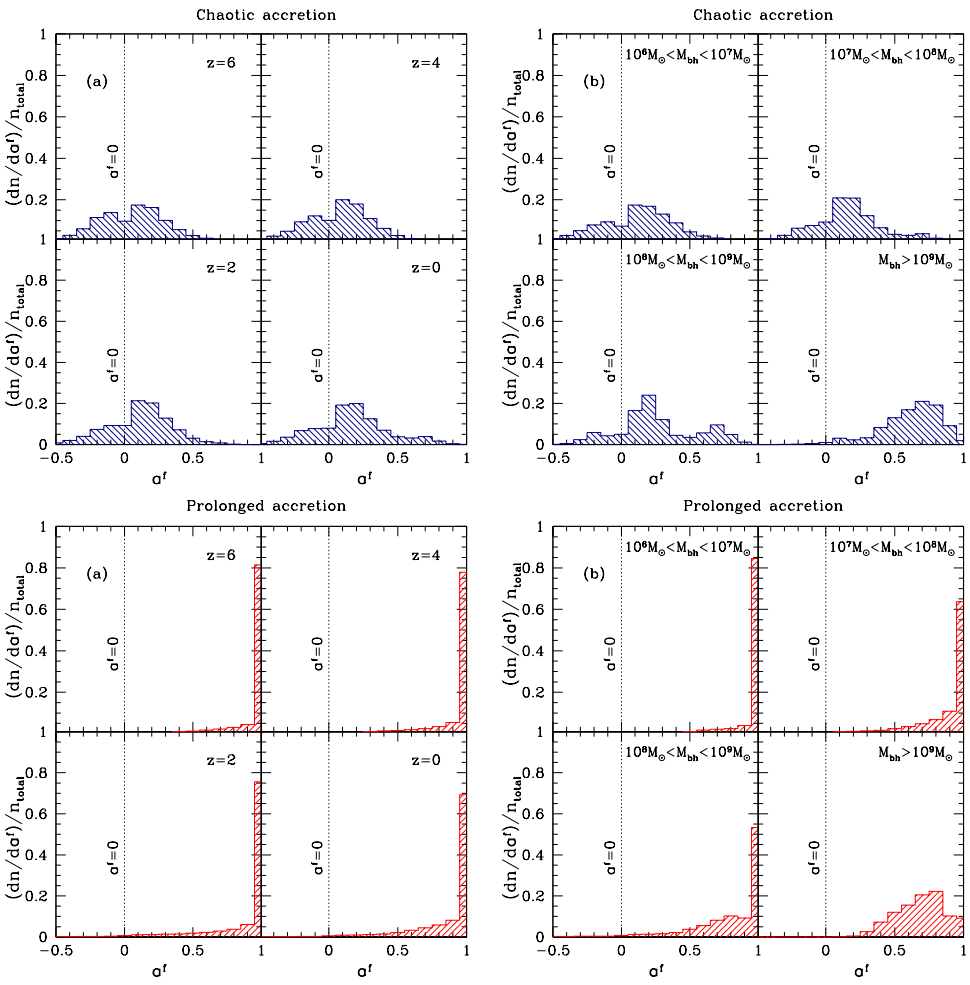

Figure 2.8: Model predictions for the final BH spin distributions. (a) The spin evolution due to BH mergers and accretion and (b) the distribution of BH spins at $z = 0$ in different mass bins in the chaotic (upper panels) and prolonged (lower panels) accretion models. The main difference between the two accretion modes is that the chaotic case results in low mass BHs having spins distributed around zero, whereas the prolonged case results in a distribution peaked at around $a^{\rm f} = 0.998$.

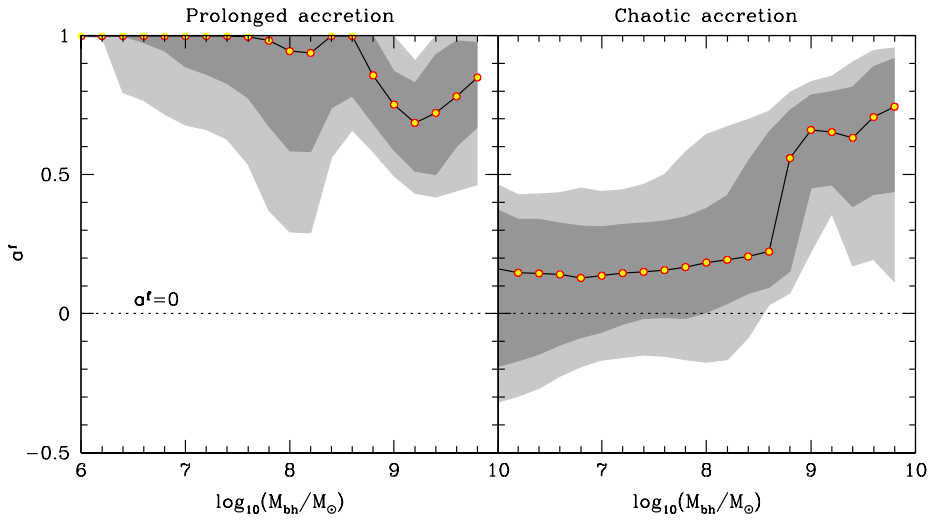

Figure 2.9: The correlation of spin with BH mass (a) for the prolonged and (b) the chaotic accretion models. The solid lines show the medians and the shaded areas the $10-90$ (light) and $20-80$ (dark) percentile spreads of the distributions.

the end product of binaries of comparable mass ($q \simeq 1$) in which the members already had significant spins (recall that $a^{\rm f} = 0.69$ is the final spin of a binary of equal-mass non-spinning BHs). Mergers between BHs of comparable mass are common only for the most massive BHs ($M_{\rm BH} \gtrsim 10^8$ M$_\odot$) in our simulation[3]. This is because these BHs are hosted by massive elliptical galaxies that have experienced at least one major merger (merger between galaxies of equal mass) in their past history (Parry et al. 2009). Hence, their BHs, which are of similar mass, will acquire a final spin close 0.69 or higher (depending on the value of the initial spins) after they coalesce. In contrast to the most massive BHs, lower mass BHs ($M_{\rm BH} \lesssim 10^8$ M$_\odot$) which experience a merger, are involved mostly in minor mergers ($q \ll 1$). These do not have a significant impact on the final spin of the

[3]At redshift zero nearly 19% of the BHs with $M_{\rm BH} \geqslant 10^6$ M$_\odot$ have experienced at least one merger. The low merger rate of BHs merely reflects the relative minor effect that mergers have in the formation of galactic spheroids (except in very massive ellipticals) in the Bower et al. (2006) model, as found by Parry et al. (2009). For example, at redshift zero about 6% of the BHs with $M_{\rm BH} \geqslant 10^6$ M$_\odot$ have experienced more than one merger and only $\sim 8\%$ have had a recent major merger

remnant which is dominated by the more massive member of the binary.

When the effects on BH spin of mergers and accretion are combined, we find the following result. BHs of mass $\gtrsim 5 \times 10^8$ $\mathrm{M}_\odot$ that have experienced a major merger will acquire spins greater than ~ 0.69; since these mergers often occur in gas poor environments, the spin distribution for these masses is not significantly altered by the accretion. For lower mass BHs, accretion *quickly* erases the characteristic post-merger spins, because the growth is dominated by intense accretion during the starburst mode. For chaotic accretion, this results in a bimodal distribution of spins for BHs with mass $10^8 - 10^{10}$ $\mathrm{M}_\odot$. The first peak is located at $a^{\mathrm{f}} \sim 0.15$ and corresponds to BHs that have had a major merger accompanied by an accretion episode in which the post merger spin is quickly erased and kept low. The second peak is located at $a^{\mathrm{f}} \sim 0.7 - 0.8$ and corresponds to BHs that experienced a merger in the absence of accreting flows and acquired a final spin characteristic of post-merger BH remnants.

We note that BHs in our cosmological model have low merger rates at high redshift ($z \sim 6$). As redshift decreases, the merger rate increases and reaches a maximum at $z \sim 1.5$. Eventually, at $z = 0$ nearly 19% of the BHs with $M_{\mathrm{BH}} \geqslant 10^6$ $\mathrm{M}_\odot$ have experienced at least one merger. Therefore, the significance of mergers increases with decreasing redshift. This accounts for the decrease with redshift of the rapidly rotating BHs in the prolonged model.

We finally show in Fig. 2.9 the correlation between the BH mass and spin. This figure confirms the conclusion of Fig. 2.8: BHs that grow their mass through chaotic accretion display a strong correlation between their mass and spin. In this case we find that the BH mass correlates with the host-galaxy morphology such that small BHs are usually found in spiral galaxies, whereas massive BHs are found in massive ellipticals. Thus, the apparent correlation between BH mass and spin indicates a strong correlation between BH spin and host-galaxy morphology. As a consequence, we expect to find rapidly rotating BHs in principle at the centres of very massive elliptical galaxies. However, these are also the objects which have low mass accretion rates (see Fig. 2.4), and so predominantly accrete via an ADAF whereas some fraction of the lower mass, low spin BH can accrete via a thin disc. By contrast, in the case of prolonged accretion there is no ap-

parent correlation between the BH mass and spin since most of the BHs exhibit very high spin independently of mass. Thus, rapidly rotating BHs are found in most types of galaxy. The correlation of mass and mass accretion rate (Fig. 2.4) remains the same, so the most massive ellipticals harbour the most massive BHs and accrete via an ADAF while a small fraction of the lower mass BHs in spirals can accrete via a thin disc. Note that the correlation between $M_{\rm BH}$ and spin for BH masses greater than 10^9 $\rm M_{\odot}$ is similar to that predicted by the chaotic model since these BHs include more growth through BH merger activity, which is independent of the accretion model.

2.6 Optical luminosities of AGN and the quasar luminosity function

We now explore whether our models are capable of explaining the observed properties of AGN. In particular, we present our predictions for the quasar luminosity function assuming that quasar activity is driven by accretion onto a SMBH. In our model, SMBHs with $\dot{m} > 0.01$ are assumed to accrete through a thin disc, whereas, those with accretion rates below this are assumed to accrete through an ADAF. In the thin-disc regime the bolometric luminosity is given by the standard expression,

$$L = \epsilon \dot{M} c^2. \tag{2.33}$$

The accretion efficiency, ϵ, is taken to vary with the hole's spin according to Eq. (2.3). When the accretion rate becomes super-Eddington ($\dot{m} > 1$), the bolometric luminosity is limited to $(1 + \ln \dot{m}) L_{\rm Edd}$ (Shakura & Sunyaev 1973). However, we do not restrict the accretion rate if the flow becomes super-Eddington. For the ADAFs, we assume that the plasma acquires a two-temperature configuration. The bolometric luminosity of the disc in this case is given by Mahadevan (1997),

$$L_{\rm bol,ADAF} = 1.3 \times 10^{38} \left(\frac{M_{\rm BH}}{M_{\odot}}\right) \left(\frac{\dot{m}^2}{\alpha^2}\right) \left(\frac{\beta}{0.5}\right) \ {\rm erg\ s^{-1}}, \tag{2.34}$$

where, β is related to the Shakura-Sunyaev viscosity parameter α through the relation $\alpha \approx 0.55(1 - \beta)$ (Hawley et al. 1995). The value of α is taken to be to 0.1 for all objects in our samples.

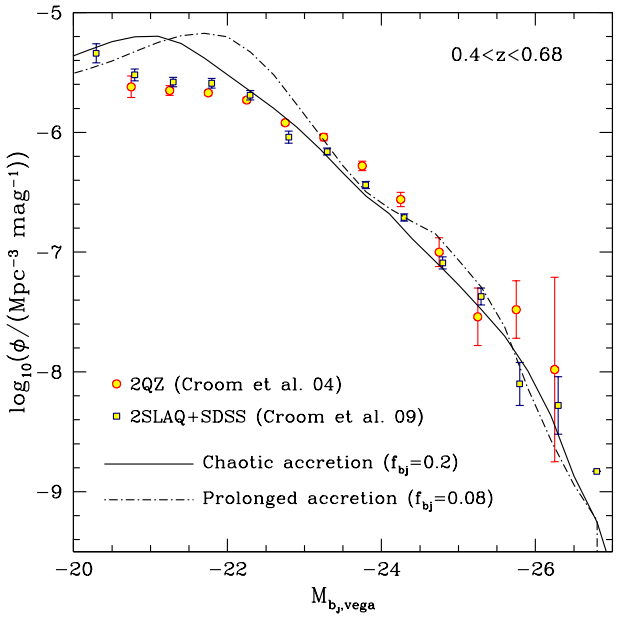

Figure 2.10: The model quasar luminosity function at $z = 0.5$ for the prolonged (dashed-dotted line) and chaotic (solid line) accretion models. The luminosity function includes only AGN assumed to be powered by a thin disc ($\dot{m} > 0.01$) that accrete in the quasar mode. The best fits to the observational data require that 8% (prolonged model) and 20% (chaotic model) of the bolometric luminosity be emitted in the $b_{\rm J}$-band. It further requires that 40% of the total number of AGN be obscured in both accretion models. The quasar luminosity functions from the 2dF (Croom et al. 2004) and 2dF-SDSS QSO survey (Croom et al. 2009) over the range $0.4 < z < 0.68$ are shown with circles and boxes respectively.

Observationally, the quasar bolometric luminosity function can be estimated by combining measurements in many different wavelengths (Hopkins et al. 2007; Shankar et al. 2009). We can compare the predictions of our model to the estimated bolometric luminosity function simply by counting the number of quasars radiating at a given luminosity bin. In this analysis, however, we will attempt to calculate the optical $b_{\rm J}$-band luminosity function since we are ultimately interested in comparing the strength of the radio jet emission of an AGN relative to its disk optical emission (see Section 2.7).

The conversion factor between bolometric accretion luminosity and $b_{\rm J}$-band luminosity, $f_{b_{\rm J}}$, is assumed to be constant and its value is adjusted to match the observed $b_{\rm J}$-band luminosity function. We take $f_{b_{\rm J}} = 0.08$ for the prolonged accretion and $f_{b_{\rm J}} = 0.2$ for the chaotic accretion model. The substantial difference between the conversion factors for the two accretion models reflects the strong dependence of the bolometric luminosity on the spin through the accretion efficiency. An increase in spin means that the disc can extend closer in towards the BH, so the same mass accretion rate produces more UV emission for the same $b_{\rm J}$-band luminosity. Hence the $b_{\rm J}$-band carries a smaller fraction of the bolometric luminosity. We check our conversion factors derived from fitting the quasar luminosity function to those derived from a Novikov-Thorne (fully relativistic) version of the Shakura-Sunyaev disc equations, assuming that the $b_{\rm J}$ band is centred at 4400 Å, with a FWHM of 980 Å. We find that our assumption is in good agreement with the theoretical calculations as long as we assume that the disc luminosity is Eddington limited and similarly they are in good agreement with the values of $0.07-0.15$ suggested by Elvis et al. (1994) from analysis of the SEDs of a large sample of quasars. Thus, we adopt these values for the rest of our calculations.

In deriving the luminosity function, we assume that only thin-disc accreting objects have the intense ionising flux which leads to their identification as quasars. We further assume that a fraction of 40% of the total number of quasars in obscured in the $b_{\rm J}$-band by the torus (Polletta et al. 2008). Finally, absolute $b_{\rm J}$-magnitudes in the Vega system are obtained using the relation,

$$M_{b_{\rm J}} = -10.44 - 2.5\log(L_{b_{\rm J}}/10^{40}\mathrm{erg\ s^{-1}}). \tag{2.35}$$

Fig. 2.10 shows the resulting quasar luminosity function at redshift zero for both the prolonged-accretion model, and the chaotic-accretion model. The models are compared to the observed luminosity functions in the redshift range $0.4 < z < 0.68$ estimated from the 2dF (Croom et al. 2004) and 2dF-SDSS QSO survey (Croom et al. 2009). The two models agree with each other, although the prolonged-accretion model predicts a somewhat higher volume density of quasars in the $-21 \leqslant M_{b_{\rm J}} \leqslant -23$ and $-24 \leqslant M_{b_{\rm J}} \leqslant -25$ range. The inflection at $M_{b_{\rm J}} \simeq -24$ that separates the two regions is a reflection of the $10^8\,{\rm M}_\odot$ dip in the $M_{\rm BH} - a$ correlation seen in Fig. 2.9. Both models predict steeper faint end slope ($-20 \leqslant M_{b_{\rm J}} \leqslant -22$) than the observed luminosity functions. A similarly steep faint end is also seen in the soft X-ray luminosity function at $z \sim 0.4$ (Miyaji et al. 2001; Hasinger et al. 2005). The differences between the two models in this regime arises because the BHs in the prolonged model that contribute to the faint end have much higher spins, and thus higher bolometric luminosities than in the chaotic model.

In conclusion, we can reproduce the optical luminosity function reasonably well with either the chaotic or prolonged accretion models. A consistency check is provided by calculating the average accretion efficiency. Assuming only the accreting sources contributing to the quasar luminosity function we find $\langle\epsilon\rangle = 14.2\%$ ($\langle a\rangle = 0.86$) for the prolonged model and $\langle\epsilon\rangle = 6.1\%$ ($\langle a\rangle = 0.12$) for the chaotic model. The latter is in good agreement with $\langle\epsilon\rangle = 6.7\%$ inferred by optically selected AGN (Martínez-Sansigre & Taylor 2009) and consistent with the low efficiency that characterises accretion at $z = 0$ suggested by Wang et al. (2009).

2.7 AGN radio loudness and the spin paradigm

In this Section we investigate how the total radio output of an AGN is related to the accretion process and the central BH properties, and we present a model where we combine standard accretion disc theory (including ADAFs), BH evolution and radio jet production to understand the observed AGN radio loudness.

2.7.1 Modelling the jet emission in AGN

We construct a model for studying the radio loudness of AGN based on our current understanding of the formation and acceleration of jets. The starting point is the galaxy formation model described in Section 2.1. Galaxies become active every time the central SMBH experiences an accretion episode, allowing us to track the evolution of BH mass, spin and mass accretion rate distributions as described in the previous section. We combine this with the prescriptions for jet luminosity in the BZ model (Meier 2002). For consistency, we also investigate the more general case where the jet taps energy from both the BH and the accretion disc (Blanford & Payne 1982), which is described in the hybrid model presented by Meier (2001).

The BZ jet model

AGN jets in the BZ jet model are exclusively powered by extraction of the rotational energy of the BH and, thus, they are formed only in AGN hosting rotating SMBHs. The mechanical energy of a jet is proportional to the square of the poloidal magnetic field, $B_{\rm pol}$, at the horizon of the BH (Blandford & Znajek 1977),

$$L_{\rm jet} \propto B_{\rm pol}^2 M_{\rm BH}^2 a^2. \tag{2.36}$$

This is a second-order perturbative solution for the spin parameter a and is used to approximate the solution for slowly rotating BHs, $a \ll 0.998$. By including higher order corrections it can be shown that the dependance of $L_{\rm jet}$ on a can be much steeper for rapidly rotating BHs ($L_{\rm jet} \sim a^4$; Tanabe & Nagataki 2008; see also Tchekhovskoy et al. 2010 for a recent study of the dynamical range of $L_{\rm jet}$ predicted by these solutions). For this analysis we will adopt the original approximation of Blandford & Znajek (1977) for simplicity.

There have been several models that give the strength of $B_{\rm pol}$ around a rotating BH. In most cases, $B_{\rm pol}$ is expressed in terms of the azimuthal component, B_ϕ, as $B_{\rm pol} \approx (H/R)B_\phi$. Therefore, the strength of the jet depends critically on whether the disc is geometrically thin or thick. For ADAFs ($H \sim R$) and thin discs (TD; $H \ll R$), this yields

(see Meier 2002 and references therein):

$$L_{\rm jet,ADAF} = 2 \times 10^{45} \left(\frac{M_{\rm BH}}{10^9 M_\odot}\right) \left(\frac{\dot{m}}{0.01}\right) a^2 \ {\rm erg\ s^{-1}}, \tag{2.37}$$

$$L_{\rm jet,TD} = 2.5 \times 10^{43} \left(\frac{M_{\rm BH}}{10^9 M_\odot}\right)^{1.1} \left(\frac{\dot{m}}{0.01}\right)^{1.2} a^2 \ {\rm erg\ s^{-1}}. \tag{2.38}$$

In the super-Eddington regime ($\dot{m} \geq 1$), we assume that the flow remains in a thin disc state as there are as yet no models to describe the behaviour of the radio jet in this regime. The value of the viscosity parameter, α, in the ADAF and thin-disc regimes is set to 0.1. Note that, according to Eqn. (2.37) the mechanical jet power at the top of the ADAF branch is $L_{\rm jet} = a^2 L_{\rm bol} \sim 0.01 a^2 L_{\rm Edd}$ ergs s^{-1}. This upper limit to the jet luminosity in the ADAF regime is the origin of our revision to the fraction of the Eddington luminosity available for jet feedback into the halo. For low spin BHs, the BZ jet power drops substantially below this.

The hybrid jet model

In the BZ mechanism, the jet is assumed to be powered directly by the extraction of the rotational energy of the BH, neglecting any energy that could be extracted from the disc. However, the field lines frozen to the accreting matter on the disc may generate collimated outflows as a response to the differential rotation of the plasma, even in the case when the BH is not rotating (Blandford & Payne 1982). The outflow in this case is powered by the extraction of the rotational energy of the disc, rather than the BH. Thus, in the general case, both the disc and the hole could contribute to the production of jets.

Based on these considerations, Meier (2001) proposed a hybrid model for the radio loudness of AGN in which the jet luminosity depends on the rotation of both the BH and the accretion disc. The model includes two distinct accretion states, the ADAF and thin disc, in which the BH can be rotating or non-rotating. The hybrid model has a weaker dependence on the spin of the BH than the standard BZ mechanism. When $a \neq 0$ the jet luminosity scales with spin as

$$L^{\rm Kerr}_{\rm jet,ADAF} \propto (0.55 f^2 + 1.5 f a + a^2), \tag{2.39}$$

$$L_{\rm jet,TD}^{\rm Kerr} \propto (1 + 1.1a + 0.29a^2). \tag{2.40}$$

where f and g are parameter related to the angular velocity of the disc and the azimuthal magnetic field respectively (see Meier 2001 for more details; also Nemmen et al. 2007 for a fully relativistic account of the hybrid model). The model appears to be a more realistic interpretation of the jets seen from MHD simulations, since these are still able to power jets even from Schwarzschild BH accretion. We have tested this model by coupling it to our predicted spin distributions. However, we find that the weak dependence on spin in this model results in small dynamic range in radio luminosity, and the results are very similar to the predictions of the BZ jet model for the prolonged accretion case (see Section 2.8). We therefore prefer to contrast the prolonged accretion model with the chaotic accretion model coupled to the spin dependence of the BZ jet model.

2.7.2 From jet power to radio luminosity

The mechanical BZ jet luminosities presented in the previous section are converted into radio luminosities according to the theoretical calculations of Heinz & Sunyaev (2003) (see also Falcke et al. 1995). Heinz & Sunyaev derived the non-linear dependence between the jet flux and the physical parameters $M_{\rm BH}$ and $\dot{m}$ for radiatively efficient and inefficient flows. These authors found that the core flux at frequency, F_ν, of a jet scales as $M_{\rm BH}^{\xi_1}\dot{m}^{\xi_2}$, with $\xi_1 = \xi_2 = 17/12$ for ADAF systems and $\xi_1 = 17/12$, $\xi_2 = 0$ when the disc is radiation-pressure supported[4]. A similar dependence on the accretion rate and BH mass seems to be implied by the fundamental plane of BH activity in the case of radiatively inefficient discs (Merloni et al. 2003; Falcke et al. 2004). Hence, when jets are launched in ADAFs we assume that

$$L_{\rm R,ADAF} \propto (M_{\rm BH}\dot{m})^{1.42}. \tag{2.41}$$

When the ADAF collapses to a thin disc we assume that for the range of accretion rates we are interested in, $0.01 \leqslant \dot{m} \lesssim 100$, the flow is radiation-pressure supported and thus,

$$L_{\rm R,TD} \propto M_{\rm BH}^{1.42} \tag{2.42}$$

[4]The values for the scaling indices ξ_1 and ξ_2 are calculated for a flat spectrum.

Since we know how $L_{\rm jet}$ depends on $M_{\rm BH}$ and $\dot{m}$ we can work out the relation between $L_{\rm R}$ and $L_{\rm jet}$ for both accretion regimes. For example, in the BZ model, Eqns. (2.37) and (2.38) in combination with Eqns. (2.41) and (2.42) give

$$L_{\rm R,ADAF} = A_1 (M_{\rm BH}\dot{m})^{0.42} L_{\rm jet,ADAF}, \tag{2.43}$$

$$L_{\rm R,TD} = A_2 M_{\rm BH}^{0.32} \dot{m}^{-1.2} L_{\rm jet,TD}. \tag{2.44}$$

where A_1 and A_2 are normalisation constants. In order to constrain the values of these constants, we assume that $A_1/A_2 \simeq 100$ which arises from the fact that the mechanical power of a jet in an ADAF is approximately 100 times higher than that of a jet in a thin disc (Eqns. 2.37 & 2.38). A_1 is then constrained by fitting the predictions of each accretion model for the bright end of the radio luminosity function to the observations (see Section 2.7.4). When we consider the prolonged accretion model this gives $A_1 = 0.05$ and $A_2 = A_1/100 = 0.0005$. For the chaotic accretion model, $A_1 = 0.07$ and $A_2 = A_1/100 = 0.0007$. The uncertainty in the parameters A_1 and A_2 introduces an arbitrariness into the model, which, however, is unavoidable since the normalisation of $L_{\rm R}$ is not calculable from first principles.

2.7.3 The $\log L_{\rm B} - \log L_{\rm R}$ plane for a 10^8 $\rm M_\odot$ BH

The theoretical predictions of the BZ model for the evolution of AGN jets on the $\log L_{\rm B} - \log L_{\rm R}$ plane are illustrated in Fig. 2.11. The optical luminosity, $L_{\rm B}$, is obtained as discussed in Section 2.6. The jet strength is explicitly determined by the three fundamental parameters of our model, the spin, the accretion rate and the BH mass (and also by the values of the normalisation constants A_1 and A_2). The predictions of the models are shown for a BH mass of 10^8 $\rm M_\odot$ spinning at $a = 0.01, 0.1, 0.5$ and 0.998. The different accretion regimes are represented by different background shadings. As shown in the diagram, a BH that accretes through an ADAF develops jets whose radio luminosity increases with the accretion rate on the $\log L_{\rm B} - \log L_{\rm R}$ plane. When the accretion rate becomes higher than 0.01, the accretion flow enters the thin-disc regime and the jet collapses by a factor roughly equal to the difference in H/R between the two very different accretion flows.

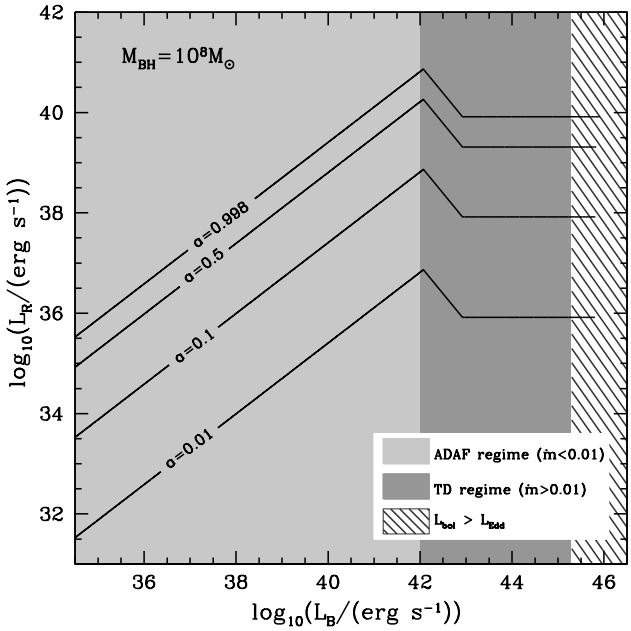

Figure 2.11: The predictions of the BZ model for the optical and radio luminosities of an AGN. Results are shown for an AGN hosting a SMBH with $M_{\rm BH} = 10^8$ $\rm M_\odot$ and rotating with spin $a = 0.01, 0.1, 0.5$ and 0.998. The viscosity parameter α is fixed to 0.1 in both the ADAF and thin-disc regimes. We represent the different accretion regimes with different background shadings. The sharp drop in radio luminosity seen in all cases is due to the transition from the ADAF to the thin disc regimes when the accretion rate exceeds $0.01 L_{\rm Edd}$. The rightmost shaded area depicts the region where accretion becomes super-Eddington. In this region, the optical luminosity is set to $(1+\ln \dot{m}) L_{\rm Edd}$. The discontinuity above 10^{42} $\rm erg\,s^{-1}$ in accretion luminosity is due to the fact that thin discs are radiatively efficient and thus, for the same accretion rate, are more luminous than an ADAF.

In the thin disc regime, the mechanical jet power increases with $\dot{m}$ but this does not translate into an increase in observed radio flux. Instead, the radio flux remains constant, while the optical flux increases with mass accretion rate. Thus, the much lower radio emission is sustained throughout the thin disc regime and we do not expect objects powered by thin discs to be radio loud. Our model extends this behaviour to super-Eddington mass accretion rates, although we note that this is almost certainly an underestimate of the jet and radio luminosities as H/R for such flows increases again to ~ 1. Thus, there is a clear accretion mode switch in the models. The brightest radio sources are the highest spin BHs accreting at the maximum rate for an ADAF. Since this is $L/L_{\rm Edd} = 0.01$, this maximum radio luminosity scales also with the mass of the BH.

2.7.4 The radio luminosity function

A first test of the jet model is the radio luminosity function of AGN. In Fig. 2.12 we show the predictions of the BZ jet model for the radio luminosity function in both the prolonged and chaotic accretion cases and compare with the estimates from the Two-degree-Field Galaxy Redshift Survey (2dFGRS; Sadler et al. 2002) and from the SDSS (Best et al. 2005)[5]. The model radio luminosity function is derived for systems powered by ADAFs and thin discs, including super-Eddington objects, in a simulation volume of $V = 1.25 \times 10^8\ {\rm Mpc}^{-3}$.

The coupling between the different spin distributions and the BZ mechanism gives interestingly different predictions for the two accretion models. The chaotic model shows a fairly good agreement with the observations throughout the entire energy spectrum. The faint end is dominated mainly by galaxies that host slowly rotating BHs whereas the bright end is dominated by galaxies that host rapidly rotating massive BHs. The majority of these BHs accrete in the hot-halo mode. A characteristic break in the slope at $\sim 10^{25}$ W Hz^{-1} separates the two regimes.

In contrast, in the prolonged accretion case the same sample of galaxies shows a different distribution of luminosities. The model overproduces the number density of faint radio sources by a factor of ~ 3 compared to the chaotic model, due to the fact

[5]The results from 2dFGRS have been adjusted to the cosmology adopted by Best et al. (2005).

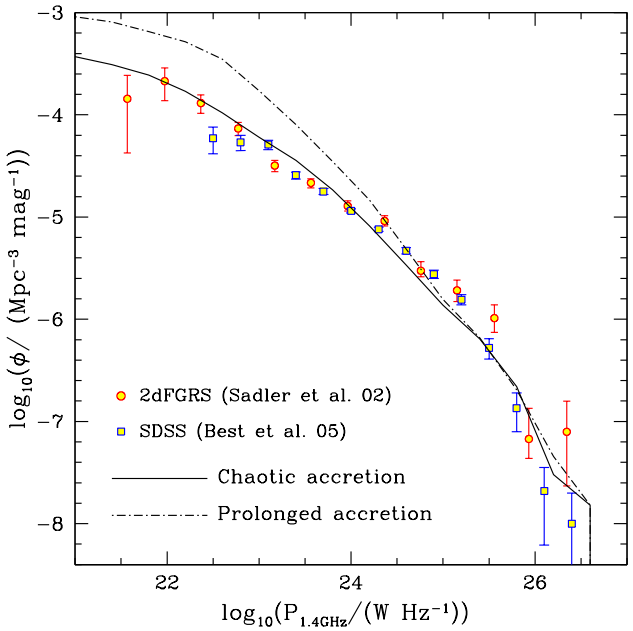

Figure 2.12: The radio luminosity function of AGN at 1.4 GHz. The lines show our model predictions for the prolonged (dashed-dotted) and chaotic (solid) accretion models. The symbols show observational measurements for the local radio luminosity function from Sadler et al. (2002) for the 2dFGRS (circles) and Best et al. (2005) for the SDSS (boxes). The predictions of the BZ model, in combination with the chaotic accretion model, reproduce the observed radio luminosity function reasonably well.

that these luminosity bins are populated by galaxies with rapidly rotating BHs whose radio luminosity is too larger. This trend extends down to luminosities of 10^{25} W Hz^{-1}. Above that luminosity, the model is in reasonably good agreement with the observations. Since the mechanism that spins those BHs up, namely the BH mergers, is present in both models, the two predicted luminosity functions agree with each other very well at $10^{25} - 10^{26}$ W Hz^{-1}. Note that the parameters A_1 and A_2 introduced in Section 2.7.2 affect only the normalisation of the radio luminosity function. The shape is a prediction of the model and depends only on the distribution of BH masses, spins, and accretion rates.

2.8 Predictions for the $L_{\rm B} - L_{\rm R}$ AGN activity

2.8.1 The distribution of galaxies on the optical–radio plane

We now explore the distribution of AGN on the $\log L_{\rm B} - \log L_{\rm R}$ plane. We consider a sample of galaxies brighter than $L_\star$ ($M_{\rm V} \simeq -20.5$). This distribution is displayed in Fig. 2.13, where we plot the B-band versus the radio luminosity of AGN for both the prolonged and chaotic accretion models (left and right plots respectively). All galaxies are volume weighted and those accreting through a thin disc are weighted according to the fraction of their lifetime during which they are active. The colour coding corresponds to different types of accretion: blue shows AGN powered by an ADAF, red those powered by a thin disc and green indicates the super-Eddington objects.

Along with the model predictions, we plot the radio and optical luminosities of a sample of AGN-powered radio sources studied by Sikora et al. (2007). We include only local objects i.e. those at $z < 0.14$, so this excludes the very brightest radio and optical sources. The evolution of the sources across cosmic time will be explored in a future study.

The data form two distinct sequences on the $\log L_{\rm B} - \log L_{\rm R}$ plane. The upper sequence represents radio-selected galaxies and the lower sequence optically-selected objects. The objects in the upper sequence are on average ~ 3 orders of magnitudes more radio loud than those in the lower sequence. These radio bright objects are Fanaroff and

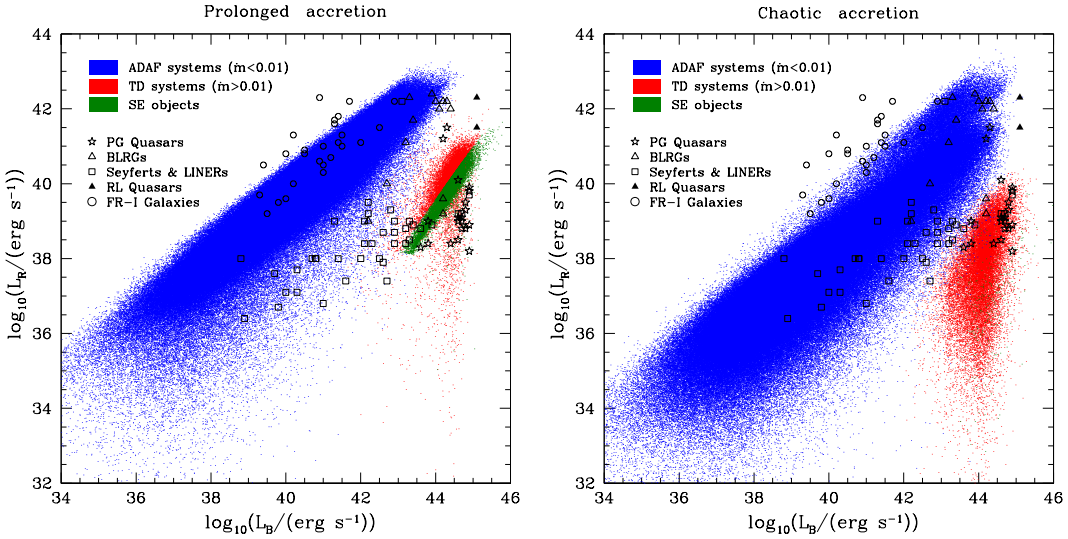

Figure 2.13: Radio luminosity *vs*. B-band nuclear luminosity for the BZ model in (a) the prolonged and (b) the chaotic accretion models. Only galaxies with $z < 0.14$, $M_{\rm V} < -20.5$ and $M_{BH} > 10^6 {\rm M}_\odot$ are shown. The blue points represent galaxies whose SMBHs accrete via an ADAF. These include galaxies experiencing *both* the hot-halo and starburst modes. The red points represent galaxies powered by thin discs around SMBHs. The green points denote super-Eddington objects. The observational data are taken from Sikora et al. (2007): BLRGs are shown by open triangles; radio-loud quasars by filled triangles; Seyfert galaxies and LINERs by open squares; FRI radio galaxies by open circles; and PG Quasars by open stars.

Riley class I (FR-I) galaxies, broad line region galaxies (BLRGs) and radio loud quasars (RLQs). These are thought to be powered by very massive BHs (Mclure & Dunlop 2002), hosted by elliptical galaxies. Objects in the lower, radio-quiet sequence include Seyferts, low ionisation emission regions (LINERs) and radio-quiet quasars (RQQs).

The observational data suffer from multiple selection effects, which may be responsible for the apparent dichotomy seen in the distribution (see discussion by Sikora et al. 2007). The fact that some FRI galaxies have much higher radio power than predicted by our model could be due to the fact that these data include *lobe* power, whereas we only model the *core* radio emission. However, the locus of the data points sets upper limits for the radio luminosity of radio-quiet and radio-loud objects, and provides a rough visual description of the general bulk properties of the different populations.

In both accretion models, AGN span a wide range of optical and radio luminosities. AGN powered by ADAFs generically produce more radio and less optical emission than those powered by a thin disc. Thus, the accretion mode switch at $\dot{m} = 0.01$ from ADAF to thin disc produces a marked transition in radio loudness. All our models show that the radio-loud sequence lies at the upper end of the radio luminosity envelope for SMBH accreting via a hot flow. Conversely, the radio-quiet locus lies predominantly on the thin disc points, although the lowest luminosity radio-quiet AGN (LINERS) lie on the lower end of the ADAF regime. Thus, the *major* switch between radio–loud and radio-quiet is the change in jet properties as the accretion flow collapses from a hot, geometrically thick configuration, to a cool, geometrically thin disc (Jester 2005).

Nonetheless, there can also be an additional spin dependence which enhances the difference in radio properties, although this depends strongly on the details of the jet modelling and the spin distribution. The BZ jet models are strongly dependent on spin, so their radio luminosity amplifies differences in the spin distribution. In the prolonged accretion model almost all SMBHs have maximal spin, so there is little dispersion in radio flux. Conversely, for the chaotic model, the correlation between mass and spin means that the low mass and hence lower optical luminosity objects have dramatically lower radio power than the higher mass BH in both the ADAF and thin disc regime.

There are also subtle differences in optical luminosity between the prolonged and

chaotic models, as the higher efficiency of high spin accretion means that the same mass accretion rate gives rise to a higher luminosity. Thus, there are more super-Eddington sources in the prolonged accretion model, in which low mass objects have high spin, than in the chaotic model.

2.8.2 The distribution of galaxies on the $\mathcal{R} - \lambda$ plane

In addition to the AGN optical and radio output, the model allows us to study how the *radio loudness* $\mathcal{R}$ of AGN depends on various physical parameters such as the BH mass and the Eddington ratio $\lambda = L_{\rm bol}/L_{\rm Edd}$. The radio loudness measures the radio to optical flux ratio, $\mathcal{R} \equiv L_{\nu_{\rm R}}/L_{\nu_{\rm opt}}$ (Richards et al. 2006). Following the definition of $\mathcal{R}$ in Sikora et al. (2007), we consider the total radio flux at 5GHz, $L_R = \nu_{5_{\rm GHz}} L_{\nu_{5_{\rm GHz}}}$, and therefore we express the radio loudness as $\mathcal{R} = (\nu_{\rm B}/\nu_{5_{\rm GHz}}) \times L_{\rm R}/L_{\rm B} = 1.36 \times 10^5 L_{\rm R}/L_{\rm B}$, given that the B-band is centred at a wavelength of 4400Å.

We plot the theoretical predictions for the radio loudness of the AGN in our sample along with the observational data set of Sikora et al. (2007) in Fig. 2.14. Our predictions suggest a clear inverse correlation between $\mathcal{R}$ and λ with a substantial scatter in both accretion models (upper panels in Fig. 2.14). In the ADAF regime, the distribution of objects shows a correlation of the form $\mathcal{R} \propto \lambda^{-0.4}$ (one can derive the correlation between $\mathcal{R}$ and λ using Eqns. (2.43), (2.37) and (3.4)) which is driven mainly by the strong dependence of the disc luminosity on the accretion rate, $L_{\rm bol} \propto \dot{m}^2$. The correlation between $\mathcal{R}$ and λ becomes steeper in the thin-disc regime, where the data approximately follow $\mathcal{R} \propto \lambda^{-1}$. The dependence of $\mathcal{R}$ on λ in the thin-disc regime arises from $\mathcal{R} \propto L_{\rm bol}^{-1} \propto \dot{m}^{-1} \propto \lambda^{-1}$.

In both models, the radio-quiet AGN ($\log \mathcal{R} < 1$, following Ho 2002) are preferentially found in the $\log \lambda \gtrsim -2$ regime, while the radio-loud sources ($\log \mathcal{R} > 1$) populate exclusively the $\log \lambda \lesssim -2$ regime. When compared to the data from Sikora et al. (2007), the predictions of the chaotic model give an adequate representation of the AGN on the $\mathcal{R} - \lambda$ plane. The model reproduces well the loci of the different AGN populations and the slope of the overall distribution. Objects such as quasars and Seyferts are radiating at $\sim (0.01 - 1) L_{\rm Edd}$, while the radio galaxies are characterised by very low sub-Eddington

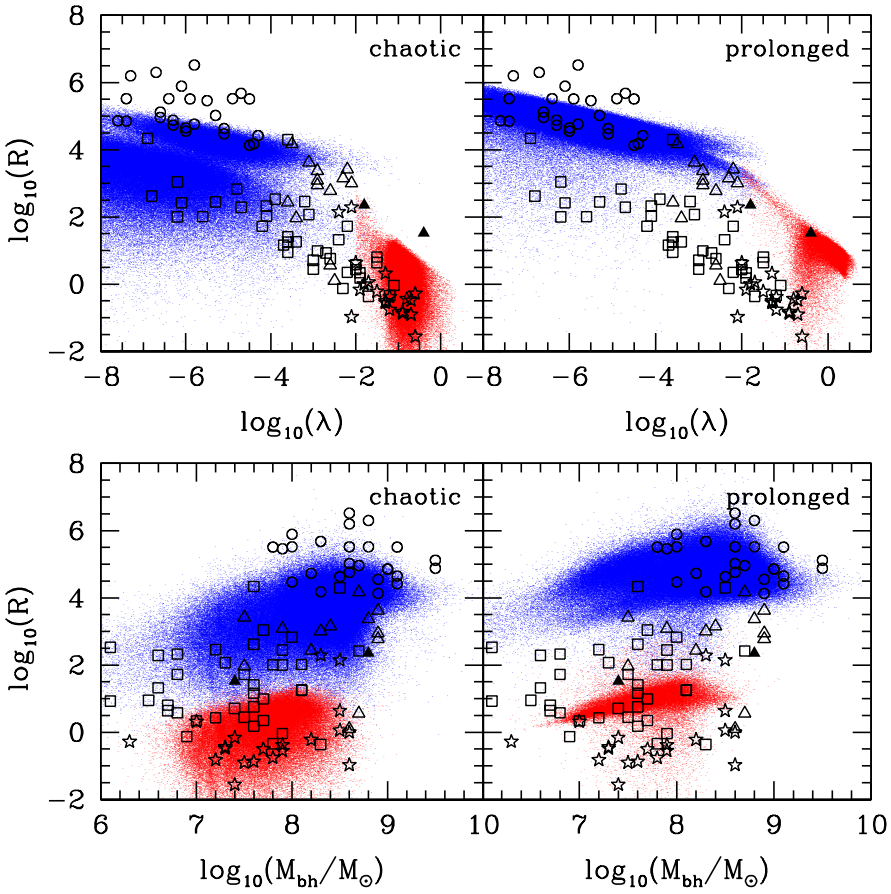

Figure 2.14: Scatter plots of radio loudness ($\mathcal{R} = (\nu_{\rm B}/\nu_{5_{\rm GHz}}) \times L_{\rm R}/L_{\rm B}$) *vs.* BH mass (top panels) and λ parameter (bottom panels) in the chaotic and prolonged accretion models for the sample in Fig. 2.13 (galaxies with $z < 0.14$, $M_{\rm V} < -20.5$ and $M_{\rm BH} > 10^6 {\rm M}_\odot$). Different colours represent different accretion regimes: blue for ADAF systems and red for thin-disc systems. The observational data are taken from Sikora et al. (2007): BLRGs are shown by open triangles, radio-loud quasars by filled triangles, Seyfert galaxies and LINERs by open squares, FRI radio galaxies by open circles, and PG Quasars by open stars.

luminosities ($< 0.01 L_{\rm Edd}$).

By contrast, in the prolonged model there is an absence of objects with $\log \mathcal{R} < 3$ in the $-4 \lesssim \lambda \lesssim 3$ regime. This is mainly because most objects pile up in the upper envelope of the distribution due to their high radio luminosities (and BH spin values). We note again that FR-I galaxies (open circles) have higher values of radio loudness than the models. This could be due to the fact that the measured radio luminosities for these objects include power from the lobes.

The objects in our sample populating the radio-loud part of the $\mathcal{R} - \lambda$ plane are associated mainly with giant ellipticals that host very massive BHs (see below). Accretion onto these BHs in the ADAF regime produces significant radio power because the spin is very high. In combination with the low optical luminosities of these objects, this gives rise to very high $\mathcal{R}$ values. Therefore, these specific properties of the host of the radio-loud AGN may suggest a correlation between $\mathcal{R}$ and $M_{\rm BH}$. However, when we plot $\mathcal{R}$ versus $M_{\rm BH}$ (lower panels in Fig. 2.14) we find that in both models there is no apparent correlation between these two quantities. The data display significant scatter along the $M_{\rm BH}$ axis which is due to the complex dependence of $\mathcal{R}$ on $M_{\rm BH}$ through the optical and jet luminosity expressions in Eqns. (2.43), (2.44), and (3.4). Both models reproduce the loci of the different AGN population in the Sikora et al. data set remarkably well. ADAF systems, mainly identified with radio-loud sources, span a wide range of BH masses ($10^6 - 10^{10}$ $\rm M_\odot$). In contrast, radio-quiet objects have BH masses in the range $\sim 10^7 - 3 \times 10^8$ $\rm M_\odot$. Finally, in both models all the sources hosting BH with $M_{\rm BH} \gtrsim 3 \times 10^8$ $\rm M_\odot$ are exclusively radio-loud.

2.8.3 A physical view of the "chaotic accretion" population

While both accretion models give a fair representation of the locus of the heterogeneous radio-optical data points from Sikora et al. (2007), the chaotic accretion model provides a better fit to the much more homogeneous data from the radio luminosity function described in Section 2.7.4. Hence, in this section, we focus on the chaotic accretion model and explore the results in greater detail.

In order to gain further insight into the predictions of the model, we show in Fig. 2.15

how the main parameters that determine the radio loudness of an AGN, a, $M_{\rm BH}$ and $\dot{m}$, are distributed across the $\log L_{\rm B} - \log L_{\rm R}$ plane for the chaotic accretion model.

Comparing these plots to the data in Fig. 2.13, the brightest radio-loud galaxies i.e. FR-I and BLRG, are identified with very massive ($10^8 - 10^9$ $\rm M_{\odot}$), rapidly rotating BHs (spins $\gtrsim 0.8$) accreting at the top of the ADAF branch at $\dot{m} \sim 0.01$. In our galaxy formation model, these objects are hosted exclusively by giant ellipticals and their central BHs grow through mergers and through the hot-halo mode. The radio loud quasars (only 2 in our volume) are the extreme end of this population, and can be matched by the highest mass objects in our sample. One issue with identifying these objects with the ADAF branch is that they typically have high excitation spectra, showing that there is a bright UV disc (see e.g. Marchesini, Celotti & Ferrarese 2004). However, the top of the ADAF branch is where the transition to a thin disc takes place. Observations of stellar mass BH binary systems show that this transition is complex, probably taking on a composite structure with the thin disc replacing the hot flow at progressively smaller radii (see e.g. the review by Done, Gierlinski & Kubota 2007). Thus, better modelling of the details of the transition may well be able to reproduce the required UV ionising spectrum.

The Palomar-Green (PG) Quasars are mostly concentrated at the top end of the narrow thin disc sequence, extending from $\sim 10^{43}$ to $\sim 10^{45}$ $\rm erg\,s^{-1}$ in optical luminosity and from $\sim 10^{38}$ to $\sim 10^{40}$ $\rm erg\,s^{-1}$ in radio luminosity. The higher mass accretion rates required to accrete via a thin disc are only generally possible in lower mass BHs, $10^7 - 10^8$ $\rm M_{\odot}$ (see Fig. 2.4), so these have similar optical luminosities to the top of the ADAF branch as their higher mass accretion rate is partially cancelled by the lower mass BHs. These lower mass BHs are hosted in lower mass galaxies, predominantly spirals, and have lower spin, but the majority of the suppression in radio power comes from the ~ 2 orders of magnitude stronger jet emission in the ADAF regime than in the thin disc regime at $\dot{m} = 0.01$. However, a few of the optically brightest radio quiet objects are powered by Eddington (or even super-Eddington) accretion onto 10^8 $\rm M_{\odot}$ BHs, and these could be hosted by ellipticals.

Seyfert and LINER galaxies constitute an interesting sample in our model because of their heterogeneity. Those exhibiting high nuclear luminosities ($L_{\rm B} \gtrsim 10^{43}$ $\rm erg\,s^{-1}$)

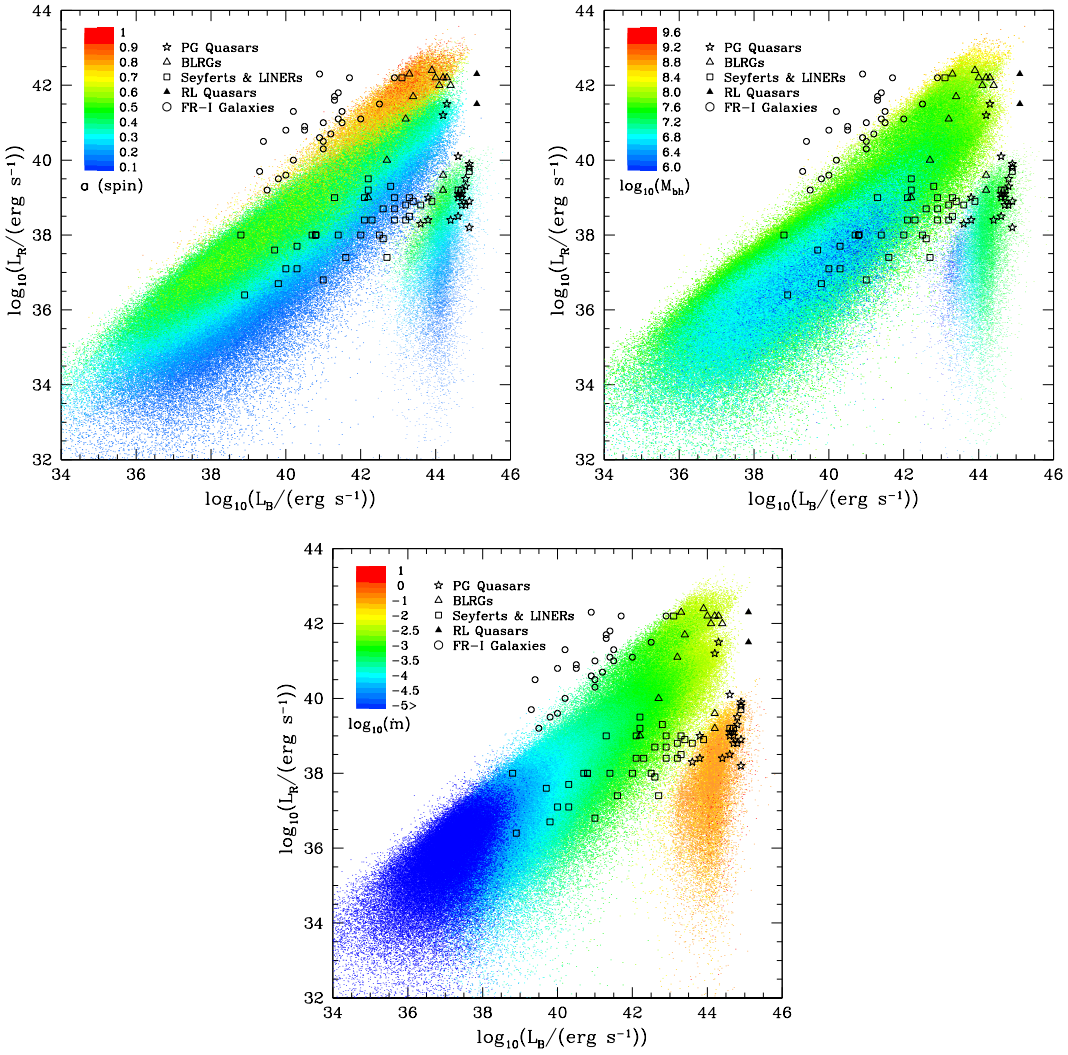

Figure 2.15: Scatter plot of radio luminosity *vs.* B-band nuclear luminosity for the chaotic accretion model (as in Fig. 2.13), with model points coloured-coded according to BH spin (left top), mass (right middle) and accretion rate (bottom). The colours represent different ranges of values as indicated in each key.

(mainly Seyferts), appear to occupy both the ADAF and thin-disc regimes, whereas those with lower luminosities (LINERs) are generally powered by an ADAF. These are the most numerous type of AGN seen in the local Universe. The majority of these objects have BHs with masses of $10^7 - 10^8$ $\mathrm{M}_\odot$. Thus, they have low-to-moderate spin and are relatively quiet at radio luminosities. These are the same population of objects as the PG Quasars, but at lower mass accretion rates.

2.9 Discussion

The process of BH growth in our model is dominated by the accretion of large amounts of gas that allow a BH to double its mass several times during a Hubble time. The evolution of the spin of the BH is strongly influenced by the nature of the accretion episodes. It is often assumed that BHs accrete gas via a disc with constant angular momentum. In this case (the prolonged accretion model), BHs are systematically spun up during accretion, with most of them ending up with maximal spin. Even minor mergers or disc instabilities, typical of the growth of the bulge of spiral galaxies, can trigger a gas flow onto the BH of mass comparable to that of the BH itself and thus lead to $a = 1$. By contrast, if the accreting material fragments at its self-gravity radius and the associated star formation randomises the angular momentum direction of each of the fragments (the chaotic accretion model), then accretion proceeds in multiple *randomly oriented* episodes. This results in a low spin BH. However, for the most massive BHs, the major growth channel is not accretion but BH-BH mergers, and these generate fairly rapid spins of $0.7 - 0.8$. Thus, in the prolonged accretion model, the most massive BHs have slightly lower spin than the bulk of the BH population, whereas in the chaotic model they have larger spin.

Our results for the spin distributions are in good agreement with those of Berti & Volonteri (2008). However, our predictions for the prolonged-accretion model deviate significantly from the results of Lagos et al. (2009). These authors obtain a strong spin bimodality when they consider accretion of gas via an accretion disc of constant angular momentum. The difference between the two approaches stems from the different

amounts of cold gas available for accretion in the two models (see Kim et al. 2010 for a recent study of the cold-gas abundance in the Bower et al. 2006 model). In the original Bower et al. (2006) model and in the updated version that we have adopted in this study, the typical amount of cold gas accreted by a $10^6 - 10^8$ $\mathrm{M}_\odot$ BH is enough to spin it up to the maximum value. This is not true, however, for the Lagos et al. model where cold gas accretion includes several episodes with $M_{\rm gas} < M_{\rm BH}$ that do not spin up the BH efficiently. The difference in the final spin distributions illustrates the impact of the underlying galaxy formation model on the inferred properties of the BHs at the centre of galaxies.

We have used the resulting distributions of BH mass, spin and mass accretion rate to calculate the properties of AGN, assuming that any accretion at a rate $\dot{m} < 0.01$ proceeds via an ADAF, while accretion at higher rates forms a standard thin disc. The optical luminosity is then fairly straightforward to calculate, but the radio luminosity depends on the jet model. This is poorly understood, but both observations and theoretical models agree that the collapse of the thick ADAF into a thin disc leads to a similar collapse of the jet emission by several orders of magnitude. Thus, there is already a clear accretion mode switch in radio-loudness predicted by these models (Maccarone, Gallo & Fender 2003; Jester 2005).

The main issue then is how jet power couples to spin. In the prolonged accretion model, there is a very small range in spin since all BHs are spinning rapidly. Thus, *independently of the detailed jet model*, the slope of the radio luminosity function is directly given by the relative numbers of low and high mass BHs accreting in the ADAF regime. This is steeper than observed since lower mass BH are much more numerous than higher mass ones. Instead, in the chaotic accretion model, the observed radio luminosity function can be reproduced *if the jet power depends strongly on spin*. The a^2 dependence on spin power in the BZ jet models is sufficient to make a large difference in radio luminosity between the numerous low mass, low spin BHs and the much rarer high mass, high spin BHs. This model reproduces the shape of the observed radio luminosity function very well.

A mass-spin correlation was also suggested by Sikora et al. (2007) to explain the range

in the radio-to-accretion disc luminosity ratio seen in their (very heterogeneous) sample of AGN. However, the model they propose to establish this correlation is rather different from ours which is based on an actual calculation of galaxy formation from CDM initial conditions. Instead, Sikora et al. speculated that the high spin resulted from major mergers which triggered large gas flows with constant angular momentum direction onto the nucleus, spinning up the BH and producing an elliptical galaxy. Conversely, they argued that low spin resulted from minor mergers of randomly aligned satellite galaxies (a random walk with spin up, spin down). These leave the galactic gas disc intact, producing a spiral galaxy. However, as discussed above, since most of the mass comes from the disc of the host galaxy, even minor mergers result in enough gas flowing to the centre to spin the BHs up to maximal. Fragmentation and chaotic accretion are necessary in order to produce low-spin BHs. Major mergers are indeed the key to the high spin of the most massive BHs, but this is the result of BH-BH mergers, not of gas accretion.

One of the distinguishing features of our work is that the properties of the BHs and their associated AGN are calculated *ab initio* within the context of a full model of galaxy formation in a ΛCDM universe. This model has been shown to agree with a large variety of observational data such as galaxy luminosity functions in various passbands and at different epochs, galaxy colours, the cosmic star formation history and structural scaling properties such as the Tully-Fisher relation and the $M_{\rm BH} - \sigma$ relations (Bower et al. 2006). In this work we have augmented the galaxy formation model with calculations of BH spin and of the optical and radio output during accretion onto the BH. The two different accretion models we have explored (prolonged and chaotic) span the range of likely spin distributions and are good templates to investigate how the optical and radio luminosities of accreting systems depend on BH spin. As shown in Sections 2.7 and 2.8 and discussed in the previous paragraphs, the chaotic model gives a reasonable overall match to the observations, suggesting that a model in which BH spins develop a bimodal distribution is the most plausible.

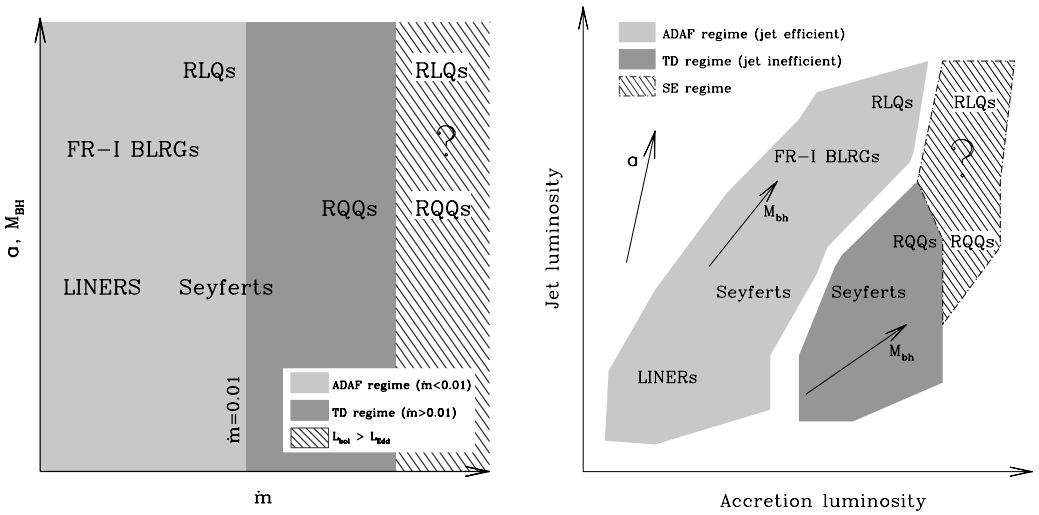

Figure 2.16: Left: the location of the different AGN types on the fundamental parameter $(a, \dot{m}, M_{\rm BH})$ plane. The a and $M_{\rm BH}$ axes have been merged into one since the two parameters are correlated as shown in the right hand plot of Fig. 2.9 in the chaotic accretion model. The shaded areas represent the different accretion regimes indicated by the keys. Right: the location of the different AGN types on the optical – radio plane. The shaded areas represent different accretion regimes. The arrows show how the physical parameters vary on the plane. Radio galaxies and LINERs lie in the ADAF regime. Seyferts are preferentially found in the thin-disc regime, even though a substantial population of Seyferts may be powered by an ADAF. RQQs accrete at relatively higher accretion rates than Seyferts and RLQs lie at the top of the ADAF branch. We speculate that some of the latter may be found also in the super-Eddington regime.

2.10 A unification scheme for the AGN activity

Finally, we present an interpretation of the optical and radio signatures of an active nucleus at different evolutionary stages of the host galaxy within a chaotic accretion framework. This is illustrated schematically in Fig. 2.16, where we show the relative position of the different types of active galaxies on the fundamental parameter (a, $\dot{m}$ and $M_{\rm BH}$) plane (left panel; the a and $M_{\rm BH}$ axes have been merged into one since the two quantities correlate as shown in the right-hand panel of Fig. 2.9) and the jet/accretion-luminosity plane (right panel). We also speculate on the outcome of super-Eddington accretion. Such objects are rare in the local Universe, but are increasingly important at higher redshift (see Fig. 2.3).

We start by considering the sources with the lowest mass BHs. During a minor galaxy merger, cold gas from the disc is transferred to the bulge, triggering star formation and BH growth. This process represents a natural mechanism for the gradual growth of spheroids in spiral galaxies (Parry et al. 2009). Accretion of gas onto the BH usually occurs at sub-Eddington rates through a thin disc which turns the host spheroid into the bright nucleus of a Seyfert galaxy. The bright UV flux from this disc produces a strongly ionising spectrum, resulting in strong emission lines. However, gas flows close to the disc may also contribute to the emission (or absorption) spectrum of the nucleus. The orientation of the central engine relative to a distant observer may have an important impact on the observed spectral features of the source and could account for the Type 1 and 2 sub-classification of Seyferts.

If the host galaxy experiences a major merger or a galactic disc instability then the entire galactic gas disc is assumed to lose most of its angular momentum, participate in a starburst and is added to the stellar spheroid mass. This supplies the central region of the galaxy with large amounts of cold gas that feed the SMBH with several solar masses of material per year at a near- or super-Eddington rate. Thus, the nucleus becomes exceptionally luminous, resulting in a quasar. The collapse of the cold gas reservoir also initiates an intense starburst which could be contemporaneous with the quasar phase. However, during the quasar phase, the galaxy is normally too dim to be seen against

the vast amounts of radiation produced by the central engine. The radio output of the central engine when the accretion rate becomes super-Eddington is not clear since the analytic solution used for this regime used in our model is not expected to be valid. Perhaps if the magnetic field strength close to the BH is enhanced due to a transition to a thick disc when the flow exceeds the Eddington limit, strong jets may be launched establishing the galaxy as a RLQ.

The duration of quasar activity is usually a few hundred million years. At the end of it (and the associated starburst), the system will have consumed or ejected its cold gas leaving a stellar bulge. In most halos, the ejected gas falls back into the galaxy and a new galactic disc is formed on a dynamical timescale. Further gas accretion, or galaxy mergers, may subsequently trigger another period of quasar activity and initiate a new growth era for the SMBH. Eventually, the halo may grow massive enough that gas is no longer able to cool rapidly and the halo enters the hydrostatic cooling regime. In this case, the end-product may be an elliptical galaxy in which further gas cooling is restricted by the hot-halo mode feedback. By construction, this accretion onto the BH takes place in the ADAF regime and the host elliptical appears as a radio galaxy. In the extreme case where the accretion occurs at the top of the ADAF branch and the central SMBH is rapidly rotating the galaxy is identified as a RLQ. The orientation of the central engine and jets may explain the different subcategories of RLQs. For example, if the jet axis lies close to the line-of-sight of a distant observer, the source may be visible as a blazar.

2.11 Conclusions

In this chapter we have presented a model of AGN activity in which the evolution of the galaxy is calculated in its full cosmological context and the luminosity of AGN at radio and optical wavelengths is calculated using a model for gas accretion and the generation of jets. We first considered the evolution of SMBH spin. We have found that the different astrophysical processes that influence the growth of SMBHs have a significant effect on the global spin distribution. For example, if accretion of gas of constant angular

momentum dominates the growth of SMBHs, the associated holes will be rapidly rotating. However, if the gas that is fed into the SMBH has random angular momentum, a bimodal spin distribution results. In this case, high spin values occur only for the most massive BHs ($\gtrsim 10^8$ $\mathrm{M}_\odot$), and these are mainly due to gas poor major mergers, where the BH growth is dominated by the BH-BH merger.

We have coupled this mass, spin and mass accretion rate evolution to a model for the accretion flow and jet. The accretion flow is assumed to form a geometrically thick, hot, radiatively inefficient flow (ADAF) for $\dot{m} < 0.01$, and to collapse to a thin disc at higher mass accretion rates. The jet power couples strongly to the accretion mode since it depends on the vertical (poloidal) magnetic field component close to the BH horizon. The collapse by two orders of magnitude in the scale height of the flow results in a similar drop in radio power. This already produces a dichotomy in radio properties which explains the distinction between radio-loud and radio quiet objects.

However, we also find that for our model to match the slope of the observed radio luminosity function, it is necessary for low mass BHs to generate relatively less jet power than high mass BHs. This is readily achieved in models where the jet couples *strongly* to spin, such as in the classic BZ jet mechanism, *and* where lower mass BHs have lower spin than the most massive BHs, as in our chaotic accretion model.

Coupling the chaotic accretion model to the BZ jet mechanism results in an AGN population which reproduces the diversity of nuclear activity seen in the local Universe. In particular, the model accounts for the radio and optical luminosities of the FR-I, BLRG, Seyfert and LINER galaxy populations. This is the first consistent demonstration that a great part of the phenomenology of AGN can be naturally explained by the coeval evolution of galaxies and BHs, coupled by AGN feedback, in a CDM universe. In future work, we will address the evolution of AGN across cosmic time, as a crucial test of galaxy formation models.

Chapter 3

The evolution of AGN across cosmic time

3.1 Introduction

In this chapter we present a study of the evolution of AGN using the model developed in Chapter 2. Our aim is to provide a robust framework for understanding the downsizing of AGN within a self-consistent galaxy formation model. For the purposes of this analysis we introduce improvements to the model that allow us to obtain a better match to the observations. We then study in detail the evolution of BH mass and explore the scaling relations predicted between the BH mass and the mass of the host galaxy mass and DM halo. We present the essential ingredients of the AGN model and study the evolution of the physical properties which, together with the mass, provide a complete description of accreting BHs. Finally, we show our predictions for the evolution of the optical, soft/hard X-ray and bolometric LFs and explore the downsizing of AGN in our model.

In Chapter 2 we extended `GALFORM` to track the evolution of BH spin, a. By predicting the spin we can compute interesting properties such as the efficiency, ϵ, of converting matter into radiation during the accretion of gas onto a BH and the mechanical energy of jets in the Blandford and Znajek (1977) and Blandford and Payne (1982) mechanisms. To calculate the evolution of a we use the chaotic accretion model. In this model, during the active phase gas is accreted onto the BH via a series of randomly oriented accretion discs, whose mass is limited by their self-gravity (King et al., 2005). We choose the chaotic model (over the alternative prolonged model in the literature by Volonteri et al.

Table 3.1: Summary of the revised parameter values in the variants of the Bower et al. model considered here.

Study	$f_{\rm Edd}{}^a$	$\tilde{\epsilon}_{\rm kin}{}^b$	$f_{\rm BH}{}^c$
Fan10b (this model)	0.039	0.016	0.005
Fan10a (Chapter 2)	0.01	0.1	0.017

Notes. ^{a}Fraction of the Eddington luminosity available for heating the gas in the host halo. ^{b}Average kinetic efficiency during the hot-halo mode. ^{c}Ratio of the mass of cold gas accreted onto the BH to the mass of cold gas used to form stars.

2007) since in this case the predicted BH spin distributions, through their influence on the strength of relativistic jets, reproduce better the population of radio-loud AGN in the local Universe (see Chapter 2).

With this extension to the Bower et al. (2006) model, we were able to reproduce the diversity of nuclear activity seen in the local universe. Furthermore, we demonstrated that the bulk of the phenomenology of AGN can be naturally explained in a ΛCDM universe by the coeval evolution of galaxies and BHs, coupled by AGN feedback. In this chapter we aim to extend the predictive power of the model to high redshifts and different wavelengths, to provide a complete and self-consistent framework for the formation and evolution of AGN in a ΛCDM cosmology.

For completeness, we now list the model parameters which have an influence over the growth of BH mass:

(i) $f_{\rm BH}$, the fraction of the mass of stars produced in a starburst, after taking into account SN feedback and the recycling of gas, that is accreted onto the BH during the burst.

(ii) $f_{\rm Edd}$, the fraction of the Eddington luminosity of an accreting BH that is available to heat the hot halo during an episode of AGN feedback.

(iii) $\tilde{\epsilon}_{\rm kin}$, the average kinetic efficiency of the jet during the hot-halo mode.

The fiducial model in this study is denoted as Fan10b. We adopt the values for the above parameters that were used in the Bower et al. (2006) model, as listed in Table 3.1

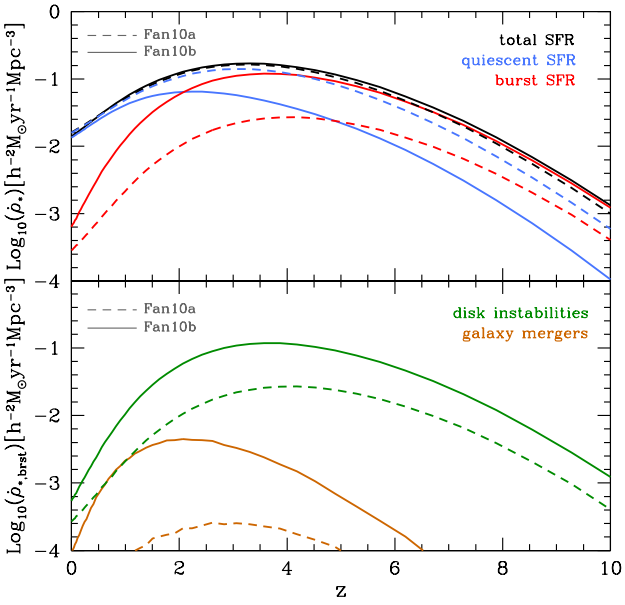

Figure 3.1: Top: The cosmic history of the total SFR density (black lines) in the Fan10b (solid line) and Fan10a (dashed line) models. Also shown is the contribution from each SF activity mode, namely burst and quiescent SF (red and blue respectively), to the total SFR density. Bottom: The contribution of disc instabilities (green lines) and galaxy mergers (orange lines) to the cosmic history of SFR density in the burst SF activity mode for the Fan10b (solid lines) and Fan10a (dashed lines) models.

against the Fan10b model. In the previous chapter we made some small changes to these parameter values, which are given in the Fan10a entry in Table 3.1. These changes resulted in a small change in the distribution of accretion rates in the hot-halo mode. By reverting to the original parameter values used in the Bower et al. model, we note that there is a small tail of objects accreting in the hot-halo mode, for which the accretion rate is higher than that typically associated with ADAFs.

3.2 A new star–formation law

A further difference between our fiducial model, Fan10b, and the Fan10a model is the use of an improved star–formation (SF) law. Following Lagos et al. (2010), who implemented a range of empirical and theoretical SF laws into GALFORM, we use the SF law of Blitz & Rosolowsky (2006, hereafter BR06). Lagos et al. found that this SF law in particular improved the agreement between the model predictions and the observations for the mass function of cold gas and the cold gas to luminosity ratio as a function of B-band magnitude. The BR06 model has the attraction that it is more physical than the previous parametric SF law used in Bower et al., and agrees with observations of the surface density of gas and SF in galaxies.

The BR06 law distinguishes between molecular and atomic hydrogen, with only the molecular hydrogen taking part in SF. The fraction of hydrogen in molecular form depends on the pressure within the galactic disc, which in turn is derived from the mass of gas and stars and the radius of the disc; these quantities are predicted by GALFORM. The BR06 SF law contains no free parameters once it has been calibrated against observations. We adopt a value for the normalization of the surface density of SF that is two thirds of the value used by Lagos et al., but which is still within the observational uncertainty. We do this to improve the match to the observed quasar luminosity function.

As shown by Lagos et al., the adoption of the BR06 SF law changes the SF history predicted by the model. This is due to a much weaker dependence of the effective SF timescale on redshift with the new SF law, compared with that displayed by the Bower et al. model. This leads to the build-up of larger gas reservoirs in discs at high redshift, resulting in more SF in bursts. This is shown in the top panel of Fig. 3.1, which compares the predictions of the Fan10b (solid lines) and Fan10a (dashed lines) models for the total SFR density and the SFR density in the quiescent and burst SF modes. Fig. 3.1 shows that the individual SF modes change substantially on using the BR06 SF law. The quiescent SF mode in the Fan10b model is suppressed by almost an order of magnitude above $z \sim 3$ compared to the Fan10a model. This has an impact on the build up of BH mass, by changing the amount of mass brought in through the starburst mode. The enhance-

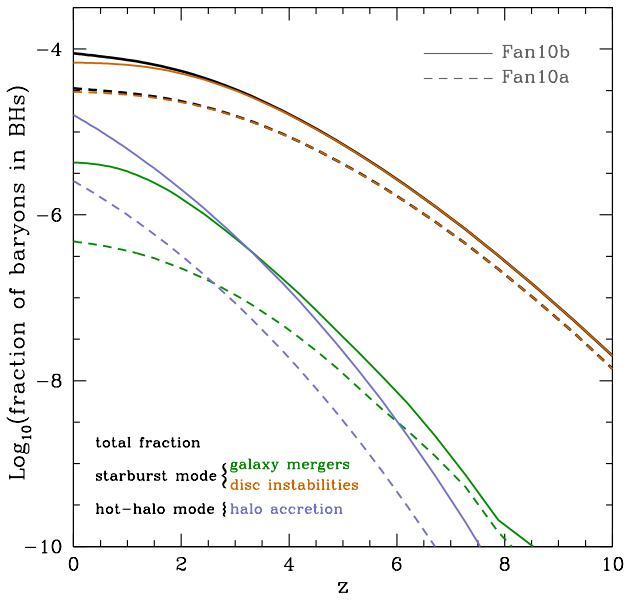

Figure 3.2: The fraction of baryons locked in BHs as a function of redshift (black lines) for the Fan10b (solid lines) and Fan10a (dashed lines) models. The plot also shows the contribution of each accretion channel, namely disc instabilities (orange), galaxy mergers (green) and quasi-hydrostatic halo accretion (blue), to the total fraction of baryons in BHs.

ment of the burst mode is further demonstrated in the bottom panel of Fig. 3.1, where we show the SFR density history in bursts distinguishing between those triggered by disc instabilities and galaxy mergers for the Fan10a and Fan10b models. Both channels show a significant increase in SFR density in the Fan10b model. Since the BHs in our model grow in bursts of SF following disc instabilities and galaxy mergers we expect this enhancement to have a significant impact on the evolution of BH mass.

To evaluate the change in the BH mass when we use the BR06 SF law, we plot in Fig. 3.2 the fraction of baryons locked up in BHs as a function of redshift. In this plot we have also distinguished between the different accretion channels: disc instabilities, galaxy mergers and accretion from hot gas haloes in quasi-hydrostatic equilibrium. We note that in this plot it becomes clear that the growth of BHs is dominated by accretion of cold gas during disc instabilities. Therefore, secular processes in galaxies are responsible

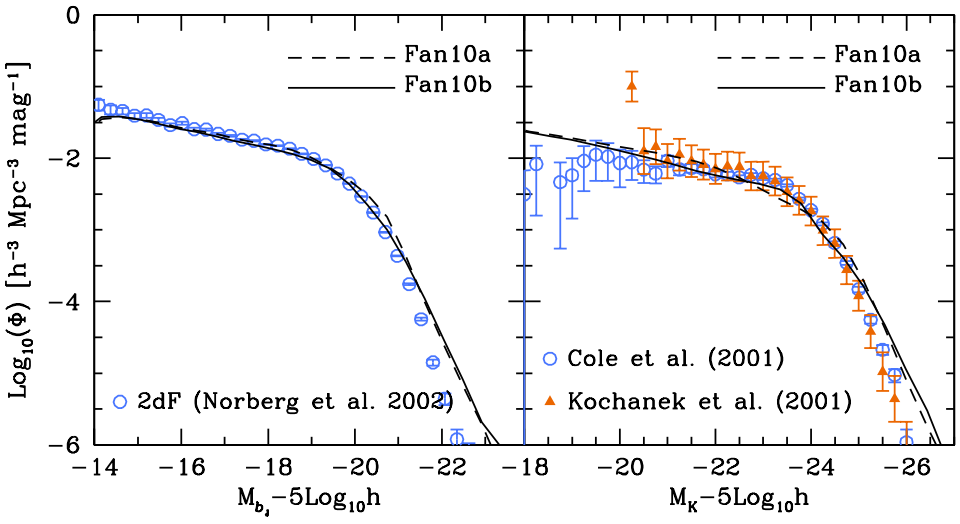

Figure 3.3: The LF of galaxies in the local Universe. The left panel compares the predictions of the Fan10b (solid line) and Fan10a (dashed line) models for the b_J-band LF with the observational determination from the 2dF galaxy redshift survey by Norberg et al. (2002). Similarly, the right panel shows the predictions of the models (line style as before) for the K-band LF and compared to the observational determinations by Cole et al. (2001) and Kochanek et al. (2001). The theoretical predictions from both models include dust extinction.

for building most of the BH mass, while galaxy mergers become an important channel only when they occur between galaxies of similar mass (i.e. major mergers).

The contribution of the starburst mode to the build up of BH mass increases significantly in the Fan10b model compared with the Fan10a model. Both the disc instability and galaxy merger channels are enhanced by a significant factor, resulting in different evolution of the total BH mass. The Fan10b model also predicts different hot-halo mode accretion. This can be attributed to the different values of the $\tilde{\epsilon}_{\rm kin}$ and $f_{\rm Edd}$ parameters used in Fan10a (note that halo accretion is completely independent of SF in the galactic discs). It will become evident in later sections that all of the aforementioned changes induced to the BH mass are essential for providing a good fit to the evolution of the AGN LF.

Finally we note that the total SFR density history in Fig. 3.1 remains unchanged when using the BR06 SF law, as reported by Lagos et al. This implies that properties such as stellar masses and galaxy luminosities are fairly insensitive to the choice of SF law. Indeed, Lagos et al. show that the predictions for the $b_{\rm J}$ and K-band LFs on using the BR06 SF law are very similar to those of the original Bower et al. model and are in reasonable agreement with the observations. Since we have changed the normalization of the SF surface density, we recheck that our model still reproduces the observed LF of local galaxies, as shown in Fig. 3.3. Hence, we are confident that we are a building an AGN model within a realistic galaxy formation model.

3.3 The evolution of BH mass

BH demographics have been the topic of many studies in the past decade mainly because of the tight correlations between the properties of BHs and their host stellar spheroids. These correlations take various forms, relating, for example, the mass of the BH to the mass of the galactic bulge (the $M_{\rm BH} - M_{\rm Bulge}$ relation: Magorrian et al., 1998; McLure and Dunlop, 2002a; Marconi and Hunt, 2003; Häring and Rix, 2004), or to the stellar velocity dispersion (the $M_{\rm BH} - \sigma$ relation: Ferrarese and Merritt, 2000; Gebhardt et al., 2000; Tremaine et al., 2002). These remarkable and unexpected correlations suggest a natural

Table 3.2: Summary of the local BH mass densities, in units of $10^5\,\mathrm{M}_\odot\ \mathrm{Mpc}^{-3}$, found in this and previous studies (assuming $h = 0.7$). Densities are shown for BHs in disc (S,S0) and elliptical (E) galaxies, and for the global BH population in our model (tot).

Study	$\rho_{\rm BH}(\mathrm{S,S0})$	$\rho_{\rm BH}(\mathrm{E})$	$\rho_{\rm BH}(\mathrm{tot})$
This study	0.72	4.70	5.42
Graham and Driver (2007)	$0.95^{+0.49}_{-0.49}$	$3.46^{+1.16}_{-1.16}$	$4.41^{+1.67}_{-1.67}$
Shankar et al. (2004)	$1.1^{+0.5}_{-0.5}$	$3.1^{+0.9}_{-0.8}$	$4.2^{+1.1}_{-1.1}$
Marconi et al. (2004)	1.3	3.3	$4.6^{+1.9}_{-1.4}$
Fukugita and Peebles (2004)	$1.7^{+1.7}_{-0.8}$	$3.4^{+3.4}_{-1.7}$	$5.1^{+3.8}_{-1.9}$

link between the BH evolution and the formation history of galaxies. The manifestation of this link could be associated with AGN activity triggered during the build up of BHs.

The observed $M_{\rm BH} - M_{\rm Bulge}$ relation can be used to estimate the mass of a BH. Several authors have utilised this technique to estimate the MF of BHs in the local Universe (Yu and Tremaine, 2002; Marconi et al., 2004; Shankar et al., 2004), using scaling relations such as $M_{\rm BH} - \sigma_*$ and $M_{\rm BH} - L_{\rm Bulge}$. Based on these MFs, and others inferred by independent studies, the total BH mass density in the local Universe has been estimated to be in the range $\rho_{\rm BH} = (4.2 - 5.1) \times 10^5\,\mathrm{M}_\odot\,\mathrm{Mpc}^{-3}$ (see Table 3.2 for a list of local BH mass density estimates).

The global MF of BHs predicted by the model for all BHs at $z = 0$ is shown in Fig. 4.3a. The predicted MF is almost constant in the mass range $10^6 - 10^8\,\mathrm{M}_\odot$. For higher masses the MF decreases steeply with increasing mass. Our predictions are compared to the local MF estimated by Marconi et al. (2004) and Shankar et al. (2004) using the BH mass scaling relations in local galaxies. The predicted and observed MFs are in good agreement for low mass BHs and disagrees moderately for the $10^9 - 10^{10}\,\mathrm{M}_\odot$ BHs. The overall BH mass density at $z = 0$ predicted by our model amounts to $\rho_{\rm BH} =$

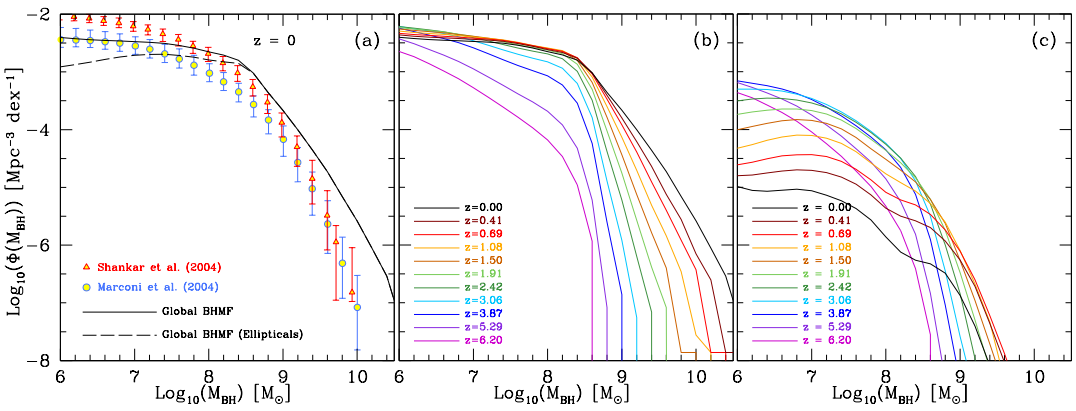

Figure 3.4: a) The global MF of BHs at $z = 0$ predicted by our model (black solid line). The observationally determined MFs are taken from Marconi et al. (2004, red filled triangles) and Shankar et al. (2004, blue filled circles). The error bars correspond to $\pm 1\sigma$ uncertainties. b) The evolution of the global MF of BHs with redshift. c) The MF of actively growing BHs (BH accreting in the thin-disc regime) calculated at different redshifts as indicated in the legend.

$5.42 \times 10^5\,\mathrm{M}_\odot\,\mathrm{Mpc}^{-3}$ and is consistent with that estimated by Marconi et al. ($\rho_{\rm BH} = 4.6^{+1.9}_{-1.4} \times 10^5\,\mathrm{M}_\odot\,\mathrm{Mpc}^{-3}$) and other authors (Shankar et al., 2004; Graham and Driver, 2007; Yu and Lu, 2008, see Table 3.2). Note that, when calculating the BH mass density we do not take into account mass loses due to gravitational wave emission (Menou and Haiman, 2004).

In Fig. 4.3a we also show the contribution to the MF from BHs hosted by elliptical galaxies. We classify as ellipticals all the galaxies whose bulge luminosity contributes more than 60% to their total $b_{\rm J}$-band luminosity (Cole et al., 2000; Parry et al., 2009). The rest of the galaxies are classified as spiral or S0 galaxies. As expected, the BHs in the elliptical galaxies dominate the high mass end of the MF. Hence, the most massive BHs inhabit the centres of the most massive systems in our simulations. By contrast, spiral and S0 galaxies contribute only to the low-mass end of the MF.

The growth of BHs in spiral and elliptical galaxies is driven in principle by different channels. In spiral galaxies, BHs grow mainly via accretion during the starburst mode

whereas the massive BHs in ellipticals grow via accretion during the hot-halo mode or BH-BH mergers. Evidently, the evolution of the MF should be shaped by these growth channels. This is illustrated in Fig. 4.3b, where we show the evolution of the global MF in the redshift range $z = 0 - 6.2$. The build up of the BHs populating the low-mass end takes place at high redshifts and is complete at $z \sim 2$. Since $z \sim 2$ the amplitude of the MF remains almost unchanged indicating that $10^6 - 10^8\,\mathrm{M}_\odot$ BHs in spiral galaxies today were already in place by $z \sim 2$, which follows from the spheroid being older than the disc. The growth of these BHs is dominated by accretion during the starburst mode.

The fact that the space density of this population does not evolve since $z \sim 2$ suggests that the starburst mode becomes less significant in the low-redshift universe. Nonetheless, the build up of the BH mass continues below $z \sim 2$, where we witness the build up of the most massive BHs in the universe. These BHs grow mainly during the hot-halo mode or via mergers with other BHs (see Chapter 2). The different physics governing these channels results in a different slope for the high-mass end of the MF giving rise to a strong break at $\sim 5 \times 10^8\,\mathrm{M}_\odot$. Yet, the build up of these BHs is not very efficient. This becomes clearer when we consider the evolution of the BH mass density. For instance, in the redshift range $z = 6.2 - 1.9$ the BH mass density increases by a factor of ~ 25, as a result of the intense accretion during the starburst mode in the high redshift universe. By contrast, from $z = 1.9$ until $z = 0$ the density only doubles, mainly because the $10^9\,\mathrm{M}_\odot$ BHs become more numerous.

To gain more insight into the rapidly evolving population of accreting BHs we consider the evolution of actively growing BHs, namely those BHs that accrete at relatively high rates (greater that 0.1% of their Eddington accretion rate, see Section 3.4). In Fig. 4.3c we show the MF of actively growing BHs in our model and its evolution with redshift. The most striking characteristic of the MF is the dramatic change in shape and normalization with redshift. At $z = 0$ the MF has a maximum at $\sim 10^7\,\mathrm{M}_\odot$ below which the accreting BHs have an almost constant space density (see also results from SDSS, Heckman et al., 2004). A significant bend in the slope located at $\sim 10^8\,\mathrm{M}_\odot$ is seen, a feature that remains evident up to $z \sim 2 - 3$. At higher redshifts, the space density of BHs drops substantially, establishing that accreting BHs with masses $\gtrsim 10^9\,\mathrm{M}_\odot$ are very rare objects.

These BHs are accreting at relatively low rates and therefore power faint-AGN activity (see discussion in Section 3.4.4).

As illustrated by Fig. 4.3c, the low-mass end of the MF evolves differently with redshift compared to the high-mass end. Its amplitude increases significantly with increasing redshift, suggesting that the space density of low-mass accreting BHs was higher at earlier epochs. This evolution is consistent up to $z \sim 2.5$ above which the amplitude of the low-mass end starts to decline modestly. The high-mass end shows a similar increase towards higher amplitudes with increasing redshift, however, the decline appears earlier, almost at $z \sim 1$. This is because the high-mass end forms much later than the low-mass end in our model.

The change of the MF of BHs with redshift illustrated in Fig. 4.3c indicates an evolutionary scenario for the actively growing BH population in our model which mirrors the hierarchical growth of their host galaxies. At high redshifts the accretion activity is dominated by $10^6\,\mathrm{M}_\odot$ BHs. Accretion onto these BHs results in the fast build up of the $10^7 - 10^8\,\mathrm{M}_\odot$ BHs at $z \sim 4 - 6$, as implied by the increase in the space density of these BHs in Fig. 4.3c. From $z \sim 4$ the accretion activity, gradually shifts to the $10^7 - 10^8\,\mathrm{M}_\odot$ BH population. This is mainly because more higher mass galactic systems are now in place and thus disc instabilities and galaxy mergers contribute to the growth of higher mass BHs compared to earlier epochs. Accretion onto these BHs leads to the fast build up of the $> 10^8\,\mathrm{M}_\odot$ BH population, which will later be promoted via accretion during the hot-halo mode and BH-BH mergers to the most massive BHs in our model.

Eventually, the different physical processes that drive the evolution of BH mass result in a tight correlation between the BH and host galaxy mass, as shown in Fig. 3.5a. In this figure, we plot the median of the $\log M_{\rm BH} - \log M_{\rm Bulge}$ distribution (solid lines) and the associated $10 - 90$ percentiles (dotted lines) at $z = 0, 1.08, 2.42$ and 6.2. Surprisingly, a well defined $M_{\rm BH} - M_{\rm Bulge}$ relation is established already at $z = 6.2$, merely as a consequence correlation of the accretion process with the SF that shapes the mass of the host bulges. Even when the growth of BHs is dominated by other processes, which are only indirectly linked to the SF, the tight correlation remains. For example, the most massive BHs correlate with the mass of their host bulge because feedback energy when

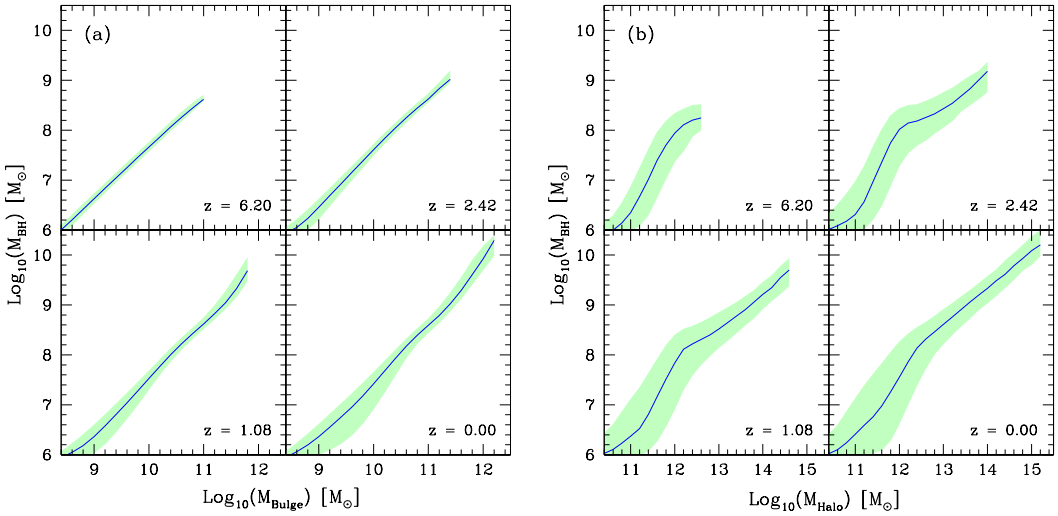

Figure 3.5: The median of the $M_{\rm Bulge}-M_{\rm BH}$ (a) and $M_{\rm Halo}-M_{\rm BH}$ (b) distributions predicted by our model (solid lines). Predictions are shown for $z = 0, 1.08, 2.42$ and 6.20 as indicated by the legend. The dotted lines indicate the $10-90$ percentile ranges of the distributions.

gas is accreted onto them regulates the cooling flows that supply gas for SF and therefore the change of mass of the bulge.

In a hierarchical universe the most massive galactic bulges are usually found in the most massive DM haloes. Since the galaxies with the most massive bulges (namely the passive ellipticals) host the most massive BHs and those with less massive bulges (namely the spiral and S0 galaxies) host the low-mass BHs, it is natural to assume that there must be a similar hierarchy in the halo environments where these BHs can be found. Indeed, when plotting the relation between the BH mass and the mass of the host halo we find a tight correlation. This is illustrated in Fig. 3.5b where we show the median of the $\log M_{\rm Halo} - \log M_{\rm BH}$ distribution (solid lines) and its $10-90$ percentiles (dotted lines) for different redshifts. Remarkably, the physical processes that shape the $M_{\rm Bulge} - M_{\rm BH}$ relation in our model give rise to a well defined link between these two quantities at all redshifts. The $M_{\rm Halo}-M_{\rm BH}$ relation can be parametrized by a power law with a very steep slope that becomes shallower above $M_{\rm Halo} \simeq 10^{12} - 10^{13}\,{\rm M}_{\odot}$.

The different slopes indicate the different efficiency with which BHs grow in haloes

of different mass. Low mass haloes are very efficient in growing BHs since in these environments the gas cooling is not suppressed. As a consequence, BHs double their mass remarkably quickly resulting in a steep slope for the $\log M_{\rm Halo} - \log M_{\rm BH}$ relation. The fast BH mass build up slows down when hot gas in the host haloes enters the quasi-hydrostatic regime. In this case, AGN feedback suppresses the cooling flows that provide fresh cold gas to the galaxies and thus accretion during the starburst mode is reduced. In the quasi-hydrostatic regime gas accretion during the hot-halo mode and mergers dominate the BH mass build up. The hot-halo mode is, however, characterized by low accretion rates (see Section 3.4.3). BH mergers rather than adding new baryons to the BHs, only redistribute the BH mass. Therefore, the BH mass build up slows down establishing haloes of $M_{\rm Halo} \sim 10^{13} - 10^{15}\,{\rm M}_{\odot}$ as environments where BH growth is not very efficient.

Given the efficiencies that characterize the two different regimes in Fig. 3.5b we expect to find the brightest AGN in the $10^{11} - 10^{13}\,{\rm M}_{\odot}$ haloes. This perhaps is in contrast with the common expectation that the brightest quasars should be found in the most massive haloes.

3.4 BH spins, accretion efficiencies and disc luminosities

AGN are unambiguously the most powerful astrophysical sources in the Universe. The ability of an accretion disc to produce electromagnetic radiation is attributed to gravity yet its radiative efficiency is controlled primarily by the properties of the gas. When the gas settles itself into a thin, cool, optically-thick accretion disc (Shakura and Sunyaev, 1973), the efficiency of converting matter into radiation can reach 32% (Novikov & Thorne 1973). When the flow is characterized by very high, Eddington accretion rates, such extremely luminous discs can power $10^{47} - 10^{48}\,{\rm erg\,s^{-1}}$ quasars. In the next sections we describe how we model the physics of accretion flows and present predictions for the most fundamental properties characterising the accreting BH systems in our model.

3.4.1 Calculation of the disc luminosity

The first important property that we can calculate in our model is the physical accretion rate, $\dot{M}$, onto a BH. This is defined as

$$\dot{M} = \frac{M_{\rm acc}}{t_{\rm acc}}, \tag{3.1}$$

where $M_{\rm acc}$ is the total accreted mass and $t_{\rm acc}$ is the accretion timescale. The accretion timescale is assumed to be directly linked to the dynamical timescale of the host bulge, $t_{\rm Bulge}$, through the relation

$$t_{\rm acc} = f_{\rm q} t_{\rm Bulge}. \tag{3.2}$$

$f_{\rm q}$ is a free parameter and its value is fixed to 10. This is determined by fitting the predictions of our model for the quasar LF to the observations (see Section 3.5.2).

The accretion rate has a dramatic impact on the geometry and radiative properties of the accretion disc (see Done et al., 2007). We have studied the effect of the accretion rate on the disc properties in Chapter 2. Here we summarise again the main characteristics of the two accretion regimes in our model and describe changes which we introduce to improve their modelling.

The two distinct accretion modes considered in this model are separated at a rate of 1% of $\dot{M}_{\rm Edd}$. In the first state, for $\dot{m} \geqslant 0.01$, we assume that the gas forms an accretion disc whose physics is adequately described by the radiatively efficient thin-disc model of Shakura and Sunyaev (1973). The bolometric luminosity of a thin disc, $L_{\rm bol}$, is linked to $\dot{M}$ through the standard expression

$$L_{\rm bol} = \epsilon \dot{M} c^2. \tag{3.3}$$

When the accretion becomes substantially super-Eddington ($L_{\rm bol} \geqslant \eta L_{\rm Edd}$), the bolometric luminosity is limited to $\eta[1 + \ln(\dot{m}/\eta)]L_{\rm Edd}$ (Shakura and Sunyaev, 1973), where η is an ad hoc parameter equal to 2 that allows a better modelling of bright end of the LF (see Section 3.5). However, we do not restrict the accretion rate if the flow becomes super-Eddington.

The second accretion state, with $\dot{m} < 0.01$, is associated with sub-Eddington accretion flows with very low density. For such low accretion rates, the gas flow is unable to

cool efficiently since radiative cooling does not balance the energy generated by viscosity. Thus, the viscous energy is trapped in the gas as entropy and ultimately advected into the hole. This type of accretion is known as an advection dominated accretion flow (ADAF, Rees, 1982; Narayan and Yi, 1994; Abramowicz et al., 1995). ADAFs have a number of distinct properties, some of which will be essential for the analysis in later sections. For example, for an ADAF around a BH, only a fraction of the standard accretion luminosity, $L = \epsilon \dot{M} c^2$, is emitted as radiation. The remainder of the viscously dissipated energy is stored in the gas as entropy, resulting in hot flows with almost virial temperatures. We note that, as shown by Ichimaru (1977), the ions and the electrons in an ADAF are not thermally coupled and, thus, reach different temperatures. This two-temperature virialized plasma flow is optically thin and, for high viscosity parameters ($\alpha \sim 0.1 - 0.3$), it acquires a quasi-spherical geometry around the BH, which resembles spherical Bondi accretion. However, the accretion is entirely due to dissipation via viscous forces rather than gravity. The bolometric luminosity of the flow in this case is equal to the luminosity emitted by the various cooling processes. For $\dot{m} \lesssim 10^{-3}\alpha^2$ it is only due to Comptonisation, whereas for $\dot{m} \gtrsim 10^{-3}\alpha^2$ the cooling is split between Compton and synchrotron emission.

As the accretion rate increases, the emission of the energy produced by the viscous processes in the gas becomes more efficient. Above some critical accretion rate, $\dot{m}_c$, the radiative efficiency of the gas is so high that the flow cools down to a thin disc. The critical accretion is independent of the BH mass but depends strongly on the viscosity, $\dot{m}_c \simeq 1.3\alpha^2$. Taking $\dot{m}_c = 0.01$ implicitly fixes the value of α to be 0.087 for all the ADAFs in our model. The luminosity of the flow for the two different regimes is then given by Mahadevan (1997),

$$L_{\rm bol,ADAF} = \begin{cases} \epsilon \dot{M} c^2 \left[0.4 \dot{m} \beta / \alpha^2 \right], & \dot{m} > 7.5 \times 10^{-6} \\ \epsilon \dot{M} c^2 \left[4 \times 10^{-4} (1-\beta) \right], & \dot{m} \lesssim 7.5 \times 10^{-6} \end{cases} \tag{3.4}$$

where β is related to the Shakura-Sunyaev viscosity parameter α through the relation $\alpha \approx 0.55(1-\beta)$ (Hawley and Krolik, 2006). The expressions in the square brackets in Eq. 3.4 shows how much less efficient the cooling is in an ADAF compared to the standard efficiency ϵ of a thin disc. For example, at $\dot{m} = 0.01$ an ADAF is characterized

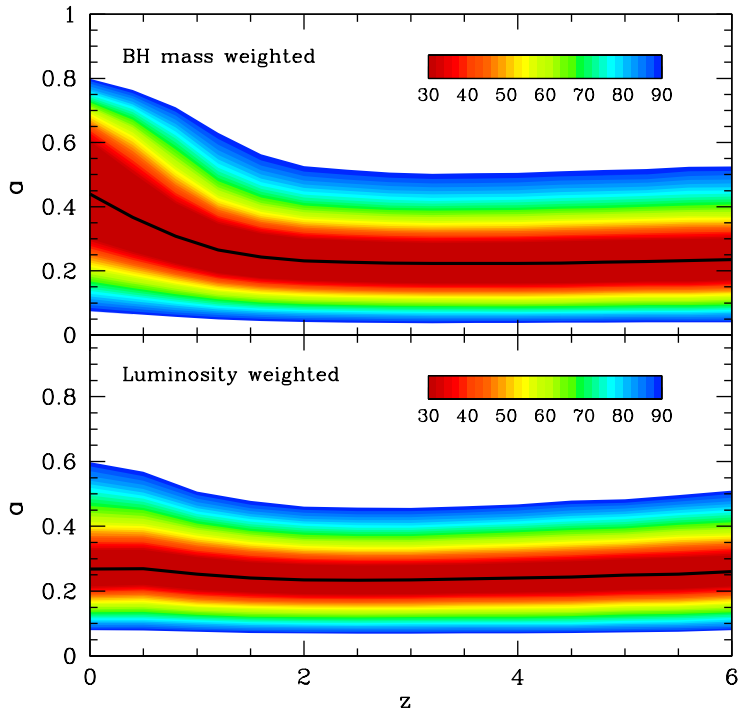

Figure 3.6: Top: The median BH spin weighted by BH mass as a function of redshift for BHs in our model (solid black line). Bottom: The median BH spin weighted by disc luminosity for all AGN accreting in the thin-disc regime (solid black line). The values of the different percentiles (shaded regions) are indicated in both cases by the colour bars.

by an accretion efficiency of 0.44ϵ, less than approximately half as luminous as a thin disc.

3.4.2 BH spins and accretion efficiencies

In Chapter 2 we describe in detail how we model the evolution of BH spin. In brief, the spins of BHs change during gas accretion (whenever a starburst is triggered by disc instabilities or galaxy mergers in the starburst mode or during the cooling of gas from the hydrostatic halo in the hot-halo mode) and mergers with other BHs. Fig. 3.6 shows the evolution with redshift of the median of the BH spin distribution at a given redshift for two different cases. Firstly, we show the median spin weighted by BH mass (upper

panel) for all the BHs with $M_{\rm BH} > 10^6\,{\rm M}_\odot$. The median shows an approximately constant trend from $z = 6$ to $z = 2$ and has a well defined value of ~ 0.25. In this redshift range BHs grow predominantly during disc instabilities (see Fig. 3.2) and therefore the evolution of BH spin is governed by accretion. As shown in Chapter 2, accretion of gas results in low spins with a typical value of $a \sim 0.2$ (under the assumption that the gas is fed chaotically onto the BH). Hence, as indicated also by the different percentiles in the plot (shaded regions), the bulk of BHs acquire low spins.

Below $z = 2$ BH mergers start to become an important channel for growing the BH mass, especially when they are between BHs of similar mass, as expected following a major galaxy merger. However, this is a characteristic only of the most massive BHs in our model ($M_{\rm BH} > 10^9\,{\rm M}_\odot$). Mergers between those BHs tend to increase the spin of the final remnant to values $a > 0.7$ (see also Baker et al., 2007; Berti and Volonteri, 2008; Fanidakis et al., 2010). Eventually, at low redshifts BH mergers give rise to a population of rapidly rotating BHs. The appearance of these BHs, as indicated also by the different percentiles below $z = 2$, increases the dynamical range of the predicted spins up to values of 0.998 (the range of spin values in the distribution of BHs in Fig. 3.6 is smaller because we show only up to the $90^{\rm th}$ percentile of the data). The environmental dependence of BH spins is illustrated in Fig. 3.7, where we see that the most rapidly-rotating BHs populate the centres of the most massive DM haloes. In contrast, slowly rotating BHs are found in low mass halo environments. This is a consequence of the correlation between BH mass and spin in our model: rapidly rotating BHs have masses $\gtrsim 10^9\,{\rm M}_\odot$. These BHs are hosted by massive elliptical galaxies in our model which inhabit the centres of the most massive haloes (see Chapter 2).

In contrast, the median spin of actively growing BHs in our model does not reveal the presence of rapidly spinning BHs. This is demonstrated in the lower panel of Fig. 3.6 where we have selected the actively growing BHs in our sample ($\dot{m} > 0.01$) and plot the median of their spin distribution weighted by disc luminosity. As illustrated in the plot, the predictions are consistent with low spins at all redshifts even at $z \sim 0$. This is because in this sample we have selected only the actively growing BHs; we find that almost exclusively these are $\lesssim 10^9\,{\rm M}_\odot$ BH and thus have low spins. Hence, these BHs

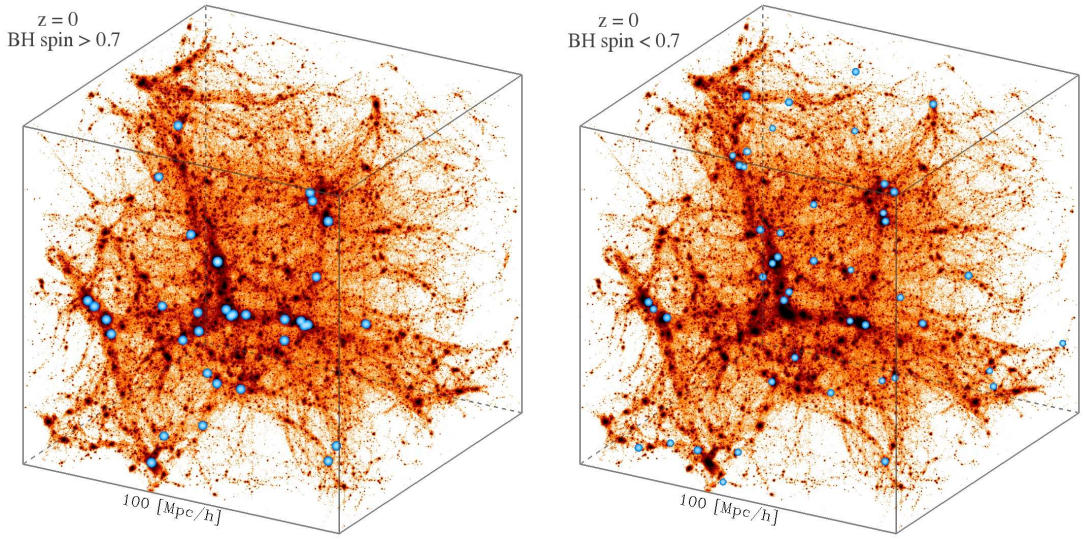

Figure 3.7: The distribution of rotating BHs at $z = 0$ in the Millennium simulation. The two panels show the same DM distribution in a cube of comoving length $100\ h^{-1}\,\mathrm{Mp}$ colour coded according to density (black represents the peaks of DM density). Over plotted with blue spheres in the left plot are galaxies with rapidly rotating BHs ($a > 0.7$) predicted by the semi-analytic model. Similarly, in the right plot are shown a sample of galaxies with slowly rotating BHs ($a < 0.7$) randomly chosen from our data and equal in number to the $a > 0.7$ BHs. The size of the spheres is proportional to the spin of the BH that the galaxy hosts.

dominate the sample and determine the over all trend of the median.

The $a - M_{\rm BH}$ correlation can be further elucidated through the dependence of the accretion efficiency on the mass of actively growing BHs. This is illustrated in Fig. 3.8 where we show the median of the ϵ distribution for the sample of actively growing BHs (solid lines), again weighted by the disc luminosity. At $z = 0$, the median is approximately constant for $M_{\rm BH} \lesssim 10^8$, with a typical value of ~ 0.07. As implied by the $10-90$ percentiles (dotted lines), the dynamical range of the typical ϵ values is very small and restricted to the range $0.06-0.08$ ($a = 0.1-0.5$). For higher BH masses the efficiency can reach significantly higher values. This is a manifestation of the fact that high mass BHs have high spins and thus high accretion efficiencies when they accrete in the thin-disc regime. Fig. 3.8 also demonstrates that the dependence of the efficiency on the BH mass does not change with redshift. Hence, at all redshifts BHs have very well determined accretion efficiencies. It is therefore, only the accretion rate that regulates the luminosity output from an accreting BH.

Note that, BHs with higher efficiencies ($\epsilon \gtrsim 0.15$) are still found in our BH populations. However, they are usually very massive ($M_{\rm BH} > 5 \times 10^8\,{\rm M}_\odot$) and do not undergo significant quasar activity. These BHs can support the formation of very strong jets in the presence of an ADAF and establish the host galaxy as a radio-loud AGN (high spins and BH mass are essential for high jet luminosities; Fanidakis et al., 2010). In this case, a plot similar to the one in the top panel of Fig. 3.6, weighted by jet instead of disc luminosity, will unveil a significant population of AGN with rapidly rotating BHs. Hence, BH spins (and efficiencies) can display different distributions depending on the AGN population we are probing.

3.4.3 The distribution of the $\lambda_{\rm Edd}$ parameter

Having explored the evolution of the BH mass and spin, and calculated the accretion efficiencies for the BHs accreting in the thin-disc regime, we now investigate the disc luminosities of the accreting BHs predicted by the model. We calculate the bolometric disc luminosity in the ADAF and thin-disc regime using the formulation described in Section 3.4.1. It is useful to scale $L_{\rm bol}$, in units of $L_{\rm Edd}$ in order to remove the dependence of

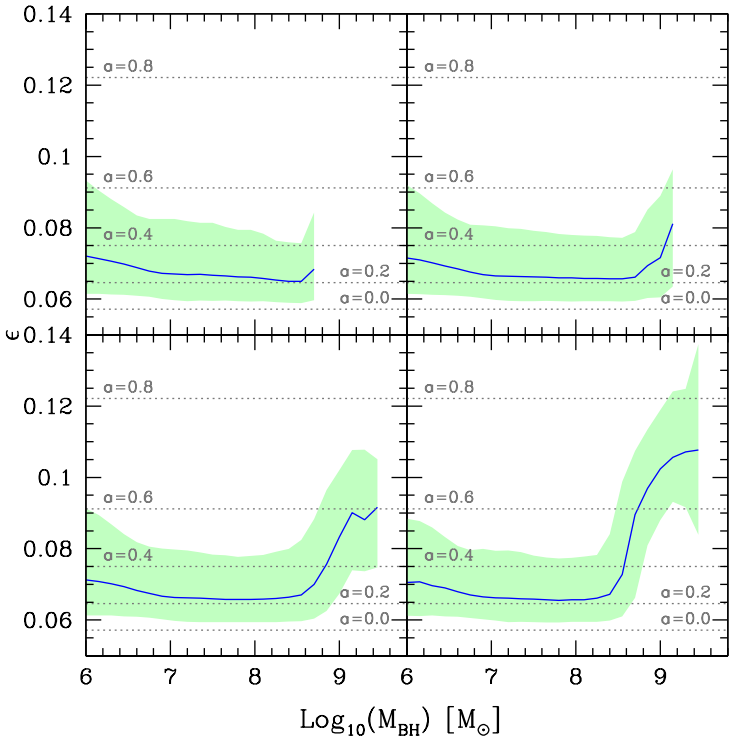

Figure 3.8: The median of the accretion efficiency, ϵ, as a function of BH mass at different redshifts (solid lines) for BHs that accrete in the thin disc regime. Also shown are the $10-90$ percentiles of the $\epsilon - M_{\rm BH}$ distribution. We also indicate the values of ϵ that correspond to spin values of $0, 0.2, 0.4, 0.6$ and 0.8 (dotted grey lines). The model predicts that low mass BHs have well defined low accretion efficiencies ($\epsilon \simeq 0.06 - 0.08$) at all redshifts. In contrast, in the low redshift universe, a population of very massive BHs with high radiative accretion efficiencies ($\epsilon \gtrsim 0.08$) emerges.

the luminosity on the BH mass. For this purpose we introduce the Eddington parameter, $\lambda_{\rm Edd}$, defined as,

$$\lambda_{\rm Edd} = L_{\rm bol}/L_{\rm Edd} = \begin{cases} \gamma\dot{m}^2, & \text{if } \dot{m} < 0.01 \\ \dot{m}, & \text{if } \dot{m} \geqslant 0.01 \\ \eta[1+\ln(\dot{m}/\eta)], & \text{if } L_{\rm bol} \geqslant \eta L_{\rm Edd} \end{cases} \tag{3.5}$$

where $\gamma = 0.4\beta/\alpha^2$.

In Fig. 3.9 we plot the distribution function of $\lambda_{\rm Edd}$ at different redshifts for all accreting sources with $M_{\rm BH} > 10^6\,{\rm M}_\odot$. The plane of the plot is divided into two distinct regions: the thin-disc regime and the ADAF regime (note the discontinuity due to the different dependence of $\lambda_{\rm Edd}$ on $\dot{m}$ in the ADAF and thin disc regime). This distinction is essential since it will help us to readily unravel the space density and evolution of luminous and under-luminous AGN in our model.

The first important property that is unambiguously depicted by Fig. 3.9 is the bimodal nature of the $\lambda_{\rm Edd}$ distribution. The bimodality is exhibited nearly at all redshifts. The first peak falls in the ADAF regime and it shifts from $\log\lambda_{\rm Edd} \simeq -2.5$ at $z \sim 6$ to $\log\lambda_{\rm Edd} \simeq -4$ at $z \sim 0$. The objects that contribute to that mode are all the AGN accreting during the hot-halo mode and those AGN accreting during the starburst mode with $\log\dot{m} < -2$. The second peak is located in the thin-disc regime and in this mode we find the most luminous objects in our model. Their peak space density shifts from $\log\lambda_{\rm Edd} \simeq -0.5$ at $z \sim 6$ to $\log\lambda_{\rm Edd} \simeq -1$ at $z \sim 0$, where it nearly disappears. The objects populating the second mode are AGN accreting exclusively in the starburst mode. Since the thin-disc regime is radiatively efficient these objects are expected to dominate the LF of AGN in all bands (except the radio and perhaps the hard X-rays).

The relative space density of the objects in each mode changes dramatically with redshift. At high redshifts, AGN in the thin-disc regime are much more numerous than those in the ADAF regime. The BHs in these AGN have low masses, accrete near the Eddington limit and double their mass several times within a few Gyrs. In contrast, BHs in the ADAF regime are more than an order of magnitude less numerous. Their number density is dominated by BHs that have reached by that time a high mass ($10^8 - 10^9\,{\rm M}_\odot$) and their host galaxy undergoes a disc instability or minor merger event that provides

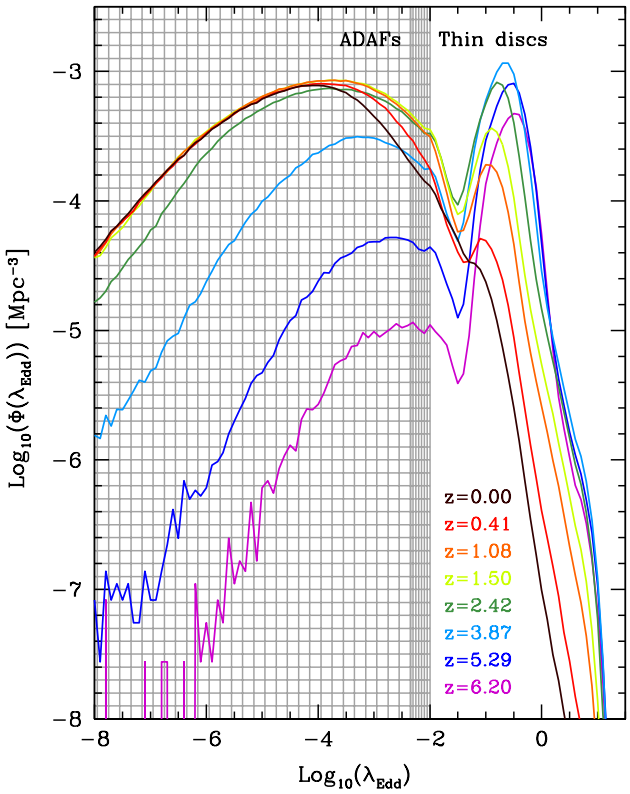

Figure 3.9: The distribution of $\lambda_{\rm Edd} = L_{\rm bol}/L_{\rm Edd}$ for different redshifts as indicated by the colour bar. The plane is divided into the radiative-inefficient regime of ADAFs (shaded region) and radiative-efficient regime of thin discs. The denser shading denotes the region of the plane where the discontinues transition from the ADAF to the thin-disc regime takes place.

gas with a low accretion rate. The first BHs accreting during the hot-halo mode also contribute to the objects populating the ADAF regime.

This picture changes in the low redshift universe. As redshift decreases more haloes enter the quasi-hydrostatic cooling regime and thus more BHs start to accrete in the ADAF regime (see also the evolution of the hot-halo accretion channel in Fig. 3.2). In this mode we also find AGN powered by gas accretion during gas-poor disc instabilities and galaxy mergers. Eventually, at $z = 0$ BHs accreting via an ADAF are much more common than those accreting via a thin disc.

3.4.4 The $L_{\rm bol} - M_{\rm BH}$ correlation

When examining the distribution function of $\lambda_{\rm Edd}$ in Fig. 3.9 we find a small population of super-Eddington AGN present at all redshifts. The number density of these AGN drops sharply with increasing $\lambda_{\rm Edd}$ due to the logarithmic dependence on the accretion rate. Whether these objects represent the most luminous AGN at some given redshift is not obvious since $\lambda_{\rm Edd}$ is independent of the BH mass. To unravel the relation between the BH mass and accreted luminosity we plot in Fig. 3.10 the median of the $L_{\rm bol} - M_{\rm BH}$ distribution and its associated percentiles at $z = 0.5, 1$ and 2. We show predictions both for objects accreting in the thin-disc (lower panels) and ADAF (upper panels) regime. To guide the reader we also distinguish with different shading the region where $L_{\rm bol} \geqslant L_{\rm Edd}(M_{\rm BH})$.

When we consider BHs accreting in the ADAF regime we find that the $L_{\rm bol} - M_{\rm BH}$ correlation is characterized by a floor at luminosities $\lesssim 10^{42}\,{\rm erg\,s^{-1}}$. In this regime, BHs have $\lambda_{\rm Edd} \simeq 10^{-4}$ and therefore they comprise the majority of accreting BHs in our sample (remember the location of the peak of the $\lambda_{\rm Edd}$ distribution function in Fig. 3.9). For example, at $z = 0$ we find that $\sim 93\%$ of the BHs produce luminosities fainter than $10^{42}\,{\rm erg\,s^{-1}}$. For brighter luminosities, we find a strong correlation between $M_{\rm BH}$ and $L_{\rm bol}$ which indicates that the most massive BHs must have higher accretion rates compared to the lower mass ones. Indeed, when identifying the accretion properties of the most massive BHs we find that the $\gtrsim 10^8\,{\rm M_\odot}$ BHs have $\lambda_{\rm Edd} \gtrsim 10^{-3}$. Thus, these BHs are able to produce a significant luminosity even though they accrete in the ADAF regime.

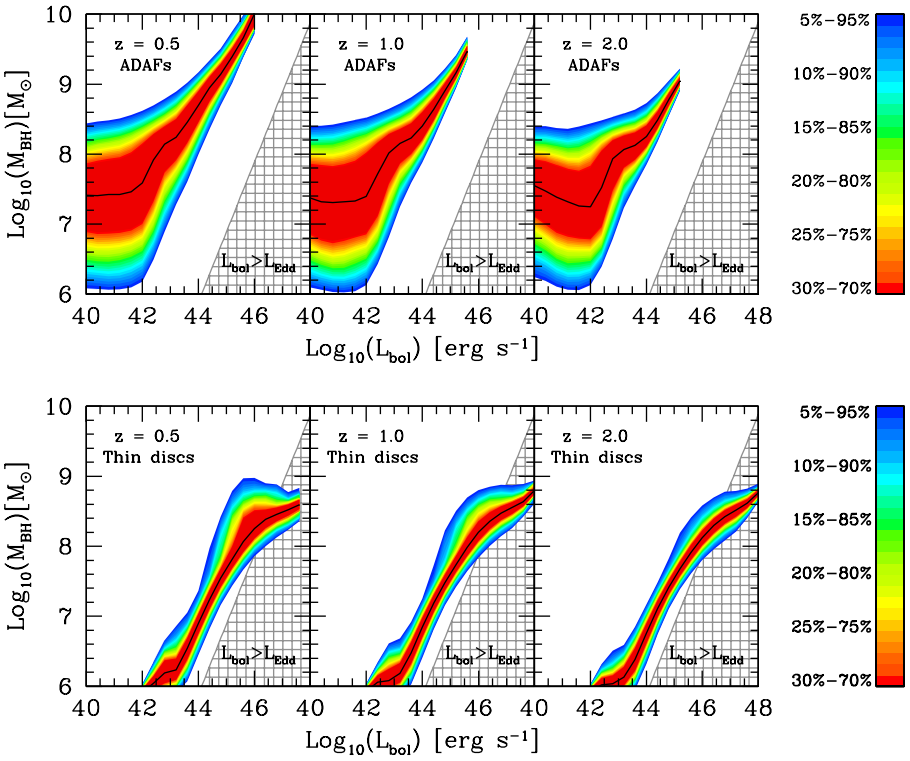

Figure 3.10: The median of the $M_{\rm BH} - L_{\rm bol}$ distribution at $z = 0.5, 1$ and 2 (black solid lines) for BHs accreting via a thin disc (lower panels) and ADAF (upper panels). The different percentiles of the distribution are colour-coded according to the bar on the right. The shaded regions represent the regime where the accretion becomes super-Eddington.

In fact, in our sample we find $\sim 10^{10}\,\mathrm{M}_{\odot}$ BHs accreting at $\dot{m} \simeq 0.01$ which produce luminosities as high as $10^{46}\,\mathrm{erg\,s^{-1}}$. However, these BHs are very rare: at $z = 0.5$, where the space density of these BHs peaks, we find only a handful of them (space densities lower than $10^{-8}\ \mathrm{Mpc^{-3}}$). For higher redshifts, their space density declines and as a consequence the maximum disc luminosity produced in the ADAF regime is also reduced.

In the thin-disc regime, we find that accreting BHs typically produce luminosities greater than $10^{42}\,\mathrm{erg\,s^{-1}}$. The $\log L_{\rm bol} - \log M_{\rm BH}$ correlation in this regime increases monotonically until the slope becomes significantly shallower near the highest luminosities achieved at a given redshift. The nature of the break in the slope is determined by the AGN feedback prescription in our model. When massive haloes reach quasi-hydrostatic equilibrium they become subject to AGN feedback that suppresses the cooling flows; some of the mass which would have been involved in the cooling flow is instead accreted onto the BH. In these haloes we find the most massive BHs in our model ($\gtrsim 10^{9}\,\mathrm{M}_{\odot}$, see Fig 3.5b). Therefore, these BHs are expected to live in gas poor environments and when they accrete gas they usually do so via an ADAF disc. In this regime, the suppression of cooling flows forces the $L_{\rm bol} - M_{\rm BH}$ correlation to evolve only along the $L_{\rm bol}$ axis since accretion via a thin disc onto $\gtrsim 10^{9}\,\mathrm{M}_{\odot}$ BHs becomes very rare.

The correlation between $L_{\rm bol}$ and $M_{\rm BH}$ found at $z = 0.5$ remains approximately the same at higher redshifts. Only the ranges of BH mass corresponding to the bulk of the AGN shift modestly to lower mass. This is due to the fact that in a hierarchical universe accretion shifts to lower BH masses at higher redshifts (Section 3.3). In addition, the break in the slope at high luminosities becomes less prominent since fewer haloes are in quasi-hydrostatic equilibrium at high redshifts.

The most luminous AGN ($\gtrsim 10^{46}\,\mathrm{erg\,s^{-1}}$) are exclusively powered by super-Eddington accretion onto $\sim 10^{8} - 10^{9}\,\mathrm{M}_{\odot}$ BHs. This implies that the most luminous quasars are expected to be found in $\sim 10^{12} - 10^{13}\,\mathrm{M}_{\odot}$ DM haloes and not in the most massive ones (remember the $M_{\rm Halo} - M_{\rm BH}$ in Fig. 3.5b). This is in good agreement with the typical DM halo mass quasars are inferred to inhabit as suggested by several observational clustering analyses (da Ângela et al., 2008; Shen et al., 2009; Ross et al., 2009). In contrast, accretion characterized by lower luminosities spans the whole range of BH masses

$(10^6 - 10^{10}\,\mathrm{M}_\odot)$.

3.5 The evolution of the AGN luminosity functions

3.5.1 Bolometric corrections and obscuration

The LF is calculated in redshift ranges which are determined by the observations we are comparing with. The contribution of each AGN to the LF in a range $z = z_1 - z_2$ is weighted by a factor,

$$w_{\rm BH} = t_{\rm active}/\Delta t_{z_1,z_2}, \tag{3.6}$$

where $\Delta t_{z_1,z_2}$ is the time interval delineated by the redshift range $z_1 - z_2$ and $t_{\rm active}$ is the time during which the AGN is "on" in the $\Delta t_{z_1,z_2}$ interval (in principle $t_{\rm active} = t_{\rm acc}$ only if the whole period of accretion falls within $z_1 - z_2$). The bands for which we present predictions are the B-band (4400Å), soft X-ray (SX: $0.5 - 2$ keV) and hard X-ray (HX: $2 - 10$ keV). The bolometric corrections considered here are approximated by the following $3^{\rm rd}$ degree polynomial relations (Marconi et al., 2004),

$$\begin{aligned}
\log(L_{\rm HX}/L_{\rm bol}) &= -1.65 - 0.22\mathcal{L} - 0.012\mathcal{L}^2 + 0.0015\mathcal{L}^3 \\
\log(L_{\rm SX}/L_{\rm bol}) &= -1.54 - 0.24\mathcal{L} - 0.012\mathcal{L}^2 + 0.0015\mathcal{L}^3 \\
\log(\nu_{\rm B} L_{\nu_{\rm B}}/L_{\rm bol}) &= -0.80 + 0.067\mathcal{L} - 0.017\mathcal{L}^2 + 0.0023\mathcal{L}^3
\end{aligned} \tag{3.7}$$

where $\mathcal{L} = \log(L_{\rm bol}/L_\odot) - 12$. Marconi et al. derive these correction based on a spectral template where the spectrum at $\lambda > 1\mu m$ is truncated in order to remove the IR bump. In this way, the spectrum corresponds to the intrinsic luminosity of the AGN (optical, UV and X-ray emission from the disc and hot corona). We apply Eqs. 3.7 to both thin discs and ADAFs, though we note that there is evidence for a change in these corrections with $\lambda_{\rm Edd}$ (Vasudevan and Fabian, 2007).

There is evidence that the fraction of obscured AGN decreases with increasing X-ray luminosity (Ueda et al., 2003; Steffen et al., 2003; Hasinger, 2004; La Franca et al., 2005) a trend found also by Simpson (2005) in a sample of broad and narrow-line AGN from the SDSS. The question of whether the fraction of obscured AGN depends also on redshift is more uncertain. If gas or dust in galaxies provide the obscuring medium then

its abundance should evolve in a fashion similar to the SFR history. This will result in a fraction of obscured AGN that is redshift dependent. In addition, a strongly evolving population of obscured AGN is required by AGN population synthesis models to reproduce the properties of the X-ray background (Comastri et al., 1995; Gilli et al., 1999; Ballantyne et al., 2006a,b; Gilli et al., 2007). Ueda et al. (2003) and Steffen et al. (2003) suggest that such a trend is not clear in AGN samples of deep X-ray surveys. However, the analysis by Treister and Urry (2006) on AGN samples of higher optical spectroscopic completeness indicates that the relative fraction of obscured AGN does increase with redshift.

More recently, Hasinger (2008) showed, based on a sample of X-ray selected AGN from ten independent samples with high redshift completeness, that the fraction of obscured AGN increases strongly with decreasing luminosity and increasing redshift. According to Hasinger, the dependence of the obscured fraction of AGN, $f_{\rm obsc}$, on $L_{\rm HX}$, can be approximated by a relation of the form,

$$f_{\rm obsc} = -0.281 \log(L_{\rm HX}) + A(z), \tag{3.8}$$

where $A(z) = 0.308(1+z)^{0.48}$ and $L_{\rm HX} = 10^{42} - 10^{46}\,{\rm erg\,s^{-1}}$. A broken power law can also be used to describe $A(z)$ which provides a fit with modestly better statistical significance. The best fit gives a power law of the form $A(z) \propto (1+z)^{0.62}$ that saturates at $z = 2.06$ and remains constant thereafter.

Hence, in order to determine the correct population of AGN in a luminosity bin of a given band we need to take into account the effects of obscuration. To do so, we utilise the dependence of the obscured fraction on the $L_{\rm HX}$ luminosity found in Hasinger (2008) as follows. We calculate the fraction of visible AGN, $f_{\rm vis} = 1 - f_{\rm obsc}$, at a given luminosity bin in the $2-10$ keV band using Eq. 3.8 and then we associate the value of $f_{\rm vis}$ with the corresponding B-band or soft X-ray luminosity bin using Eqs. 3.7. The LF can then be expressed as,

$$\left.\frac{d\Phi}{d\log(L_X)}\right|_{\rm vis} = f_{\rm vis}(L_{\rm HX}, z)\frac{d\Phi}{d\log(L_X)}. \tag{3.9}$$

In our analysis, we choose the single instead of the broken power law form of $A(z)$ to allow for a comparison with previous work (e.g., La Franca et al., 2005). In this way we

provide a simple, yet well constrained, prescription for the effects of obscuration in the AGN of our model.

3.5.2 The optical LF

In Fig. 3.11 we present the $b_{\rm J}$-band LF of quasars in 9 different redshift bins between $0.4 < z < 4.25$. Our predictions are shown before and after applying the obscuration effect (dashed and solid black lines respectively). Absolute magnitudes are first calculated in the B band using the standard expression

$$M_{\rm B} = -10.44 - 2.5\log(L_{\rm B}/10^{40}{\rm erg\ s^{-1}}), \tag{3.10}$$

for magnitudes in the Vega system and then converted to the $b_{\rm J}$ band using the correction $M_{b_{\rm J}} = M_{\rm B} - 0.072$ (Croom et al., 2009b). Predictions are shown for the Fan10b and for comparison, the predictions from the modified version of the Bower et al. (2006) model (solid orange lines) presented in Chapter 2 (Fan10a). The Fan10a model was constrained to match the observed LF of quasars at $z \sim 0.5$. In brief, the model assumes a constant obscuration fraction of $f_{\rm vis} = 0.6$ and a $b_{\rm J}$-band bolometric correction of 0.2. Finally, our predictions for the $z = 0$ LF, after applying the obscuration effect, are shown in every redshift bin (black dotted lines) to help us assess the evolution with redshift.

Our predictions are compared to the 2SLAQ+SDSS QSO LFs (Croom et al., 2009b). QSO magnitudes in the 2SLAQ sample were obtained in the g-band and therefore need to be converted to the $b_{\rm J}$ band considered here. We use $M_{b_{\rm J}} = M_g + 0.455$ (Croom et al., 2009b) where the K-corrections for the g band have been normalized to $z = 2$. In addition, we plot the 2QZ LFs by Croom et al. (2004). The observed LFs agree very well with each other particularly at bright magnitudes ($M_{b_{\rm J}} < -24$). The modest disagreement seen at the faintest magnitudes is due to the different K-correction applied to the 2QZ QSO sample by Croom et al. (2004). For higher redshifts, we include the LF derived from the SDSS Data Release 3 sample (DR3, Richards et al., 2006). The SDSS DR3 LF is obtained in the i band, therefore we need to convert it to the $b_{\rm J}$ band. We use $M_{b_{\rm J}} = M_i + 0.71$, assuming a spectral index of $a_\nu = -0.5$ (Croom et al., 2009b).

The AGN model contains one free adjustable parameter that must be constrained by

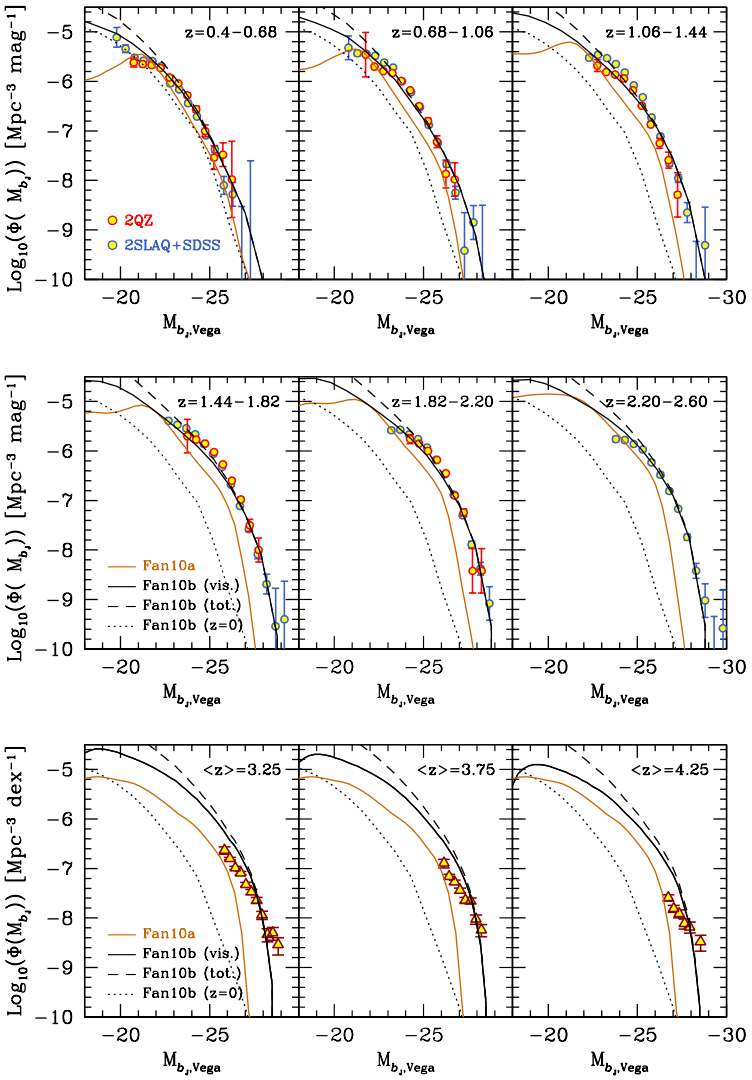

Figure 3.11: The b_J-band quasar LF in the redshift range $0.4 < z < 4.25$. Predictions are shown for the model described in this chapter (Fan10b; solid black lines) and the Fan10a (solid orange lines) model. For reference, we show the $z = 0$ LF in the Fan10b model (dotted black line). We also show the evolution of the LF in the Fan10b model before applying the obscuration (dashed black lines). The observations represent the LFs estimated from the 2SLAQ+SDSS (blue-filled circles, Croom et al., 2009b), 2QZ (red-filled circles, Croom et al., 2004) and SDSS (brown-filled triangles, Richards et al., 2006) surveys.

Table 3.3: Typical values of $f_{\rm vis}$ in three magnitude bins and its evolution with redshift.

	$M_{b_{\rm J}} = -20$	$M_{b_{\rm J}} = -24$	$M_{b_{\rm J}} = -28$
$z = 0.4$	53.3%	84.3%	100%
$z = 0.68$	49%	81%	100%
$z = 1.06$	44.9%	76.9%	100%
$z = 1.44$	42.2%	73.3%	100%
$z = 1.82$	27.8%	69.9%	100%
$z = 2.20$	24.7%	66.7%	98.7%

observational data. This is the $f_{\rm q}$ parameter in Eq. 3.2 which sets the accretion timescale. We choose the $b_{\rm J}$ band for constraining the value of $f_{\rm q}$ because it is the most sensitive to the modelling of AGN. Other free parameters are constrained by the galaxy formation model and are adjusted to reproduce the observed galaxy LFs (Bower et al., 2006; Lagos et al., 2010, see also Bower et al. 2010 for further discussion of our parameter fitting philosophy). Since $f_{\rm q}$ is essentially the only free parameter in our model, the predictions presented in these sections are genuine predictions of the underlying galaxy formation model. By fixing $f_{\rm q}$ to 10 we obtain an excellent overall match to the observed QSO LFs in the $0.4 < z < 2.6$ redshift interval. For higher redshifts, our model provides a good match, however, it predicts a much steeper slope for the bright end compared to the SDSS DR3 LF.

A comparison between the predictions for the $z = 0.4-4.25$ and $z = 0$ LFs in Fig. 3.11 shows that quasars undergo significant cosmic evolution. For example, quasars with $M_{b_{\rm J}} = -25$ increase in space density from $\sim 10^{-8}$ to $\sim 10^{-6}$ $\rm Mpc^{-3}$ between $z = 0$ and $z = 2.2 - 2.6$. This strong evolution in the space density of quasars is due to the fact that disc instabilities and galaxy mergers, the two processes that trigger accretion during the starburst mode, become more frequent at higher redshifts (see Fig. 3.1). Yet, the strong evolution of quasars does not affect only their space density. At a fixed space density of 10^{-8} $\rm Mpc^{-3}$ the quasar LF brightens from $M_{b_{\rm J}} \simeq -25$ at $z = 0$ to $M_{b_{\rm J}} \simeq -28$

at $z = 2.2 - 2.6$. This is attributed to the fact that the cold gas becomes more abundant with increasing redshift. This is equivalent to a strong increase in the gas reservoir available for feeding the central BHs since more gas is turned into stars when a starburst is triggered.

The processes that are responsible for driving the formation of stars in starbursts are also responsible for the cosmic evolution of quasars. Qualitatively, the strong link between the formation of stars and quasar activity (and therefore BH growth) can be illustrated by considering the Fan10a model. In Fig. 3.1 we can see that the SFR density in bursts in the Fan10a model shows a milder evolution with redshift compared to the Fan10b model. Hence, the model predicts that considerably less gas is available for accretion which then results in more modest evolution of the quasar LF. As a consequence, the predictions of the model Fan10a provide an overall poor match to the observed LFs.

The evolution of the SFR density with redshift does not imply a proportional evolution of quasar luminosities on the $M_{b_\mathrm{J}} - \Phi(M_{b_\mathrm{J}})$ plane. The space density of the brightest quasars increase with redshift. However, the density of objects around the break in the LF increases more quickly, leading to a steepening of the LF as illustrated by Fig. 3.11. This differential evolution is determined exclusively by the accretion physics in our model. In the $0.01 < \dot{m} < 1$ regime, the disc luminosity scales in proportion to $\dot{m}$. However, when the flow becomes substantially super-Eddington, the luminosity instead grows as $\ln(\dot{m})$ and therefore the dynamical range of predicted luminosities decreases dramatically. The logarithmic dependence of luminosity on the accretion rate has a strong impact on the shape of the LF, resulting in a very steep slope at the bright end. This becomes apparent in the highest redshift intervals ($z > 1.44$) where the relative number of super-Eddington accreting sources becomes significantly higher than in the lower redshift intervals (because more gas is available for accretion, see Fig. 3.9). Since these sources exclusively populate the brightest magnitude bins, the bright end of the LF now becomes significantly steeper.

Another factor that influences the evolution of the quasar LF is obscuration. Low luminosity quasars are heavily obscured according to our obscuration prescription, and thus remain well buried in their host galactic nuclei. This is clear from Table 3.3 where

we summarize the evolution of the $f_{\rm vis}$ value in the redshift range of interest. In the highest redshift intervals the obscuration becomes more prominent affecting even the brightest sources. However, the intense accretion activity during the starburst mode dominates the evolution of the faint end, and therefore a strong cosmic evolution in the space density of the faintest sources, similar to that of the brightest sources, is still observed. Nonetheless, the obscuration significantly influences the cosmic abundance of the quasar populations dominating the faint end, something that will become more evident in Section 3.6 where we will explore the cosmic evolution of quasars of given intrinsic luminosity.

Finally, we point out that those AGN that are powered by an ADAF contribute significantly to the space density of AGN fainter than $M_{b_{\rm J}} \simeq -22$ in the low redshift universe. In fact, in the range $0.4 < z < 0.68$, we find ADAF sources with $\dot{m} \simeq 0.001 - 0.01$ contributing also to the knee of the LF. These systems represent the rare $\gtrsim 10^9\,{\rm M}_\odot$ accreting BHs in Fig. 3.10. Identifying the ADAF systems with optically bright quasars introduces a caveat for the model since quasars typically show high excitation spectra which indicate the presence of a bright, UV thin disc (see e.g., Marchesini et al., 2004). Nonetheless, these systems accrete where the transition to a thin disc takes place. Observations of stellar mass BH binary systems show that this transition is complex, probably taking on a composite structure with the thin disc replacing the hot flow at progressively smaller radii (see e.g,. the review by Done et al., 2007). Such a configuration could possibly produce high excitation lines while retaining also the ADAF characteristics. For a more comprehensible representation of the objects populating the LF, we refer the reader to Fig. 3.14 in Section 3.5.4 where we decompose the LF into the contribution from ADAF, thin-disc, and also super-Eddington sources.

3.5.3 The X-ray LFs

The good agreement between our model predictions for the optical LF and the observations motivates us to study also the evolution of X-ray AGN as a function of redshift and intrinsic luminosity. X-rays account for a considerable fraction of the bolometric luminosity of the accretion disc and therefore provide an ideal band for studying the

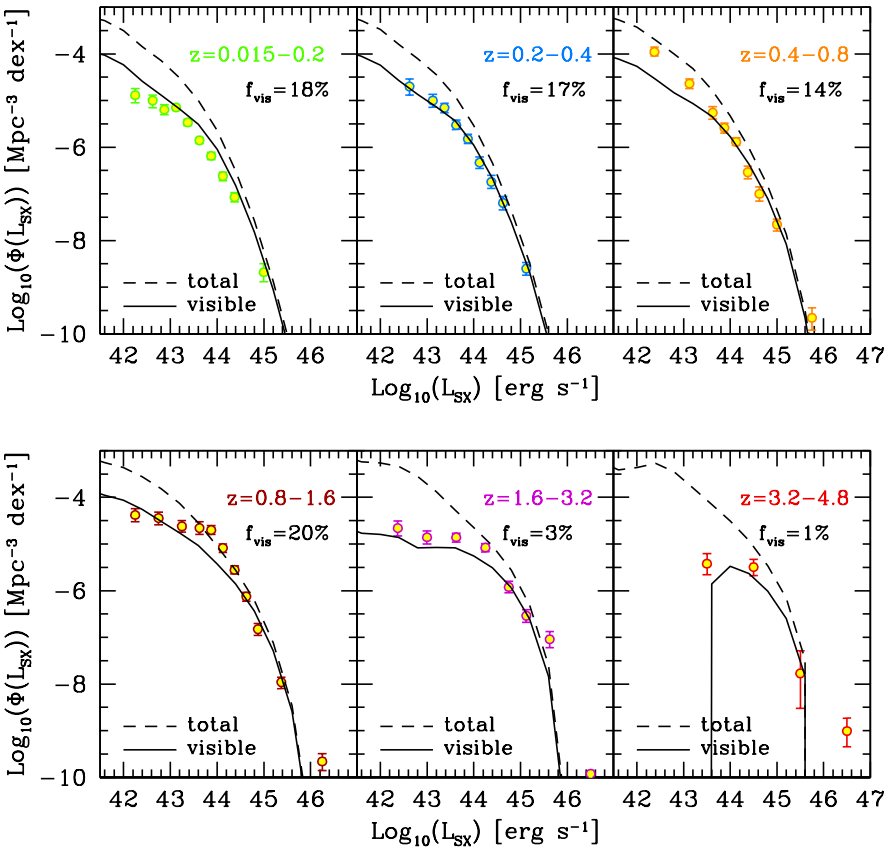

Figure 3.12: The predictions of our model for evolution of the soft X-ray LF (solid black lines). Predictions are shown before (total: dashed lines) and after (visible: solid lines) we apply the effects of obscuration. In addition, we quote the total fraction of AGN with $L_{\rm SX} > 10^{42}\,{\rm erg\,s^{-1}}$ that are visible in every luminosity bin. Data are taken from Ueda et al. (2003).

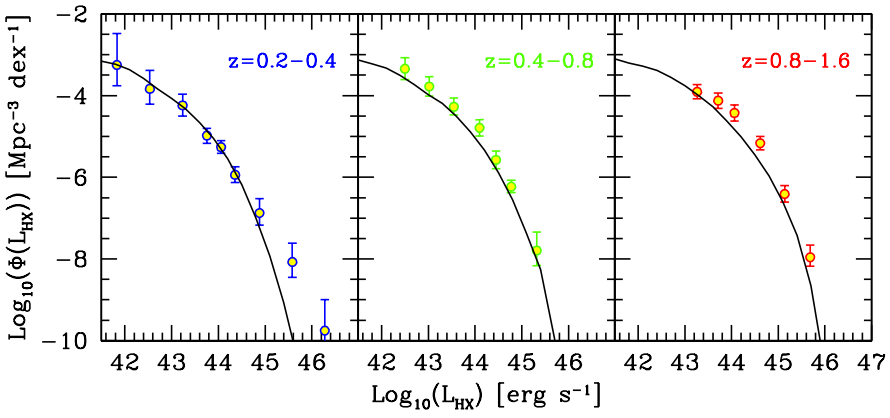

Figure 3.13: The evolution of the hard X-ray LF in our model (solid black lines). Predictions are shown only for $z < 1.6$ and no obscuration correction is applied. Observational data are taken from Hasinger et al. (2005).

cosmic evolution of AGN. The observed continuum spectra of AGN in the X-rays can be represented by a simple power law in the *hard* part of the spectrum ($2 - 10$ keV) with a universal spectral index of $\alpha_X \sim 0.7$ which is independent of the luminosity over several decades. In the *soft* part of the spectrum ($0.5 - 2$ keV) the power law continuum is strongly attenuated by absorption which is typically in excess of the Galactic value and corresponds to a medium with hydrogen column densities of $N_{\rm H} \simeq 10^{20} - 10^{23}$ cm^{-1} (Reynolds, 1997; George et al., 1998; Piconcelli et al., 2004).

The cosmic evolution of X-ray AGN has been investigated by employing AGN selected both in the soft (Miyaji et al., 2001; Hasinger et al., 2005) and hard part of the spectrum (Ueda et al., 2003; La Franca et al., 2005; Barger et al., 2005; Aird et al., 2010). Mirroring the strong evolution of the optical LF, the LF of X-ray selected AGN also evolves strongly with cosmic time. The LFs in soft and hard X-rays have similar characteristics, evolving at the same rate but differ significantly in normalization. For example, the Hasinger et al. (2005) soft X-ray sample has approximately a 5 times smaller global LF normalization compared to that of the hard X-ray LF estimated by Ueda et al. (2003). This difference is most likely attributed to the fact that a large fraction of AGN is obscured in the soft X-rays (type-2 AGN are by a factor of 4 more numerous than type-1

AGN, Risaliti et al., 1999).

We present in this section our predictions for the X-ray LFs. We calculate the X-ray emission in the $0.5-2\,\mathrm{keV}$ and $2-10\,\mathrm{keV}$ bands using Eq. (3.7). Our predictions for the soft and hard X-ray LFs are shown in Figs. 3.12 and 3.13 respectively (solid lines). The predictions are compared to the LFs estimated by Hasinger et al. (2005) for the soft X-rays and Ueda et al. (2003) for the hard X-rays. Note that we do not show estimates from observations that consist only of upper limits (empty bins). The Hasinger et al. sample comprises unabsorbed AGN and therefore we need to take this into account for the sample in the soft X-rays the effect of obscuration. We do so by using the Hasinger (2008) prescription as explained in the previous section. To quantify the effect of absorption we also plot in the soft X-rays the total population of AGN (dashed lines).

Overall, our model provides a very good match to the observations in both soft and hard X-rays. We find discrepancies between the observations and the model predictions in the redshift range $z=0.4-0.8$, where the space density of the $<10^{43}\,\mathrm{erg\,s^{-1}}$ soft X-ray AGN is under predicted. A similar disparity is also seen in the $z=0.8-1.6$ bin for the $10^{43}-10^{45}\,\mathrm{erg\,s^{-1}}$ AGN. However, it is important to bear in mind that our predictions in the soft X-rays depend strongly on our prescription for the obscuration. Since our predictions for the total AGN population are always well above the observations, it is likely that these discrepancies are attributed to the modelling of the obscuration. We also find that the model predicts at high redshifts a somewhat steeper bright end compared to the observations, although the very brightest point could be due to beaming effects in a small fraction of the more numerous lower luminosity sources (Ghisellini et al., 2010). Nonetheless, the very steep slope in our predictions is again a manifestation of the Eddington limit applied to the super-Eddington sources, an effect that becomes more significant at higher redshifts as already explained in the previous section.

As illustrated by the predictions for the soft X-ray LF in Fig. 3.12, the space density of the faintest soft X-ray AGN in our model is strongly affected by the obscuration. As illustrated by the LFs in the soft X-rays, AGN with $L_{\mathrm{SX}}\simeq 10^{42}-10^{44}\,\mathrm{erg\,s^{-1}}$ are heavily obscured. In fact, in the redshift interval $z=0.015-0.2$ only 19% of the total AGN population with $L_{\mathrm{SX}}\geqslant 10^{42}\,\mathrm{erg\,s^{-1}}$ is visible in soft X-rays. Hence, the obscured AGN

outnumber the visible AGN by a factor of 4 (Risaliti et al., 1999). This fraction of visible AGN becomes even smaller at higher redshift because the obscuration becomes more prominent with redshift. At $z > 3.2$ only a negligible fraction of the AGN are seen in soft X-rays. Based on these results we estimate that approximately 10% of the total number of AGN with $L_{\rm SX} \geqslant 10^{42}\,{\rm erg\,s^{-1}}$ are visible in the soft X-rays in the $z = 0.015 - 4.8$ universe. We note that these estimations are based on the obscuration model which according to the AGN sample from Hasinger (2008) is evaluated only for luminosities $10^{42}\,{\rm erg\,s^{-1}} < {\rm L_{HX}} < 10^{46}\,{\rm erg\,s^{-1}}$. For luminosities lower than $10^{42}\,{\rm erg\,s^{-1}}$ we assume that $f_{\rm vis}$ remains constant and equal to $f_{\rm vis}(10^{42}\,{\rm erg\,s^{-1}})$. It is therefore likely that we underestimate the value of $f_{\rm vis}$.

3.5.4 The bolometric LF

We have so far studied the LF of AGN and quasars in different wavebands using the bolometric corrections in Eq. (3.7) and compared them to the available observations. We find that our predictions match reasonably well the observations, particularly in the $b_{\rm J}$ band. Further insight into the evolution of AGN can be gained by calculating the bolometric LF and studying its evolution with redshift. This will provide an overall characterisation of the global AGN population and might reveal additional trends which are perhaps unseen when exploring the LF in the other bands we studied earlier.

To calculate the bolometric LF we consider all accreting objects (in both the starburst and hot-halo mode) taking into account the regime these objects accrete in (ADAF or thin disc). This time we probe a wider baseline in luminosity and thus we expect to see clearly the contribution of the AGN powered by ADAFs. We calculate the bolometric LF at some redshift z following the technique described in the previous sections. AGN are sampled over a period equal to 20% of the age of the universe at redshift z. We need to stress that the resolution of the Millennium simulation has an impact on the gas properties of the $\lesssim 10^{44}\,{\rm erg\,s^{-1}}$ objects at high redshifts. Therefore, we compare the N-body results with high-resolution simulations using Monte-Carlo (MC) halo merger trees to test the limit of our predictions. The MC algorithm we use to generate the DM halo merger trees has been presented in Parkinson et al. (2008). The algorithm is a modification of

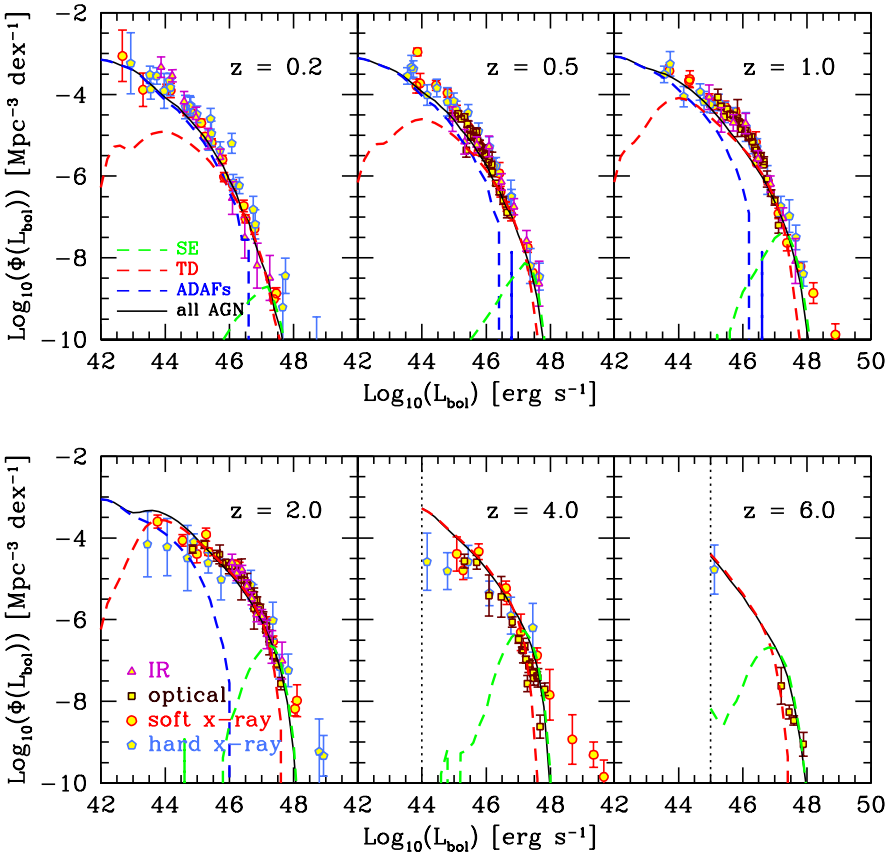

Figure 3.14: The bolometric LF predicted by our model in 6 redshift bins between $z = 0.2$ and $z = 6$. Also shown is the bolometric LF estimated by Hopkins et al. (2007) using a large sample of infrared (IR) optical, soft and hard X-ray LFs (we refer the reader to Hopkins et al. 2007 for a description of the observational samples used by the authors). The different bands are depicted by different colours as indicated by the labels. The dashed lines show the contribution to the LF of the ADAF (blue), thin disc (red) and super-Eddington sources (green). The vertical dotted lines indicate the resolution limit of the Millennium simulation.

the Extended Press-Schechter algorithm described in Cole et al. (2000) and accurately reproduces the conditional MFs predicted by the Millennium N-body simulation. The comparison shows that the calculation with N-body trees becomes incomplete for $L_{\rm bol} \lesssim 10^{44} - 10^{45}\,{\rm erg\,s^{-1}}$ AGN at $z \gtrsim 4$. Therefore, at high redshifts we show predictions only down to the resolution limit of the Millennium simulation (the limit is indicated by the vertical dotted lines).

Our predictions for the bolometric LF are shown in Fig. 3.14 (solid black lines) in the redshift range $z = 0.2 - 6$. In addition, we show independently the contribution to the LF from the ADAF, thin-disc, and $L_{\rm bol} \geqslant L_{\rm Edd}$ sources (dashed coloured lines). Our results are compared to the bolometric LF extracted from observations by Hopkins et al. (2007), using a combination of a large set of observed LFs in the optical, X-ray, near- and mid-infrared wavebands. The authors are able to reproduce the bolometric LF and the individual bands by employing their best-fit estimates of the column density and spectral energy distribution, but also a prescription for the obscuration fraction which is assumed to be a function of the luminosity (though not of redshift). Their AGN LF also show the downsizing of AGN activity at low redshifts, which is expressed through the steepening of the faint-end slope below $z = 1$. The data used by Hopkins et al. cover redshift wide redshift ranges and sometimes the same data sets appear in more than one bin (especially the soft X-ray data at $z > 0.8$). Therefore, comparison between the data and our predictions should be treated with caution because the observations over such wide redshift bins could hide evolutionary trends.

Nevertheless, our predictions for the bolometric LF match very well the observational estimates across a wide range of redshifts. In the low-redshift universe ($z \lesssim 1$), the model reproduces the faint and bright ends of the observed LF remarkably well. At the faint end, the model predicts a significant contribution from AGN powered by ADAFs. These are predominately massive BHs accreting at low accretion rates during the hot-halo mode and they account for the increasing abundance with decreasing redshift of the faint AGN (see also Fig. 3.9). By contrast, the bright end is always populated by AGN radiating near or greater than the Eddington limit. These are the AGN that harbour the rapidly growing $10^7 - 10^8\,{\rm M_\odot}$ BHs in the low-redshift universe.

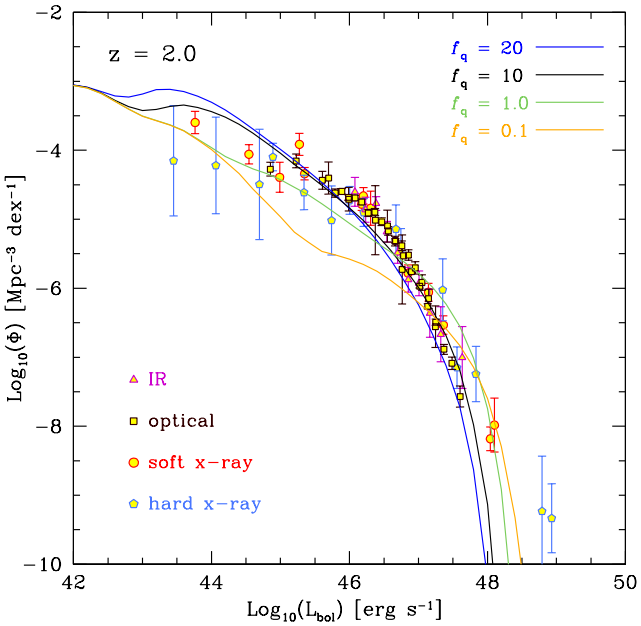

Figure 3.15: Our predictions for the bolometric LF at $z = 2$ considering four different values of the accretion timescale parameter,$f_{\rm q}$, as indicated in the legend. Data are taken from Hopkins et al. (2007).

At high redshifts ($z \gtrsim 1$), the contribution from the ADAF sources becomes less important. This is because not only fewer haloes reach quasi-hydrostatic equilibrium, but also most of the accretion during the starburst mode takes place in the thin-disc regime. The LF at these redshifts is dominated by AGN whose BHs accrete during the starburst model. The BHs in these AGN grow very fast as they usually double their mass several times during a single accretion episode. This gives rise to a strongly evolving population of super-Eddington sources that dominate the bright end of the LF.

The bright end of the $z \geqslant 1$ bolometric LF has a very steep slope compared to the observational estimate, indicating a deficiency of very bright quasars ($L_{\rm bol} > 10^{48}\,{\rm erg\,s^{-1}}$). The inability of the model to predict the luminosities of the most luminous quasars is due to the fact that the accretion luminosity is constrained by the Eddington limit. As discussed before, applying the Eddington limit to the accreting sources in our model results in a very steep decline in the space density of the super-Eddington sources, an effect clearly seen earlier in the optical LF.

To achieve higher quasar luminosities we need to increase the accretion rates in the most massive BHs to values much higher than the Eddington rate[1]. This is necessary because even if we assume that all our BHs accrete at the Eddington limit the maximum luminosity we can produce is $\sim 10^{48}\,\mathrm{erg\,s^{-1}}$ (when we consider, for example, a $10^{10}\,\mathrm{M_{\odot}}$ BH) which is still lower than the highest luminosities observed. Note though that, AGN feedback prevents BHs more massive than $10^{9}\,\mathrm{M_{\odot}}$ from accreting at or near super-Eddington accretion rates in our model.

To increase the accretion rate of a BH we can either increase the amount of gas that is fed into it or decrease the accretion timescale. The former solution corresponds to increasing the value of $f_{\rm BH}$ (the parameter that determines the fraction of gas available for accretion) which has already been tuned to provide a good match to the local BH density and MF. The latter solution gives us the freedom to adjust the accretion rates without changing the BH mass properties. By decreasing the value of $f_{\rm q}$ in Eq. 3.2 we can obtain higher $\dot{m}$ values and therefore boost the produced bolometric luminosities to $L_{\rm bol} > 10^{48}\,\mathrm{erg\,s^{-1}}$. This is illustrated in Fig. 3.15, where we show the bolometric LF at $z = 2$ assuming $f_{\rm q} = 20, 10, 1$ and 0.5. However, changing the value of $f_{\rm q}$ has a strong effect on the faint end of the LF since it decreases the space density of the low accretion rate objects (the space density of the $\lesssim 10^{43}\,\mathrm{erg\,s^{-1}}$ AGN remains unchanged since that part of the LF is dominated by AGN in the hot-halo mode in which the accretion timescale is derived directly from the cooling timescale of the gas). In addition, it reduces significantly the duty cycle of actively growing BHs by limiting the typical accretion timescale to $\sim 10^{5} - 10^{6}$ yr if $f_{\rm q} \leqslant 1$. Hence, having a constant value of $f_{\rm q}$ for all the accreting BHs limits our ability to account for the entire $L_{\rm bol}$ baseline. Perhaps this suggests that a more sophisticated treatment of the accretion timescale is therefore needed. However, this is beyond the scope of the present analysis.

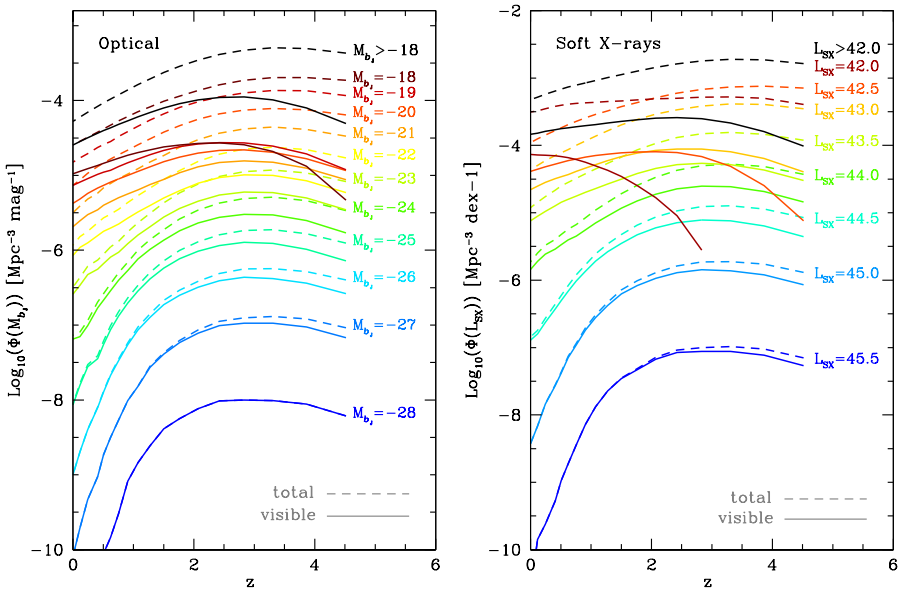

Figure 3.16: The cosmic evolution of different magnitude and luminosity classes of AGN selected in the optical M_{b_J}-band (left panel) and soft X-rays (right panel) respectively. In addition, we show the cosmic evolution of the sum of all AGN with $M_{b_J} \leqslant -18$ in the optical and $\log L_{\rm SX} \geqslant 10^{42}\,{\rm erg\,s^{-1}}$ in the soft X-rays (black lines). In all cases we show with dashed and solid lines the evolution of the space density of AGN before (total) and after (visible) applying the effects of obscuration.

3.6 The evolution of cosmic AGN abundances: cosmic downsizing?

Our predictions for the optical, X-ray and bolometric LFs, suggest that AGN undergo important cosmic evolution. Their space density was significantly higher at earlier epochs, an evolutionary trend which suggests that AGN activity in the past was much more intense. Interestingly, our predictions indicate that the effects of the different physical processes considered here (the two accretion modes and the obscuration prescription) must have an important, and indeed variable, effect on the evolution of faint and bright AGN. Therefore, to gain more insight into the cosmic evolution of AGN we study how the abundance of different luminosity populations of AGN evolves with redshift. This is shown in Fig. 3.16, where we show the cosmic evolution of optically selected AGN in 11 magnitude bins (left panel) and soft X-ray selected AGN in 8 luminosity bins (right panel). We have depicted separately the evolution of the total number of AGN (before applying obscuration; dashed lines) and visible population of AGN (after applying obscuration; solid lines) in each bin. In this figure we also show the sum over all magnitudes with $M_{b_{\rm J}} \leqslant -18$ and luminosities with $\log L_{\rm SX} \geqslant 10^{42}\,{\rm erg\,s^{-1}}$ (black solid lines for the visible and black dashed lines for the total populations).

A feature immediately evident in both wavebands is that the evolution of the space density of AGN is shallower for fainter sources. For example, in the optical waveband the increase in the space density of the $M_{b_{\rm J}} = -21$ AGN is characterized in the redshift interval $z = 0 - 1$ by a power law of the form $(1+z)^{\beta}$ with a very shallow slope of $\beta \sim 0.5$. The slope becomes gradually steeper reaching a value of ~ 2.3 for the $M_{b_{\rm J}} = -26$ AGN. The steepening of the slope is evident in both the total and visible populations and it is driven primarily by the two distinct accretion channels in our model as follows. The faintest sources depicted in the plots of Fig. 3.16 comprise a combination of objects accreting during the starburst and hot-halo mode. The hot-halo mode is responsible for building up the majority of them in the low redshift universe whereas the starburst mode accounts for them exclusively in the high redshift universe (cf. Figs. 3.9 and 3.10, but

[1]For comparison, a BH accreting at $\dot{m} \sim 100$ is only ~ 5 more luminous that a BH accreting at $\dot{m} = 1$.

also Fig. 3.14). The slope of these populations changes very slowly since the transition from the hot-halo mode to starburst-mode domination is not characterized by a strong change in the space density of AGN (the decrease of hot-halo sources is compensated by the increase of starburst sources). However, when we consider brighter populations, the contribution of the hot-halo mode becomes less important (or vanishes for the brightest populations). As a consequence, in the low redshift universe we find a much steeper slope for the bright AGN since their evolution is driven primarily by the starburst mode.

A second noticeable feature is the strong reduction of the visible populations compared to the total AGN populations. The effect is stronger in the faintest populations where we see a decrease in the space density of AGN sometimes greater than an order of magnitude. This has a significant effect on the redshift at which the space density of AGN peaks. For example, the space density of the $M_{b_{\rm J}} \leqslant -18$ and $\log L_{\rm SX} \geqslant 10^{42}\,{\rm erg\,s^{-1}}$ AGN (dashed black lines) peaks at $z \simeq 3.5$, which is the same redshift where the SF in bursts peaks (Fig. 3.1). The same behaviour is seen also in the individual luminosity AGN populations in both the optical and soft X-rays. However, the visible population shows a different behaviour. AGN activity, as observed in the soft X-rays for example, seems to peak at $z \sim 2-2.5$, much later than that of the total AGN population. More interestingly, when considering each luminosity population separately we notice that the brightest sources peak at $z \sim 3$ whereas the faintest ones at $z \lesssim 2$. Similarly, although less obviously, in the optical the space density of the faintest quasars peaks at $z \sim 2$ whereas that of the most luminous increases monotonically until $z \simeq 3$. This behaviour is ascribed to the fact that fainter populations are subject to stronger obscuration. Therefore their abundance reaches a maximum at lower redshifts and beyond that it declines faster. The strong obscuration also contributes to the further flattening of the slope making the evolution of these AGN quite modest.

Trends similar to those seen in the cosmic evolution of AGN in our model have been reported in the literature. For example, Hopkins et al. (2007) find in their analysis of the bolometric LF that faint AGN evolve much more slowly than bright AGN (Fig. 9 in their analysis). The modest evolution is evident also in the optical and soft/hard X-rays. In addition, Hasinger et al. (2005) report that in their sample of soft X-ray AGN, the redshift

at which the space density of AGN peaks changes significantly with luminosity: the peak of AGN with $10^{42}\,\mathrm{erg\,s^{-1}} < \mathrm{L_{SX}} < 10^{43}\,\mathrm{erg\,s^{-1}}$ is at $z \simeq 0.7$ but gradually shifts to higher redshifts, reaching $z \simeq 2$ for $10^{45}\,\mathrm{erg\,s^{-1}} < \mathrm{L_{SX}} < 10^{46}\,\mathrm{erg\,s^{-1}}$. Similarly, Croom et al. (2009b) found the same downsizing behaviour in the optical sample of quasars from 2SLAQ+SDSS. The faintest quasars in their sample peak at $z \sim 0.6 - 0.8$ ($-21.5 \geqslant M_g \geqslant -22.5$) whereas the brightest sources ($M_g \leqslant -25.5$) seem to monotonically increase in density up to $z \simeq 2.5$. Further evidence that the redshift at which the space density of quasar peaks is a strong function of luminosity form the analysis of Croom et al. is the inability of pure luminosity evolution models (PLE; models where only the luminosity of objects changes) to provide an excellent fit to the data. Instead, luminosity and density evolution (LEDE; models where both the luminosity and density of objects change) are needed to provide the best fit to the data.

These predictions pose the following key question. Why does AGN activity shift from high-luminosity objects in the high-z universe to low-luminosity objects in the low-z universe? Is this clear evidence against hierarchical galaxy formation models as has been interpreted by many authors? In our model, the downsizing of AGN is expressed through the shallow slope that characterizes the evolution of faint AGN and the dependence on luminosity of the redshift at which the AGN density in a given luminosity range peaks. The former arises naturally from the interplay of the starburst and hot-halo mode, just as in the galaxy population (Bower et al., 2006). Therefore, the SF and cooling processes in a hierarchical cosmology can account consistently for the different evolution with redshift of the individual luminosity populations. The latter is driven largely by obscuration biases rather than the nature of their host galaxies. The analysis presented earlier in this section shows clearly that the cosmic evolution of the AGN space density is subject to strong obscuration which depends significantly on both luminosity and redshift. Therefore, AGN populations that are subject to obscuration could lead to misleading conclusions. For example, in both the Croom et al. (2009b) QSO (these are only type-1 AGN Croom et al. (2009a)) and Hasinger et al. (2005) soft X-ray AGN samples no correction for obscuration is adopted. Given that at low redshifts only unabsorbed AGN are detected in soft X-rays (La Franca et al., 2005), these samples can only trace the

evolution of a small fraction (and also a specific class) of the total AGN population.

Hence, to probe the intrinsic evolution of AGN one needs to correct for observational biases caused by obscuration (note also that incompleteness effects at low luminosities and high redshifts could also influence observational results about the evolution of AGN). Ueda et al. (2003) investigated the cosmological evolution of hard X-ray AGN using a combination of surveys such as the HEAO 1, ASCA and Chandra. The sample of AGN constructed by Ueda et al., which was compared to our predictions for the hard X-ray LF in Section 3.5.3, was corrected using an absorption distribution function that depends on both the luminosity and redshift. In a similar analysis, La Franca et al. (2005) used a sample of AGN from the HELLAS2XMM survey to study the evolution of the hard X-ray LF taking into account selection effects due to X-ray absorption. In both these studies, a careful examination of the "cosmic evolution" plots (Fig. 12 in Ueda et al. and Fig. 8 in La Franca et al.) reveals no evidence for downsizing in hard X-rays.

When accounting for these effects, our model suggests that the cosmic interplay between the starburst and hot-halo mode results in complex evolution scheme for the AGN. In this scheme, low luminosity AGN avoid the cosmic fate (namely becoming dramatically less numerous with time) of their bright counterparts, since accretion during the hot-halo mode provides gas for enabling modest AGN activity in the low-z universe. Note that, as already implied by our analysis, modest activity implies low accretion rates rather than low BH masses. The AGN in the hot-halo mode show a wide range of BH masses, and therefore, in our model the AGN downsizing *does not* imply that the growth of low-mass BHs is delayed to low redshifts. Averaged-sized BHs accreting at low rates as an interpretation of the reported AGN downsizing is also supported by observations of X-ray selected AGN in the Chandra Deep Field South at $z < 1$ (Babić et al., 2007).

3.7 Conclusions

In this chapter we have made predictions for the evolution of AGN using the `GALFORM` model. Along with the extension for calculating the BH spin, we have introduced an improved SF law, as implemented by Lagos et al. (2010).

Using this model we calculate the cosmic evolution of the fundamental parameters that describe BHs. These are the BH mass, $M_{\rm BH}$, BH spin, a, and accretion rate onto the BH, $\dot{m}$ (expressed in units of the the Eddington accretion rate through out this chapter). We find that at high redshifts ($z \sim 6$) it is mainly the $10^6 - 10^7\,{\rm M}_\odot$ BHs accreting at $\dot{m} \simeq 0.3$ that are actively growing. This picture changes at lower redshifts where we find that the accretion activity peaks for $10^7 - 10^8\,{\rm M}_\odot$ BHs, accreting at $\dot{m} \simeq 0.05$. Throughout the evolution of these BHs their spin is kept low because of the chaotic fashion with which gas is consumed. However, when these BHs grow to masses of $\gtrsim 5 \times 10^8\,{\rm M}_\odot$ they acquire high spins as a consequence of mergers with other BHs.

Knowledge of the values of $M_{\rm BH}$, a and $\dot{m}$ allows us to calculate the luminosity produced during the accretion of gas. To do so, we assume that accretion takes place in two distinct regimes: the thin-disc (radiatively efficient) and ADAF (radiatively inefficient) regime. Objects accreting in the thin-disc regime are luminous enough to account for the observed luminosities of AGN. Using the luminosities predicted for each AGN (formed when the central BH experiences an accretion episode) and a prescription for taking into account the effects of obscuration (Hasinger, 2008) we calculate the LF of all accreting objects in the optical, soft and hard X-rays. We find a very good agreement with the observations, particularly in the optical, by adjusting the value of the $f_{\rm q}$ parameter, namely the proportionality factor that determines the accretion timescale in our model.

The presence of two distinct accretion channels naturally causes a downsizing in the predicted AGN populations. These channels shape the evolution of the faint AGN with cosmic time, indicating that the faint end of the LF is dominated by massive BHs experiencing quiescent accretion. By contrast, the bright end is always populated by AGN radiating near or greater than the Eddington limit. In addition, our model suggests that a significant fraction of AGN are obscured in optical and soft X-rays. In fact, we find that $\sim 90\%$ of the total number of AGN in the $z = 0.015 - 4.8$ universe are not visible in soft X rays. The implications of the obscuration are further revealed when we study the cosmological evolution of AGN of different luminosity populations. As demonstrated by Fig. 3.16, low luminosity AGN populations are strongly attenuated by obscuration. As a result, their peak of AGN activity appears shifted to lower redshifts.

Chapter 4

The early evolution of BHs and the appearance of the first quasars

4.1 Introduction

In this chapter we study the growth of SMBHs and the properties of associated AGN in the early universe and calculate the fraction of DM haloes that host an actively growing BH, using the coupled model of galaxy and BH formation in a CDM universe developed in the previous chapter. We build our model upon DM halo merger trees obtained using a Monte-Carlo (MC) algorithm. This allows us to target the halo masses of interest at very high redshifts, which are typically beyond the group of N-body simulations which have been designed to study haloes in the present day Universe. The MC algorithm we use to generate the DM halo merger trees has been presented in Parkinson et al. (2008). The algorithm is a modification of the Extended Press-Schechter scheme described in Cole et al. (2000) and accurately reproduces the conditional MFs extracted from the Millennium N-body simulation.

4.2 Growing the first BHs

In addressing the formation of the first SMBHs, it is important to discuss the assumption made about the seed BH mass. In our model we assume a rather simple scenario were BHs grow from stellar-sized seeds ($M_{\rm BH,seed} = 1\,{\rm M}_{\odot}$). The mass of the seed grows

exponentially

$$M_{\rm BH} = e^{t/t_{\rm eff}} M_{\rm BH,seed}, \tag{4.1}$$

on a timescale $t_{\rm eff}$ proportional to the Salpeter timescale, $t_{\rm S} = 4.34 \times 10^8$ yr,

$$t_{\rm eff} = \frac{\epsilon c \sigma_{\rm T}}{4\pi G m_{\rm p} \lambda_{\rm Edd}} = \epsilon t_{\rm S}/\lambda_{\rm Edd}. \tag{4.2}$$

Here ϵ is the accretion efficiency (Novikov & Thorne 1973) and $\lambda_{\rm Edd} = L_{\rm bol}/L_{\rm Edd}$. The growth of BHs in our model is inextricably linked to the star formation in galaxies. When the host galaxy experiences a disc instability or galaxy merger, processes that trigger bursts of SF, cold gas becomes available for feeding the central BH. This channel is responsible for building most of the $\lesssim 5 \times 10^8\,{\rm M}_\odot$ BH mass in our model. Quiescent SF episodes in the disc are not considered to contribute to the BH mass build up since they do not provide an efficient mechanism for transferring gas to the vicinity of the BH. The first galaxies form when gas in haloes cools and flows towards the centre, and settles into a rotationally supported disk. As these galaxies are not very massive they are not strongly self-gravitating and therefore are dynamically stable. The majority of these galaxies are therefore expected to build stars in the quiescent mode. This is shown in Fig. 4.1, where we plot the total SFR density history and the contribution from the burst and quiescent SF modes. As expected, at $z > 12$ we find that the total SFR density is dominated by SF in the quiescent mode. This picture, however, changes at $z < 12$ were we see that more SF takes place in bursts. This is due to the fact that galaxies are more massive at $z < 12$ and therefore undergo disc instabilities more often. In addition, galaxy mergers become more frequent with increasing redshift, and therefore, the contribution of merger-driven bursts of SF becomes more important.

BH mass growth is initiated as soon as the host galaxy undergoes its first burst of SF. We assume that a fraction of the gas that is converted into stars during the burst is directly fed into the BH. The common fuelling channel that spheroid stars and BHs share contributes to a coeval evolution of the BH and host spheroid that is expressed through the $M_{\rm BH} - M_{\rm Bulge}$ scaling relation. In the redshift range we are interested in here, the $M_{\rm BH} - M_{\rm Bulge}$ relation is solely determined by the starburst mode. However, at lower redshifts additional mechanisms (hot-halo accretion and BH mergers) contribute

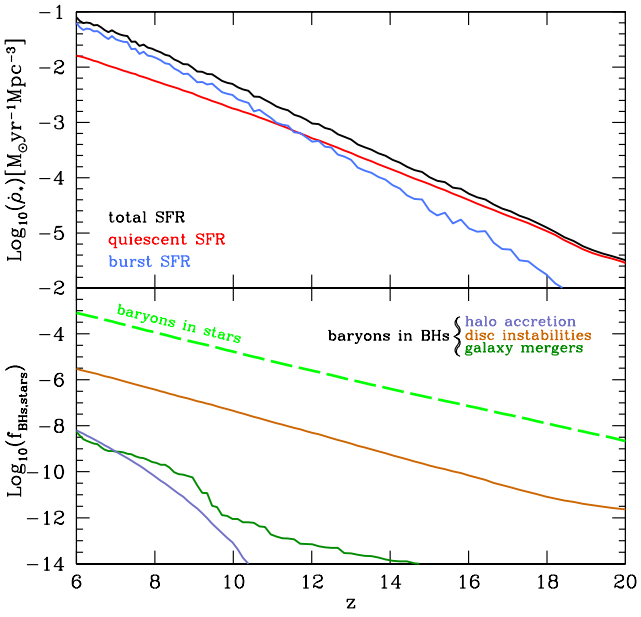

Figure 4.1: Top: The cosmic history of the total SFR density (black line). Also shown is the contribution from each SF activity mode, namely burst and quiescent SF (blue and red respectively), to the total SFR density. Bottom: The contribution of the accretion channels, namely the disc instability (orange), galaxy mergers (green) and quasi-hydrostatic halo accretion (blue) channel, to the total fraction of baryons locked in BHs. Also shown is the fraction of baryons in stars (dashed green line).

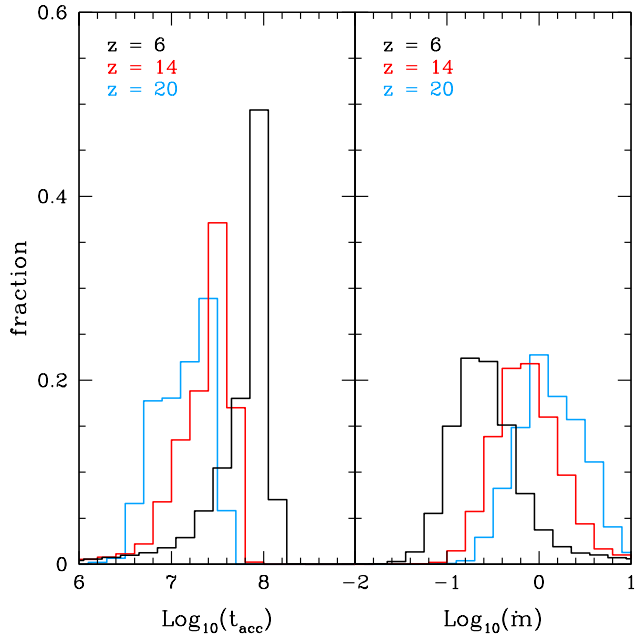

Figure 4.2: The distribution of the accretion timescale, $t_{\rm acc}$ (left plot), and accretion rate, $\dot{m}$ (right plot), at $z = 20, 14$ and 6 as indicated by the key.

to shaping of this scaling relation. The dominance of the starburst mode in the growth of BHs is illustrated in the bottom panel of Fig. 4.1. In this plot we show the fraction of baryons in the universe that has been delivered into BHs (solid lines) by the starburst mode (disc instabilities and galaxy mergers) and hot-halo mode (halo accretion). Mergers between BHs are not relevant in this plot because they only redistribute the baryons already locked up in BHs rather than adding new mass. In addition, we show the fraction of baryons locked up in long-lived stars and remnants (dashed line).

It is immediately obvious from Fig. 4.1 that the growth of BHs at $z > 6$ is driven exclusively by accretion triggered by disc instabilities. Accretion triggered by galaxy mergers and accretion from the hot halo make insignificant contributions to the total BH mass. Hence, BHs begin to grow efficiently when the disc of the host galaxy first becomes dynamically unstable, driving the flow of cold gas to the centre. Following the consumption of the cold gas in a starburst, further gas cooling from the hot halo will regrow the disc, a process which may be interrupted by a subsequent instability in the

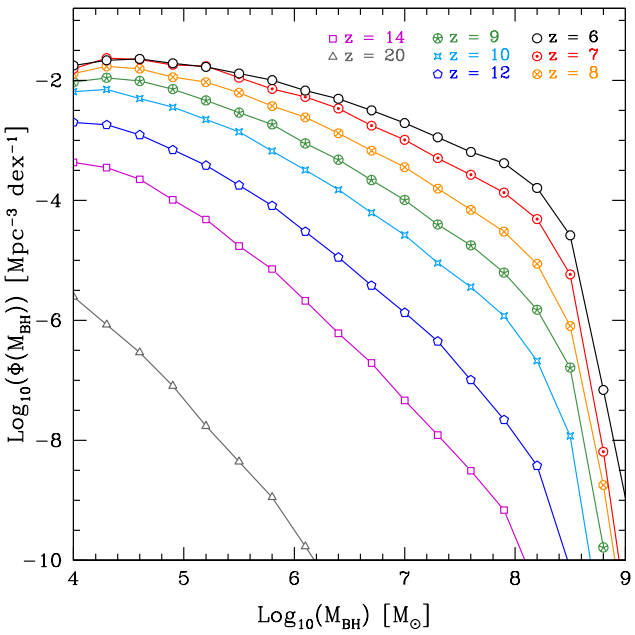

Figure 4.3: In these plots we show the evolution of the global MF of BHs in the $z > 6$ universe. Different redshifts are depicted with different colours and point types as denoted by the labels.

disc. A succession of accretion episodes during starbursts triggered by disc instabilities results in a fast build up of the BH mass. The close correlation between SF and BH growth becomes evident when we compare the fraction of baryons in BHs from disc instabilities (that basically represents the total fraction of baryons in BHs) to the fraction of baryons in stars. The two curves have approximately the same slope and differ only in normalisation.

Fig. 4.1 gives us an idea of how prodigious BH growth is in the early universe. The BH mass in the universe experiences a boost of 6 orders of magnitude between $z = 20$ and $z = 6$. Such an immense mass build up is the end result of the vast amounts of gas being accreted onto the first BHs at $z \gtrsim 14$. Note that the gas is assumed to be consumed on a timescale proportional to the dynamical timescale of the host bulge, $t_{\rm acc} = f_{\rm q} t_{\rm bulge}$. $f_{\rm q}$ is fixed for all the accretion episodes in our model and its value is tuned by fitting the observed LFs in optical and X-rays over the redshift range $0.4 < z < 4.8$ (see Chapter 3). At very high redshifts we find that the gas is fed onto the BHs during ephemeral

accretion episodes with typical duration of $\sim 10^7$yr. This is shown in Fig. 4.2, where we plot the distribution of accretion timescales (left panel) and accretion rates (right panel) at $z = 20, 14$ and 6. The accretion rate is expressed for convenience in Eddington units, $\dot{m} = \dot{M}/\dot{M}_{\rm Edd}$: a BH with $\dot{m} = 1$ accretes at the Eddington rate.

As shown in Fig. 4.2, the typical accretion timescale becomes longer with decreasing redshift. This is mainly because in our model the accretion timescale is assumed to be proportional to the dynamical timescale of the host spheroid. Therefore, as the galactic spheroids become more massive with decreasing redshift, the accretion duration, and thus the AGN lifetime, becomes correspondingly longer. At $z \sim 6$ we find that AGN have typical lifetimes of the order of ~ 100 million years. The evolution of the accretion timescale has a clear impact on the accretion rate. We find that accretion at $z = 20$ takes place in the super-Eddington regime, with most AGN accreting at $\dot{m} \gtrsim 1$. However, as redshift decreases so does the accretion rate. At $z = 6$, most of the AGN accrete in the sub-Eddington regime with typical accretion rates of $\dot{m} \simeq 0.2$.

The very high accretion rates in the high-redshift universe result in a fast build up of BH mass: only ~ 300 million years after the Big Bang the first $10^8\,{\rm M}_\odot$ BHs appear. Such an early appearance of very massive BHs is not a surprise. From Eq. 4.2 we have that e-fold time of the BH mass is $t_{\rm eff} = 4.34 \times 10^8 (\epsilon/\lambda_{\rm Edd})$ yr. The accretion efficiency, ϵ, has a typical value of ~ 0.07 in our model (see Chapter 3). Also, the $\lambda_{\rm Edd}$ parameter scales as $1 + \ln(\dot{m})$ in the super-Eddington regime, therefore from Fig. 4.2 we find that $\lambda_{\rm Edd}$ typically ranges between 1 and 3.5 at $z = 20$. The BHs with the highest accretion rates will therefore have an e-folding time of $t_{\rm eff} = 8.5 \times 10^6$ yr. This is a very short timescale that results in a sufficiently rapid, exponential growth of the BH mass.

To understand better the demographics characterising the BH mass we plot in Fig. 4.3 the evolution of the MF of BHs. Our calculation probes objects with a space density as low as 10^{-10} Mpc^{-3}, which would require a simulation volume in excess of $10\,{\rm Gpc}^{-3}$. As already discussed in the previous paragraph we find our first $10^8\,{\rm M}_\odot$ BHs at $z = 14$. In spite of the fact that initially these BHs are very rare, the plentiful abundance of gas in the early universe quickly boosts their space density. As redshift decreases between $z = 14$ and $z = 6$ we find that the abundance of the $\sim 10^8\,{\rm M}_\odot$ BHs increases by more than

6 orders of magnitude. A similar increase, but not as substantial, is also found for the less massive BHs. However, we find that BHs do not reach $\sim 10^9\,\mathrm{M}_\odot$ masses as fast as one might expect given the evolution of the $10^8\,\mathrm{M}_\odot$ BHs. Indeed, for BH masses higher than $\sim 5\times10^8\,\mathrm{M}_\odot$ the MF steepens strongly, delaying significantly the appearance of the $\sim 10^9\,\mathrm{M}_\odot$ BHs. In fact, the first $\sim 10^9\,\mathrm{M}_\odot$ BHs in our model appears only at $z\simeq 6$.

Responsible for the slow build up of the most massive BHs in our model is the AGN feedback process. When massive haloes reach quasi-hydrostatic equilibrium they become subject to AGN feedback that suppresses the cooling flows. Some of the mass which would have been involved in the cooling flow is instead accreted onto the BH during the hot halo mode. However, the amount of gas involved during this mode is usually very low and therefore it does not increase the BH mass as efficiently as the starburst processes. The different efficiency with which BHs grow during each mode causes a strong break in the MF whose appearance we witness already at $z\sim 10$.

The formation of the $\gtrsim 10^8\,\mathrm{M}_\odot$ BHs boosts significantly the comoving BH mass density. At $z=6$ we find $\rho_{\rm BH}(z=6)=5.5\times10^4\,\mathrm{M}_\odot\,\mathrm{Mpc}^{-3}$, only ~ 10 times lower than that at $z=0$. Our predicted value is in good agreement with the upper limit of $\rho_{\rm BH}\sim 4\times10^4\,\mathrm{M}_\odot\,\mathrm{Mpc}^{-3}$ inferred from the soft X-ray background at $z\sim 6$ (Salvaterra et al., 2005). 20 percent of the mass our model predicts is locked in the BHs with masses greater than $10^8\,\mathrm{M}_\odot$.

4.3 The first quasars

When disc instabilities provide the gas to be fed into the BHs the host galaxies undergo their first AGN phases (when accretion takes place in the thin-disc regime). The intense BH growth results in a significant increase in the space density of the galaxies that host an AGN. To gain insight into the evolution of the population of accreting BHs we calculate the bolometric luminosity function of AGN. Our method for calculating the AGN LF is extensively described in the previous chapter. In brief, we assume that accretion takes place in two distinct regimes, the thin-disc (luminous accretion with high accretion rates) and advection dominated accretion flow (ADAF, less luminous accretion with low

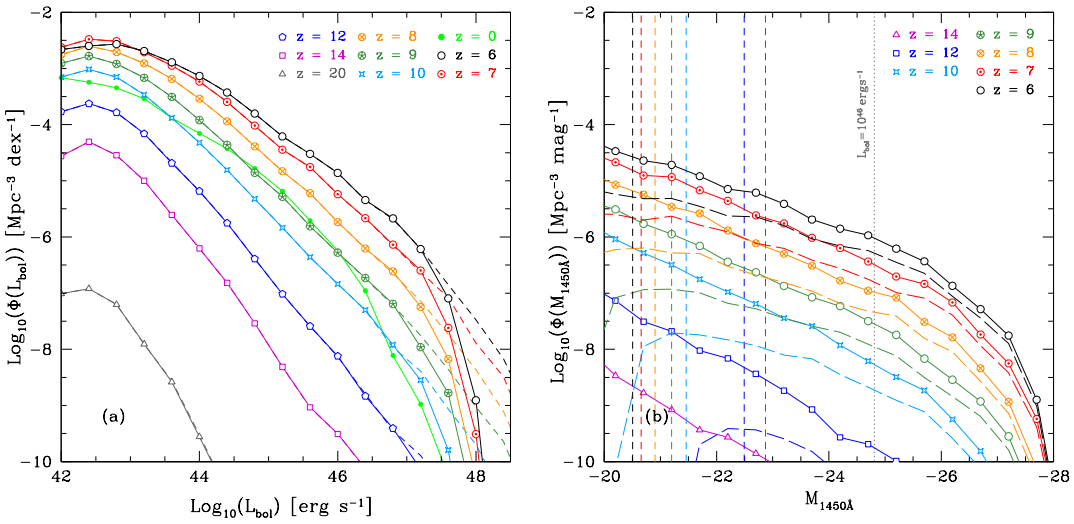

Figure 4.4: Top: The evolution of the bolometric luminosity function in the $z \geqslant 6$ universe. Predictions are shown with and without considering the Eddington limit (solid and dashed lines respectively). Different redshifts are depicted with different colours and point types as denoted by the labels. For comparison, we also show the bolometric LF at $z = 0$ (green line). Bottom: The 1450Å LF with and without obscuration (dashed and solid lines respectively) and its evolution with redshift. Also shown are the magnitude limits of the JWST at the denoted redshifts assuming $10\,\sigma$ detections of an integration time of $10\,000$ s.

accretion rates) regimes. For each accreting BH we calculate the bolometric luminosity produced taking into account the accretion regime and then we determine the comoving space density of AGN radiating in each luminosity bin. If the luminosity produced exceeds the Eddington limit ($L_{\rm bol} > L_{\rm Edd}$) we assume a logarithmic dependance of the luminosity on the accretion rate. This results in a weak evolution of the bright end of the AGN LF. Our predictions for the bolometric LF of AGN and its evolution for redshifts $z \geqslant 6$ are shown in Fig. 4.4a (solid lines with points). To illustrate the effect of the Eddington limit we also show our predictions without imposing a limit on the disc luminosity (short-dashed lines).

Fig. 4.4a shows that AGN undergo a truly remarkable cosmological evolution during the first Gyr of the universe. Already at $z = 14$ we have a significant population of $L_{\rm bol} \gtrsim 10^{42}\,{\rm erg\,s^{-1}}$ AGN that increases strongly with redshift. However, not all the AGN undergo the same evolution. Faint AGN seem to evolve modestly compared to bright AGN. For example, the space density of $\sim 10^{44}\,{\rm erg\,s^{-1}}$ AGN increases by approximately 3 orders of magnitude. In contrast, the $\sim 10^{46}\,{\rm erg\,s^{-1}}$ AGN increase by 6 orders of magnitude within the same redshift interval. Given that the $\sim 10^{46}\,{\rm erg\,s^{-1}}$ AGN are powered by accretion near the Eddington limit onto $10^8\,{\rm M_\odot}$ BHs, such an immense evolution demonstrates the prodigious build up of the $10^8\,{\rm M_\odot}$ BHs. However, the picture changes when we consider the brightest, $10^{47} - 10^{48}\,{\rm erg\,s^{-1}}$, AGN. These AGN are powered by super-Eddington accretion onto $10^8 - 10^9\,{\rm M_\odot}$ BHs and their luminosity output scales as the logarithm of the accretion rate. Such a dependance results in a break which is obvious when one compares the LF to the one calculated without imposing the Eddington limit.

We can define as quasars all galaxies that host an AGN with $L_{\rm bol} \gtrsim 10^{46}\,{\rm erg\,s^{-1}}$. This definition does not reflect any physical limit, however it is motivated by the fact that in $\gtrsim 10^{46}\,{\rm erg\,s^{-1}}$ AGN we find that the luminosity emanating from the nucleus dominates the energetics of, and therefore completely outshines, the host galaxy. Almost exclusively, these quasars inhabit in bulge dominated galactic systems ($B/T \gtrsim 0.6$) whose B/T could resemble the elliptical galaxies in our local Universe. From Fig. 4.4a we find that AGN with $\gtrsim 10^{46}\,{\rm erg\,s^{-1}}$ luminosities appear already at $z = 14$. Therefore, 300 million years

after the Big Bang is established in our model as the era of the first quasars.

One of the main scientific goals of the infrared space observatory JWST is to find the first quasars at high redshifts. JWST will carry onboard an extremely sensitive near infrared camera (NIRCam) that will cover a wavelength range of 0.6 to $5\ \mu\mathrm{m}$ and therefore it will be ideal for detecting the redshifted UV continuum radiation of the $z > 6$ quasars. For this purpose, we show in Fig. 4.4b the rest-frame UV LF of AGN at $1450\,$Å and its evolution with redshift (solid lines). We calculate AB magnitudes at 1450Å using the Marconi et al. (2004) bolometric corrections to estimate the emission in the B band and then we use $M_{1450} = M_{\mathrm{B}} + 0.626$ to convert in M_{1450} (Richards et al., 2006).

In addition, we show predictions for the $1450\,$Å LF when we take into account the effect of obscuration on the central source fuelling the AGN emission. The obscuring medium, perhaps dust, is assumed to originate from the host galaxy, affects mostly the low luminosity quasars and its effect becomes more prominent with increasing redshift (Hasinger, 2008). We quantify the obscuration by extrapolating to high redshifts the Hasinger 2008 prescription. We apply the effect of obscuration keeping in mind that this is a rather crude approach since the nature of the obscuration in AGN at very high redshifts is quite uncertain. For example, the detection of quasars at $z \sim 6$ with the Spitzer Space Telescope with no hot-dust emission perhaps suggests that the first generation of quasars are born in dust free environments (Jiang et al., 2010). Nonetheless, since our prescription for the obscuration is determined by the observations and not by a physical model, we cannot discriminate between first generation and evolved quasars. Therefore, we apply the effect of obscuration on all galaxies hosting an active nucleus.

Our predicted 1450Å LFs with and without the effect of obscuration are shown in Fig. 4.4b (dashed and solid lines respectively). In the same plot we show the magnitude limits of JWST at the redshifts at which we calculate the LF. These are calculated using the Wide NIRCam Filter sensitivities ($9.18 - 24.13$ nJy in the wavelength range $0.7 - 3.56\ \mu\mathrm{m}$, assuming $10\,\sigma$ detections of $10\,000\,$s). A comparison between the LFs with no obscuration and JWST limits in Fig. 4.4b shows that JSWT should be able to detect continuum radiation from quasars up to $z \sim 12$ (prospective detections depend of course on the integration time). When we consider the effect of obscuration, we expect more conser-

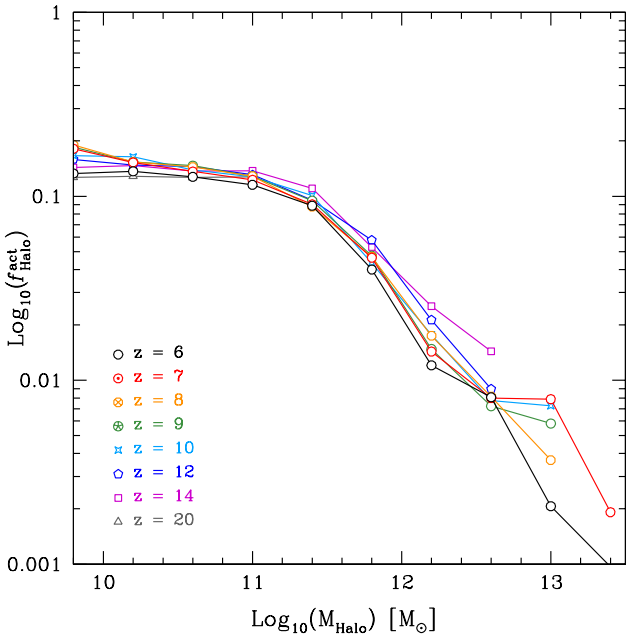

Figure 4.5: The fraction of haloes that host an actively growing BH, $f_{\rm Halo}^{\rm act}$, as a function of redshift.

vative detections since the obscuration decreases significantly the space density of faint quasars. In fact, we find that all quasars at $z > 14$ should be well buried deep within the dust of their host galaxies. Essentially, the first quasars visible at $1450\,$Å appear only at $z \lesssim 12$. A great fraction of the faintest of them still spend their lives veiled in dust. However, according to Fig. 4.4b there should still exist an important population of faint quasars within the magnitude limits of JSWT. On the other hand, quasars with $M_{1450} \lesssim -26$ shine almost freely below $z \sim 10$, since the obscuration affects little the very bright quasars. These quasars should be excellent candidates for JSWT.

4.4 The fraction of active haloes

The very short accretion episodes onto BHs in the early universe imply short duty cycles, namely a low fraction of BH that are actively growing at a given time. Evidently, short BH duty cycles imply that at a given time, BH growth, and therefore AGN activity, takes place in only a small fraction of the total number of DM haloes in the universe. We

illustrate this in Fig. 4.5 by showing the fraction, $f_{\rm Halo}^{\rm act}$, of DM haloes that have hosted an actively growing BH sometime during a period equal to 20 percent of the age of the universe at each redshift plotted. Our results are not sensitive to the previous choice of the fraction of the age of the universe.

Surprisingly, we find, as shown over several redshifts in Fig. 4.5, that there is hardly any evolution of $f_{\rm Halo}^{\rm act}$ with redshift. This indicates that the probability of finding an AGN in a DM halo of a given mass is always the same in the early universe. For haloes with masses $\lesssim 10^{11}\,{\rm M}_{\odot}$, this probability is approximately ~ 15 percent. For haloes of higher mass, the probability decreases significantly.

The substantial drop of the $f_{\rm Halo}^{\rm act}$ value above $10^{11}\,{\rm M}_{\odot}$ in halo mass is related to the AGN feedback. These haloes are the first ones entering they quasi-hydrostatic regime in which the cooling time of the gas in the halo is longer than its free-fall time. In these haloes feedback from the accreting BH is effective in injecting energy in the halo and suppressing cooling the flows. As a result, BH growth (but also the galaxy formation activity) becomes less efficient due to the smaller gas reservoir available to starbursts, which also results in the strong break seen in the BH MF near $M_{\rm BH} \sim 10^{9}\,{\rm M}_{\odot}$ in Fig. 4.3. Hence, very massive haloes are not very common environments for growing BHs.

Given the dependance of $f_{\rm Halo}^{\rm act}$ on the halo mass, we expect that AGN populate with the same frequency haloes with masses less than $10^{11}\,{\rm M}_{\odot}$ in the early universe. In this mass range we usually find AGN with $\lesssim 10^{44}\,{\rm erg\,s^{-1}}$ luminosities. Therefore, relatively low luminosity AGN trace the underlying distribution of low mass haloes with a constant sampling of 0.15. AGN with luminosities greater than $10^{44}\,{\rm erg\,s^{-1}}$ occupy haloes with $M_{\rm Halo} \gtrsim 10^{11}\ {\rm M}_{\odot}$, however, with a significantly low sampling. Note that the value of $f_{\rm Halo}^{\rm act}$ is very sensitive to the BH duty cycles. In our model the duty cycle is essentially determined by the value of the $f_{\rm q}$ parameter. Making $f_{\rm q}$ smaller results in an overall decrease in $f_{\rm Halo}^{\rm act}$, thus, decreasing the probability of a halo hosting an AGN.

4.5 Conclusions

We have presented predictions for the evolution of SMBHs and associated AGN in the redshift range $6 < z < 20$, using the model described in Chapter 3. We find that SMBHs at the centres of the first galaxies undergo huge growth spurts when the hosts experience disc instabilities. As a result of the prodigious accretion of gas the first 10^8 $\mathrm{M}_\odot$ BHs appear already at $z = 14$. Despite the early appearance of the 10^8 $\mathrm{M}_\odot$ BHs, the build up of more massive BHs is delayed because of the AGN feedback. Consequently, BHs reach masses of 10^9 $\mathrm{M}_\odot$ only at $z \simeq 6 - 7$.

Our model predicts that the first quasars with bolometric luminosities of $10^{46}\,\mathrm{erg\,s^{-1}}$ appear at $z = 14$. These quasars inhabit the most massive DM haloes in our simulation, however, with a significantly low sampling. In contrast less luminous quasars populate intermediate and low mass halos with a constant sampling of ~ 0.15. Finally, we predict that the JWST should be able to detect luminous quasars up to $z = 12$.

Chapter 5

The dependence of AGN activity and luminosity on environment: The clustering of AGN

5.1 Introduction

In this part of the thesis we present basic predictions for the environmental dependence of AGN formation and evolution. In particular, we calculate the two-point correlation function of AGN and study its dependence on luminosity and redshift. Knowledge of the two-point correlation function provides insight into the spatial distribution of AGN in the filamentary cosmic web of DM.

Following the definition from Peebles (1980), for given a galaxy, the two-point correlation function, $\xi(r)$, describes the excess probability that another galaxy will be found within a distance r from the first galaxy, compared with a random distribution. To calculate the two-point correlation function for a given galaxy population we use the following estimator,

$$\xi_{\rm gal} = \frac{\langle DD \rangle}{(1/2)N_{\rm gal} n \Delta V(r)} - 1, \tag{5.1}$$

where $\langle DD \rangle$ is the number of galaxy-galaxy pairs at separation r and $r + dr$, $N_{\rm gal}$ and n are the total number and mean number density of galaxies, and $\Delta V(r)$ is the volume of the shell between r and $r + dr$. The $1/2$ factor accounts for the double counting of galaxies. This estimator can be used in a periodic simulation volume in which the volume of

each annulus is known.

The two-point correlation function is a measure of the degree of clustering in the spatial (or angular) distribution of galaxies. If galaxies are unclustered, namely randomly distributed in space, then $\xi_{\rm gal} = 0$. A positive value of $\xi_{\rm gal} = 0$ means that galaxies are more clustered than a random distribution. The clustering of galaxies can be related to the clustering of the underlying DM through a bias parameter, b. The bias is an indication of how strongly galaxies are clustered relative to the DM and can be defined as (e.g. Kaiser 1984)

$$b(r) = \sqrt{\frac{\xi_{\rm gal}(r)}{\xi_{\rm dm}(r)}}. \tag{5.2}$$

In principle, on large scales the bias is scale independent, and therefore the distribution of galaxies can be related in a simple way to the distribution of DM. However, on small scales the complex interplay of the physical processes that drive galaxy formation results in a scale dependent bias. Knowledge of $\xi_{\rm gal}(r)$ and $b_{\rm gal}(r)$ provides a complete description of the spatial distribution of galaxies.

5.2 The clustering of quasars and radio galaxies

As a first step we calculate $\xi(r)$ for AGN at $z = 0$. This is shown in Fig. 5.1, for a sample of quasars (blue line) and radio galaxies (green line) with magnitude and luminosity cuts of $M_{b_{\rm J}} = -20$ and $P_{1.4{\rm GHz}} = 10^{22}\,{\rm W\,Hz^{-1}}$ respectively. In addition, we plot the two-point correlation function of the Millennium DM particles (solid black line). $\xi_{\rm dm}$ is calculated using a dilute sample of DM particles from the Millennium simulation. We do not calculate pairs for the total number of particles in the simulation ($\sim 10^{10}$) since that would be very costly computationally. Choosing a dilute sample of $\sim 10^7$ random particles is adequate to provide excellent statistics in the determination of $\xi_{\rm dm}$ down to $0.1\,h^{-1}$ Mpc.

Fig. 5.1 shows that the two-point correlation function of quasars, $\xi_{\rm q}$, is not a pure power-law. Our model predicts that $\xi_{\rm q}$ has a characteristic inflection on scales $\sim 2 - 3\,h^{-1}$ Mpc which is due to the transition from $\xi_{\rm q}$ being dominated by quasar pairs within the same halo on small scales (one-halo term) to quasar pairs in two different haloes on

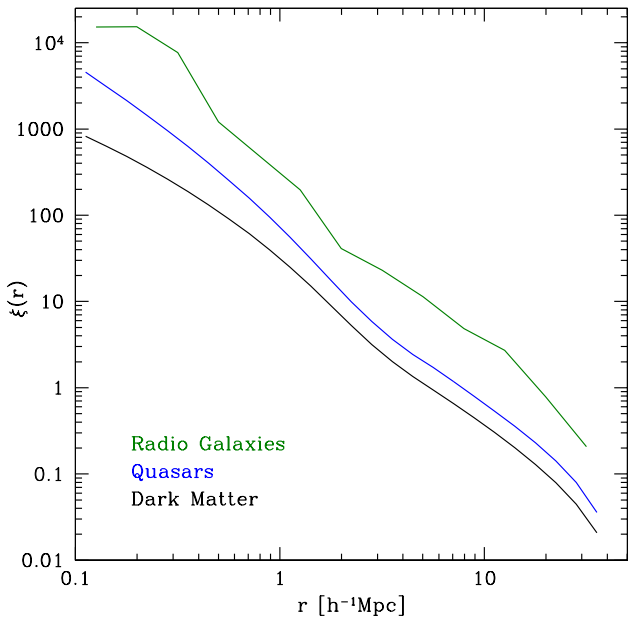

Figure 5.1: The two-point correlation function of radio galaxies (green line), quasars (blue line) and DM (black line) at $z = 0$. The radio-galaxy and quasar samples used for the calculation of $\xi(r)$ are limited to $M_{b_J} = -20$ and $P_{1.4\mathrm{GHz}} = 10^{22}\,\mathrm{W\,Hz^{-1}}$ respectively.

large scales (two-halo term). ξ_q is found to closely follow ξ_dm for $r \gtrsim 2 - 3\,h^{-1}\,\mathrm{Mpc}$ with an approximately constant bias of $b_\mathrm{q} = 1.33$. However, for scales smaller than $r \sim 1\,h^{-1}\,\mathrm{Mpc}$, ξ_q is very different from ξ_dm. On these scales we find that the bias increases with decreasing separation, which indicates that on small scales quasars become more clustered than the underlying DM.

Interestingly, our model suggests that radio galaxies and quasars are not clustered in the same way. We find that radio galaxies are more clustered than quasars on all scales, particularly on small scales. Radio galaxies are also strongly biased relative to the DM. The bias reaches a maximum of $b_\mathrm{rg} \simeq 4.3$ on scales of $\sim 0.1\,h^{-1}\,\mathrm{Mpc}$, which suggests radio galaxies have a preference for inhabiting peaks in the DM density distribution. Therefore, radio galaxies are expected to be biased tracers of the most massive DM haloes. Our predictions contradict the work by Smith and Heckman (1990) who found no difference between the clustering of radio galaxies and radio-quiet quasars using a

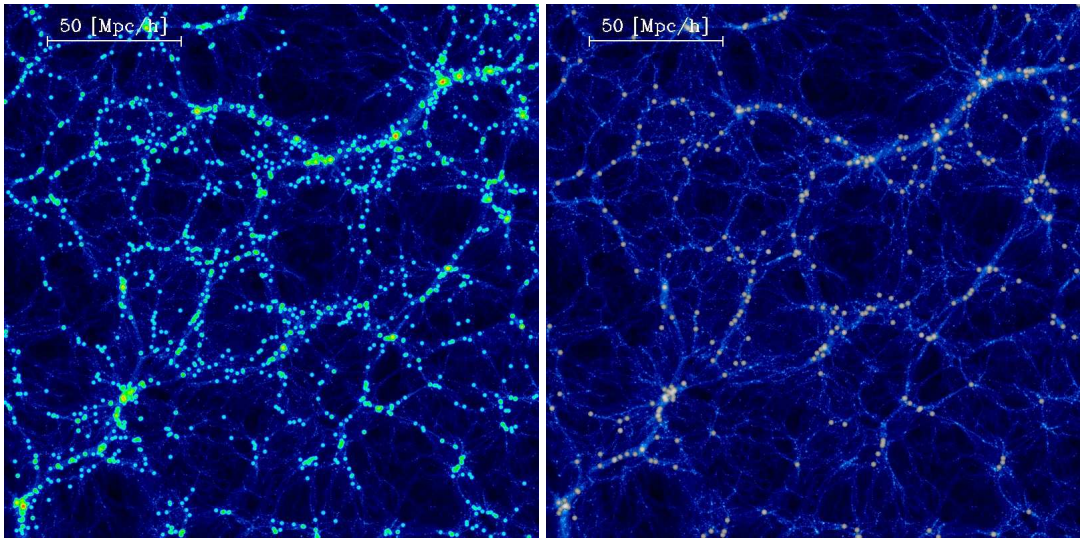

Figure 5.2: The distribution of quasars and radio galaxies at $z = 0$ in the Millennium simulation. The two panels show the same DM distribution in a cube of comoving length $200\,h^{-1}\mathrm{Mpc}$ colour coded according to density (white represents the peaks of DM density). Over plotted in the left plot are the quasars predicted by our semi-analytic model. The colour scales according to the optical luminosity: red represents the most luminous quasars in our model. Similarly, in the right panel we show with grey spheres galaxies with prominent radio emission. The size of the spheres is proportional to the radio luminosity the central BH produces.

sample of 66 low-redshift QSOs and radio galaxies (see also Yates et al. 1989). However, we find an excellent agreement with the more recent measurements of the correlation function of radio galaxies and quasars in the SDSS by Donoso et al. (2010).

To further elucidate the physical meaning of $\xi_{\rm q}$, $\xi_{\rm rg}$ and $\xi_{\rm dm}$, we show in Fig. 5.2 the quasars and radio galaxies in the samples we have used for calculating $\xi_{\rm q}$, $\xi_{\rm rg}$ as they distributed in the Millennium simulation (left and right plot respectively). As illustrated by the figure, quasars are more faithful tracer of the DM than radio galaxies since they closely follow the morphology of structures on different scales. On the other hand, radio galaxies appear to follow the location of the DM density peaks and therefore we expect

them to be hosted by the most massive haloes in the simulation.

The most massive haloes are the typical host of powerful radio galaxies in our model, for the following reason. In the model, a galaxy becomes a prominent radio source when its central BH has a high spin and experiences accretion in the ADAF regime. Under these circumstances, the BH can support the formation of a strong radio jet. High BH masses further contribute to the enhancement of the jet strength. These prerequisites are often fulfilled for giant ellipticals. These galaxies host the most massive and rapidly rotating BHs in our model with very low gas accretion rates (since they inhabit haloes in the quasi-hydrostatic regime). Therefore, these galaxies are the ideal candidates to be powerful radio galaxies. Since more massive haloes are approximately expected to host more massive galaxies (Kim et al. 2009) our model predicts that radio galaxies are likely to be found in the most massive DM haloes.

5.3 The evolution of the quasar two-point correlation function

In Fig. 5.3 we show the evolution with redshift of the quasar two-point correlation function, $\xi_{\rm q}$ (solid blue line). We calculate $\xi_{\rm q}$ in redshift bins similar to those for which the 2dF and 2SLAQ+SDSS LFs are estimated (see Chapter 3). In the same plot we also show the evolution of the dark matter correlation function, $\xi_{\rm dm}$ (solid black lines) and for reference we reproduce the $z \simeq 0.5$ $\xi_{\rm q}$ and $\xi_{\rm dm}$ in all panels (dashed-dotted black and dashed grey lines respectively). As shown in Fig. 5.3, at almost all redshifts the difference between $\xi_{\rm q}$ and $\xi_{\rm dm}$ lies mainly in the normalisation (except on very small scales), with the quasar bias increasing with increasing redshift. As far as the evolution of $\xi_{\rm q}$ is concerned, we find that in the redshift range $0.41 < z < 2.64$ it is basically the one-halo term that evolves. This is mainly because the number of quasars in a given halo changes significantly with redshift, an effect ascribed the change in typical mass of haloes which host quasars.

The two-point correlation can be fit by a power law of the form,

$$\xi_{\rm q}(r) = \left(\frac{r}{r_0}\right)^{-\gamma}, \tag{5.3}$$

where γ is the power law slope and r_0 is the correlation length. The correlation length

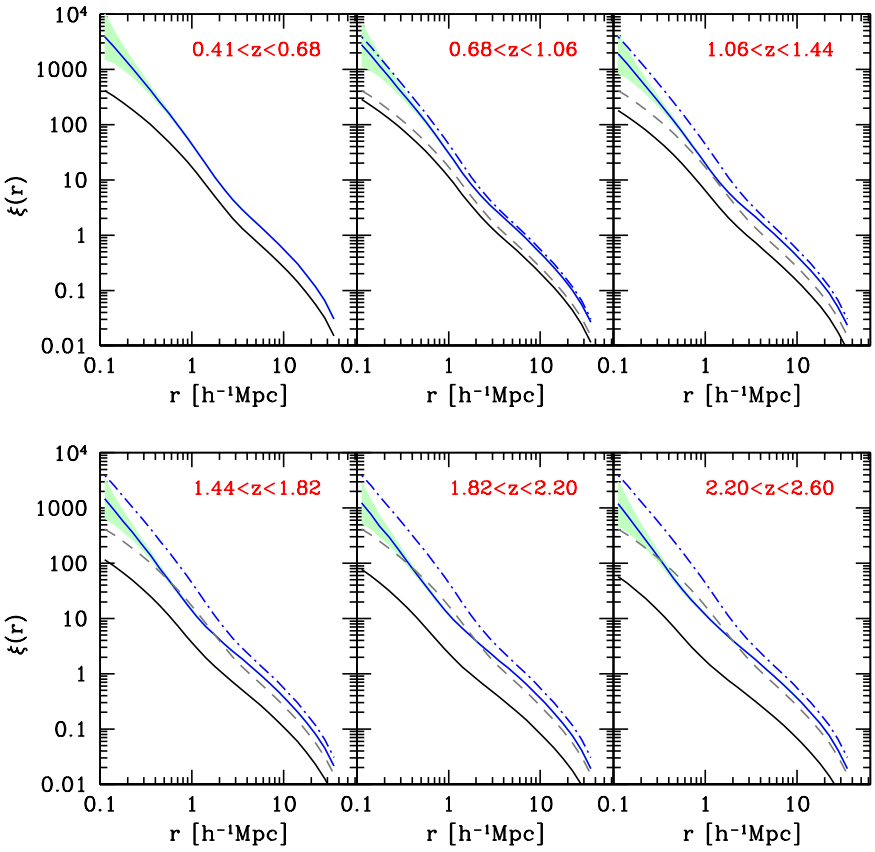

Figure 5.3: The evolution with redshift of the two-point correlation function of quasars (blue solid lines). Also shown is the evolution of the DM correlation function (solid black line). In addition, we show for reference in every redshift panel the amplitude of $\xi_{\rm q}$ and $\xi_{\rm dm}$ at $z \simeq 0.5$ (dashed-dotted black and dashed grey lines respectively).

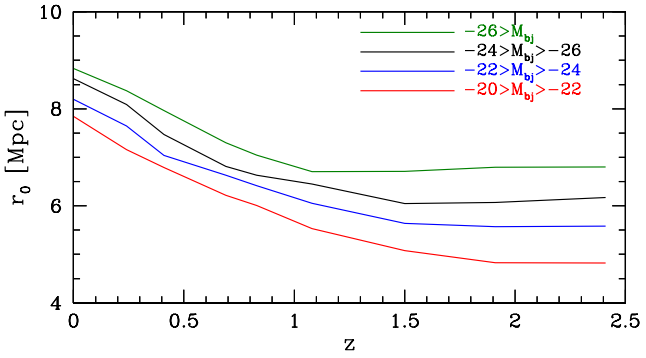

Figure 5.4: The evolution with redshift of the quasar correlation length, r_0, for four quasar magnitude bins as indicated by the label.

determines the scale at which $\xi_{\rm q}(r)$ is unity and is of particular interest since it helps to quantify the evolution of $\xi_{\rm q}(r)$ with redshift. Typical observational values of the power–law slope and correlation length for quasars are $\gamma = 1.5 - 2$ and $r_0 = 5 - 6\,h^{-1}$ Mpc.

To characterise the predicted evolution of $\xi_{\rm q}$ we fit the power law of Eq. 5.3 over the range $1 < r < 10\,h^{-1}$ Mpc assuming a fixed slope $\gamma = 1.8$ at all redshifts (Davis & Peebles 1983). In order to reveal a possible dependence of the two-point correlation function on luminosity, we split our quasar catalogues to four magnitude bins in the range $-20 > M_{b_{\rm J}} > -30$. We then fit Eq. 5.3 to the two-point correlation function obtained for each luminosity sample. Our predictions for the evolution of r_0 with redshift for the four magnitude bins are shown in Fig. 5.4. In all magnitude bins we find that in the redshift range $0 < z < 1$ the value of r_0 decreases with increasing redshift. Hence, quasars were less clustered in the past. In the same redshift range we also find a weak dependence of the clustering on quasar luminosity. Bright quasars tend to be somewhat more clustered than their faint counterparts. At higher redshifts, the value of r_0 remains approximately constant. However, the dependence of r_0 on the luminosity is now stronger. Since the amplitude of the clustering gives an indication of the DM environments quasars inhabit our predictions suggest that at high redshifts bright quasars should be found in more massive halos than those occupied by faint quasars.

To gain further insight into the clustering of quasars relative to that of the underlying

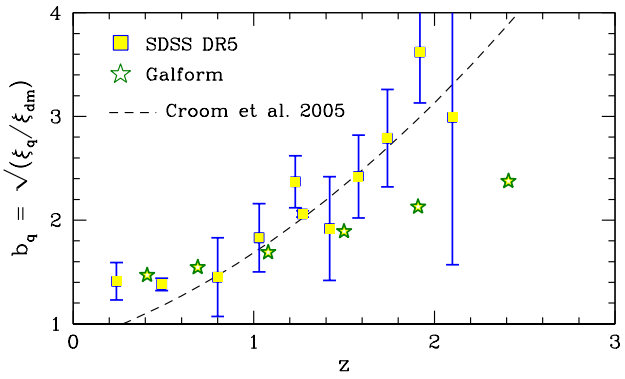

Figure 5.5: The evolution of the bias parameter, $b_{\rm b}$, with redshift (green filled star). Also shown with blue-filled rectangles is the observational estimation of $b_{\rm b}$ from the SDSS Data Release 5 quasar sample (DR5, Ross et al. 2009). In addition, we show the empirical model fit from Croom et al. (2005) to the 2dF QSO bias (dashed-black line).

DM, we plot the evolution of the bias parameter $b_{\rm q}(z)$ with redshift in Fig. 5.2. At a given redshift, $b_{\rm q}(z)$ is determined by calculating the average value of $b_{\rm q}(r)$ from Eq. 5.2 over the range $1 < r < 50\,h^{-1}$ Mpc. We do not include smaller scales in order to avoid scale dependence in bias. It is evident that the bias increases with redshift. Such evolution is also supported by recent observational estimates of b from big quasar surveys (2dF and SDSS, Croom et al. 2005; da Ângela et al. 2008; Ross et al. 2009). At $z \simeq 0.5$ we find that the amplitude of $\xi_{\rm q}$ is ~ 2 times higher than the amplitude of $\xi_{\rm dm}$. At $z \simeq 2.5$ the difference in amplitude raises up to a factor of ~ 5.5. The increase of $b_{\rm q}$ with increasing redshift suggests that quasars where more clustered relative the the overall DM in the past.

5.4 The $L_{\rm bol} - M_{\rm halo}$ relation for quasars

Finally, we explore the correlation between quasar bolometric luminosity and host halo mass. We show in Fig. 5.6 the median of the $L_{\rm bol} - M_{\rm halo}$ distribution (solid black lines) and its associated percentiles (indicated by the colour bar) at $z = 0.5, 1$ and 2. Fig. 5.6

reveals a very interesting correlation between halo mass and quasar luminosity. At high redshifts ($z = 2$), we find that $L_{\rm bol}$ and $M_{\rm halo}$ are strongly correlated. More massive haloes host in principle more luminous quasars. Such a correlation is implied also by the strong dependance of the correlation length on the quasar luminosity at high redshifts seen in Fig. 5.4. Another interesting prediction of the model is that the slope of the median of the $L_{\rm bol} - M_{\rm halo}$ correlation flattens significantly for luminosities greater than $10^{46}\,{\rm erg\,s^{-1}}$. At lower redshifts, the $L_{\rm bol} - M_{\rm halo}$ correlations shows a similar behaviour. However, the flattening above $10^{46}\,{\rm erg\,s^{-1}}$ is now more evident. For the same luminosities, we also find a much wider spread in the data.

When comparing the typical masses of haloes which quasars inhabit with the masses of the biggest haloes in our simulation (at $z = 0.5, 1$ and 2 these are $M_{\rm Halo} = 2.49 \times 10^{15}, 1.2 \times 10^{15}$ and 1.1×10^{14} ${\rm M_\odot}$ respectively) we find that quasar activity usually takes place in low and intermediate mass haloes. The most massive haloes usually host gas-poor galactic systems because AGN feedback suppresses the cooling flows that provide gas to the central galaxy. Therefore, we do not find luminous quasars in these environments. Our predictions for the typical host halo mass of quasars agree very well with recent observational estimates. Ross et al. (2009) find that the $0.3 < z < 2.2$ quasars in the SDSS inhabit DM haloes of constant mass $M_{\rm Halo} \sim 3 \times 10^{12}$ ${\rm M_\odot}$. A similar mass is found by da Ângela et al. (2008) in the 2SLAQ quasar sample. At $z \leq 1$, our model suggest a similar typical halo mass of $1 - 5 \times 10^{12}$ ${\rm M_\odot}$ in which quasars with luminosities greater than $10^{45}\,{\rm erg\,s^{-1}}$ are found. The constant quasar halo mass arises from the flattening due to AGN feedback of the $L_{\rm bol} - M_{\rm halo}$ correlation at intermediate and high luminosities.

5.5 Conclusions

In this chapter we have demonstrated the different environmental dependence of quasars and radio galaxies. Fig. 5.4 clearly shows that quasars become more clustered with decreasing redshift. In addition, the important evolution that the bias parameter undergoes in Fig. 5.5 hints that the relative clustering of quasars and DM changes over time and becomes almost identical at very low redshifts. The clustering of quasars is driven by two

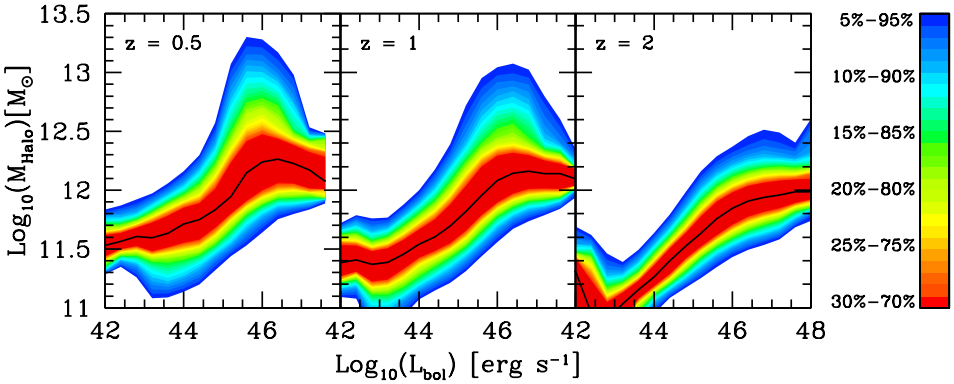

Figure 5.6: The median of the $L_{\rm bol} - M_{\rm halo}$ correlation at $z = 0.5, 1$ and 2 for the quasar sample considered in this chapter (solid black lines). We also show the associated percentiles as indicated by the colour bar on the right.

things: the clustering of the underlying DM and the distribution of gas rich starbursts between DM haloes. The triggering of starbursts due to discs becoming dynamically unstable or mergers between galaxies determines which haloes host quasars activity. The gaseous content of the disc depends upon the star formation timescale and the rate at which gas is cooling, which could be suppressed by AGN feedback. The evolution of $\xi_{\rm dm}$ is a consequence of the hierarchical nature of DM. DM structures continuously merge with each other and therefore become more clustered. Since the two-point correlation function of quasars remains almost constant on scales greater than $\sim 3\,h^{-1}$ Mpc, we conclude that the evolution of the two-point correlation function of quasars reflects the complex non-linear dynamics of DM on small scales.

The evolution of the dependence of r_0 on luminosity is driven by the physical process of galaxy formation. At high redshifts we find an obvious dependence on luminosity which translates to a well defined $L_{\rm bol} - M_{\rm halo}$ correlation. At low redshifts the luminosity dependence is more modest (although a correlation still exists). For these redshifts we find a complex $L_{\rm bol} - M_{\rm halo}$ correlation. AGN feedback strongly suppresses quasar activity in haloes more massive than 10^{13} M$_\odot$. Hence, all quasars are contained in $\lesssim 10^{13}$ M$_\odot$

haloes. However, the $L_{\rm bol} - M_{\rm halo}$ correlation has a significant spread. For example, a halo of 10^{12} $\rm M_{\odot}$ can host a quasar with luminosity in the range $10^{44} - 10^{48}\,\rm erg\,s^{-1}$. As a consequence, the two-point correlation function shows a weak dependence on luminosity.

Although massive haloes do not usually host luminous quasars, they constitute the typical environments in which radio galaxies are found. As we explained earlier in this chapter, powerful galaxies live in the most massive haloes and therefore trace the peaks of the DM distribution. The strong radio output of these galaxies is attributed to the synergy between low mass accretion rates, high BH masses and spins and AGN feedback. These three properties characterise in our model massive red elliptical galaxies (Gonzalez-Perez et al., 2009). This is also supported by observations indicating that radio galaxies are associated to giant ellipticals sitting at the centres of the most massive haloes in the universe (Wake et al., 2008; Donoso et al., 2009).

Chapter 6 | *Epilogue*

6.1 Summary-Conclusions

In this thesis we have used the GALFORM semi-analytical galaxy formation code to study the importance of BH spin in a cosmological context. GALFORM simulates the formation and evolution of galaxies and BHs in a hierarchical cosmology by modelling a wide range of physical processes, including gas cooling, AGN heating, SF and supernovae (SN) feedback, chemical evolution, and galaxy mergers. The model has been extensively tested against a large range of observations of the galaxy population. For the purposes of this analysis we have modified the code to follow the evolution of BH spin. Using GALFORM we calculate the growth of BHs by accretion and mergers, their acquisition of spin and their mass accretion rates. We also incorporate several accretion and jet-launching models from the literature, which allows us to perform a quantitative comparison with observations of AGN. Our predictions match very well the evolution of AGN and their optical-radio properties in the local Universe. This validation against the available observations, along with the success of the underlying galaxy formation model, gives us confidence in the predictions of the model for the growth of BHs in the early universe and the clustering properties of AGN.

In Chapter 2 we explain how we calculate the growth of the mass and spin of BHs through the accretion of hot gas from the halo (hot-halo mode) and cold gas from the galactic disc and mergers (starburst mode). Most BHs grow primarily by gas accretion, except the most massive ones which form late and increase their mass substantially by merging with other BHs. A BH is spun up to approximately the maximal value when it accretes its own mass from a flow at constant angular momentum.

We present the resulting distributions of BH mass, gas accretion rate and spin. We consider two possible modes of accretion. In the prolonged accretion case, the gas is accreted in a single episode. Even minor mergers trigger gas flows onto the nucleus that often deposit a mass greater than the mass of the recipient BH. Thus, most BHs are typically spun up to the maximal value. This model predicts radio properties that do not reproduce the observed luminosity function. We also consider a chaotic accretion case in which the accretion episodes are limited by the self-gravity of the disc. Gas flows onto the nucleus give rise to a series of accretion episodes each typically augmenting the BH mass by a small factor. Successive accretion events are uncorrelated, resulting in low spins for the relatively low mass BHs which grow primarily by accretion. On the other hand, the most massive holes, which build up substantial mass through BH-BH mergers, are spun up to high (but not maximal) spin values. We also show that on adopting this accretion model, the optical luminosity from disc-accreting objects matches the observed quasar luminosity function reasonably well.

We then incorporate an explicit BZ model for the jet power (Meier 2002) and use this to predict the radio luminosity function which, in the chaotic accretion case, agrees well with observations. On the basis of our derived optical and radio luminosity distributions, we propose, a grand unification of AGN activity, in which the accretion flow and jet luminosity are related to AGN type through their mass, spin and mass accretion rate. Fundamentally, our calculation shows, for the first time, how the coeval growth of BHs and their host galaxies result in optical and radio properties that explain the AGN activity seen in the local Universe.

In Chapter 3, we present our predictions for the evolution of AGN. We use an updated version of the model described in Chapter 2 that incorporates an improved SF law, as implemented by Lagos et al. (2010). By taking into account AGN obscuration, we obtain a very good fit to the observed luminosity functions of AGN (optical, soft and hard X-ray, and bolometric) for a wide range of redshifts ($0 < z < 6$). The model predicts a hierarchical build up of BH mass, with the typical mass of actively growing BHs increasing with decreasing redshift. Remarkably, despite this, we find downsizing in the AGN population, in terms of the differential growth with redshift of the space density

of faint and bright AGN. This arises naturally from the interplay between the starburst and hot-halo accretion modes. The faint end of the LF is dominated by massive BHs experiencing quiescent accretion via a thick disc, primarily during the hot-halo mode. The bright end of the LF, on the other hand, is dominated by AGN which host BHs accreting close to or in excess of the Eddington limit during the starburst mode.

In addition, our model suggests that a significant fraction of AGN are obscured in the optical and soft X-rays. In fact, we find that $\sim 90\%$ of the total number of AGN in the $z = 0.015 - 4.8$ universe are not visible in soft X rays. The implications of the obscuration are further revealed when we study the cosmological evolution of AGN of different luminosity populations. The model predicts that the comoving space density of AGN peaks at $z \simeq 3$, similar to the star formation history. However, when taking into account obscuration, the space density of faint AGN peaks at lower redshift ($z \lesssim 2$) than that of bright AGN ($z \simeq 2 - 3$). This implies that the cosmic evolution of AGN is shaped in part by obscuration.

In Chapter 4 we present predictions for the early evolution of BHs and associated AGN ($6 < z < 20$). We find that SMBHs at the centres of the first galaxies undergo huge growth spurts when the hosts experience disc instabilities. As a result of the prodigious accretion of gas the first 10^8 $\mathrm{M}_\odot$ BHs appear already at $z = 14$. Despite the early appearance of the 10^8 $\mathrm{M}_\odot$ BHs, the build up of more massive BHs is delayed because of the AGN feedback. Consequently, BHs reach masses of 10^9 $\mathrm{M}_\odot$ only at $z \simeq 6 - 7$.

Our model predicts that the first quasars with bolometric luminosities of $10^{46}\,\mathrm{erg\,s^{-1}}$ appear at $z = 14$. These quasars inhabit the most massive DM haloes in our simulation, however, with a significantly low sampling. In contrast less luminous quasars populate intermediate and low mass halos with a constant sampling of ~ 0.15. Finally, we predict that the James Webb Space Telescope should be able to detect luminous quasars up to $z = 12$.

Finally, in Chapter 5 we explore the dependance of AGN activity and luminosity on environment. We calculate and compare the two-point correlation function of quasars and radio galaxies. We find that radio galaxies are more clustered than quasars especially on small scales. The model shows that quasars trace the distribution of DM with a bias

that increases with increasing redshift. Quasars inhabit haloes with typical mass of $10^{12}-10^{13}$ $\mathrm{M}_{\odot}$ at low redshifts ($z < 2$). Our model suggests that in more massive haloes AGN feedback strongly suppresses quasar activity due to the suppressing of cooling and the subsequent drop in the reservoir of cold gas. In contrast, such haloes represent typical environments for powerful radio galaxies. This is due to the prediction of our model that in massive haloes we find galaxies with massive, rapidly rotating BHs with low gas accretion rates. As we showed in Chapter 2, these are the necessary conditions for a galaxy to be radio loud.

This thesis explicitly demonstrates that hierarchical cosmological models for galaxy formation and evolution are able to provide a robust framework in which AGN can be studied. The ability of our galaxy formation model to reproduce the observed LF of AGN in radio, optical and X-ray bands, along with the bolometric LF and account for the diversity of the AGN populations at low redshifts strengthens the powerful capabilities of semi-analytic modelling and shows that the level of AGN activity implied by AGN feedback is compatible with observations.

6.2 Future directions

In a forthcoming study we aim to provide a more thorough analysis of the clustering of quasars. We will study the evolution of the two-point correlation function of quasars and compare our predictions with SDSS and 2dF data. We will also study the effects of obscuration in the clustering of AGN and provide predictions for the halo occupation distribution of quasars and radio galaxies.

Moreover, despite the fact that our model accounts for the radio properties of AGN at low redshifts, it fails to reproduce their evolution with cosmic time. Radio-loud AGN undergo significant cosmic evolution in the redshift range $0 < z < 0.7$. Over this interval, the comoving number density of the most radio-loud AGN increases by a factor of ~ 10 more than that of the radio-quiet AGN. The strongest evolution of galaxies that host radio-loud AGN may be triggered by two distinct fuelling mechanisms that cause radio galaxies to evolve in different ways (Tasse et al. 2008; Donoso et al. 2009). Reproducing

the correct evolution of radio galaxies is a *critical* test for galaxy formation models. In a future work, will study this hypothesis by exploring the impact of the different accretion channels (starburst and hot halo) on the evolution of radio galaxies.

In addition, we aim to extend the model's predictive power to cover a wider range of outstanding astrophysical phenomena and provide accurate predictions for the gravitational wave radiation emitted by SMBHs binaries formed during galaxy mergers, which will play an essential role in the interpretation of forthcoming data from pulsar timing array experiments.

Gravitational waves are fluctuations in the curvature of spacetime which propagate as a wave, traveling outwards from the source. Direct detection of gravitational waves is the goal of several pioneering experiments (such as LISA and LIGO) and is expected to revolutionise the way astronomy is done. A stochastic background of gravitational waves is expected to arise from the superposition of a large number of unresolved gravitational–wave sources of astrophysical and cosmological origin. For instance, binaries of very massive SMBHs form when galaxies merge and emit low frequency gravitational waves that contribute to a diffuse background. The generated background depends on the assembly scenario and the dynamical processes that determine the formation of massive SMBH binaries. Hence, the ΛCDM cosmology must predict a unique gravitational wave background.

Our model is a unique tool for studying the gravitational waves emitted by SMBH binaries since it can calculate their properties and evolution within a successful cosmological model, and therefore provide the most accurate calculation of the gravitational-wave background available. Direct detection of the background may be possible through observations of pulsars since current pulsar timing array experiments have the potential to detect low-frequency gravitational wave signals within a decade (Hobbs et al. 2009). Comparison of these predictions with a potential observation of the stochastic gravitational background will provide constraints on the mass assembly of the SMBH mass in the ΛCDM universe.

Appendix A | *Introducing rotating BHs*

The most general spacetime geometry of astrophysical relevance in General Relativity is the Kerr metric. The Kerr metric is a stationary and axially symmetric solution to the vacuum Einstein field equations which describes a collapsed object of mass $M_{\rm BH}$ and angular momentum $J_{\rm BH}$. The Kerr solution has two free parameters, the geometrized mass m and the specific angular momentum or *spin parameter* a, related to $M_{\rm BH}$ and $J_{\rm BH}$ by $m = GM_{\rm BH}/c^2$ and $a = cJ_{\rm BH}/GM_{\rm BH}^2$. The linear element of the Kerr metric in Boyer-Lindquist oblate spheroidal coordinates $(r, t, \vartheta, \varphi)$ is written as

$$\begin{aligned} ds^2 = &-\left(1 - \frac{2mr}{\varrho^2}\right) dt^2 - \frac{4mFar\sin^2\vartheta}{\varrho^2} d\varphi dt + \frac{\varrho^2}{\Delta} dr^2 \\ &+\varrho^2 d\vartheta^2 + \left(r^2 + a^2 + \frac{2mra^2\sin^2\vartheta}{\varrho^2}\right)\sin^2\vartheta d\varphi^2, \end{aligned} \tag{A.1}$$

where

$$\varrho(r,\vartheta)^2 = r^2 + a^2\cos^2\vartheta, \quad \Delta(r) = r^2 - 2mr + a^2. \tag{A.2}$$

We assume that $0 \leq a \leq 1$ and in the extreme case where the BH has zero angular momentum ($a = 0$), the metric (A.1) reduces to the Schwarzschild metric[1]

$$\begin{aligned} ds^2 = &-\left(1 - \frac{2m}{r}\right) dt^2 + \left(1 - \frac{2m}{r}\right)^{-1} dr^2 \\ &+r^2 d\vartheta^2 + r^2\sin^2\vartheta d\varphi^2. \end{aligned} \tag{A.3}$$

The quantity $R_{\rm Schw} = 2m = 2GM_{\rm BH}/c^2$ defines the *Schwarzschild radius* (or *gravitational radius*) of the BH, a characteristic radius associated with every spherical mass distribution m.

[1]The case $a > 1$ describes a naked singularity and is considered as unphysical.

One can easily show that the Kerr metric is singular at $\varrho = 0$, which happens when $r = 0$ and $\vartheta = \pi/2$. The Kerr singularity is a generalisation of the Schwarzschild curvature singularity and its nature is best seen in Kerr-Schild coordinates $(\tilde{t}, x, y, z)$, where it is found to represent a "ring" with zero thickness but non-zero radius. A further singularity, however a coordinate one, is found at $\Delta = 0$. Assuming $a < m$, the quantity Δ vanishes at

$$r_{\pm} = m \pm \sqrt{m^2 - a^2}. \tag{A.4}$$

The surface $r = r_+$ is a stationary, axisymmetric 3-surface in the Kerr spacetime, which actually represents the event horizon of the Kerr BH. This event horizon is equivalent to the $r = 2m$ event horizon of the Schwarzschild BH.

The region between $r = r_+$ and $r = \infty$ is called *domain of outer communication* and is of great astrophysical interest. Orbits of test particles in the domain of outer communication are remarkable as a rotating BH is expected to influence the surrounding matter directly through its rotation. Following the analysis developed in Chandrasekhar (1983), we consider a freely falling particle in the $\vartheta = \pi/2$ plane with a zero ϑ-component velocity ($\dot{\vartheta} = 0$). The particle is constrained to orbit in the equatorial plane of the BH, governed by the metric

$$ds^2 = -\left(1 - \frac{2m}{r}\right) dt^2 - \frac{4am}{r} dt d\varphi + \frac{r^2}{\Delta} dr^2 + \left(r^2 + a^2 + \frac{2ma^2}{r}\right) d\varphi^2. \tag{A.5}$$

The assumption of equatorial orbits simplifies significantly the complex behaviour of freely falling particles in the hole's exterior, since the axisymmetry of the spacetime does not guarantee that the orbits will be confined in some plane.

Given the line element (A.5), it is straightforward to obtain the Lagrangian, which reads

$$2L = -\left(1 - \frac{2m}{r}\right) \dot{t}^2 - \frac{4am}{r} \dot{t}\dot{\varphi} + \frac{r^2}{\Delta} \dot{r}^2 + \left(r^2 + a^2 + \frac{2ma^2}{r}\right) \dot{\varphi}^2. \tag{A.6}$$

Here the time derivatives are with respect to an affine parameter τ. Once the Lagrangian is known, one can derive the equations governing the energy and angular momentum

of the particle from the integrals of motion[2]

$$p_t \equiv \frac{\partial L}{\partial \dot{t}} = \text{constant} = -e \tag{A.7}$$

$$p_\varphi \equiv \frac{\partial L}{\partial \dot{\varphi}} = \text{constant} = l \tag{A.8}$$

$$L = -\frac{m^2}{2} \Rightarrow r^3 \left(\frac{dr}{d\tau}\right)^2 = V_{\text{eff}}(e, l, r), \tag{A.9}$$

where V_{eff} represents the effective potential governing radial orbits on the equatorial plane

$$V_{\text{eff}} = -r^3 e^2 + 2m(ae - l)^2 + r(a^2 e^2 - l^2 - m^2 \Delta). \tag{A.10}$$

Note here that the sign of l determines the type of orbit in the equatorial plane; positive values of l represent orbits that go with the rotation of the BH, whereas negative values represent orbits going against it. We refer to these orbits as co-rotating and counter-rotating respectively. The existence of orbits with negative angular momentum is a general property of the Kerr spacetime closely related to the fact that rotating bodies in relativity drag the spacetime around themselves a phenomenon knows as frame-dragging or Lense-Thirring effect (Lense-Thirring 1918).

Bound circular orbits occur when $dr/d\tau = 0$, which requires

$$V_{\text{eff}} = 0, \quad \frac{\partial V_{\text{eff}}}{\partial r} = 0 \tag{A.11}$$

to be satisfied simultaneously. These conditions determine the values of e, ℓ allowed for stable circular orbits in the Kerr geometry and once solved together with the integrals of motion they give the specific energy and angular momentum of the particle

$$\tilde{e} = e/m = \frac{r^2 - 2mr \pm a\sqrt{mr}}{r(r^2 - 3mr \pm 2a\sqrt{mr})^{1/2}} \tag{A.12}$$

$$\tilde{\ell} = \ell/m^2 = \pm \frac{\sqrt{mr}(r^2 \mp 2a\sqrt{mr} + a^2)}{r(r^2 - 3mr \pm 2a\sqrt{mr})^{1/2}}. \tag{A.13}$$

[2]The integrals of motion are derived from the condition $p_\beta p^\beta = -1$, where $p^\beta = dx^\beta/d\tau$ is the momentum per unit mass four-vector of the particle (β is the index representation of the coordinate set).

Here the upper sign refers to co-rotating orbits and the lower sign to counter-rotating orbits. The stability of the orbits characterised by e and l in Eqs (A.12), (A.13) is ensured if the effective potential is a minimum, i.e

$$\frac{\partial^2 V_{\rm eff}}{\partial r^2} \leq 0. \tag{A.14}$$

A straightforward calculation of (A.14) gives

$$1 - \tilde{e}^2 \geq \frac{2}{3}\frac{m}{r}. \tag{A.15}$$

The equality holds for the *last stable orbit* (LSO), $r_{\rm lso}$, given by (Bardeen et al. 1972)

$$r_{\rm lso} = m\{3 + Z_2 \mp [(3 - Z_1)(3 + Z_1 + 2Z_2)]^{1/2}\}, \tag{A.16}$$

with

$$\begin{aligned} Z_1 &\equiv 1 + \left(1 - \frac{a^2}{m^2}\right)^{1/3}\left[\left(1 + \frac{a}{m}\right)^{1/3} + \left(1 - \frac{a}{m}\right)^{1/3}\right] \\ Z_2 &\equiv \left(3\frac{a^2}{m^2} + Z_1^2\right)^{1/2}. \end{aligned} \tag{A.17}$$

The stability criterion for bound circular orbits is now written as

$$r \geqslant r_{\rm lso}. \tag{A.18}$$

Figure 2.1 demonstrates the innermost stable circular orbit in the equatorial plane around a BH of mass $M_{\rm bh} = c^2 m/G$, as function of the hole's specific angular momentum. For $a = 0$, $r_{\rm lso} = 6m$; for $a = m$, $r_{\rm lso} = m$ (co-rotating orbits) or $r_{\rm lso} = 9m$ (counter-rotating orbits).

A property evidently important for astrophysics is the binding energy of the particle at the LSO. The binding energy can be defined as the difference between the rest energy of the particle at infinity and the energy at the LSO as measured by an observer at infinity. Since $\tilde{e}$ expresses the energy per unit rest mass, we can define the binding energy as $1-\tilde{e}$. Condition (A.15), when the equality holds, provides a simple relation for the binding energy at the LSO,

$$1 - \tilde{e} = 1 - \sqrt{1 - \frac{2}{3}\frac{m}{r_{\rm lso}}}, \tag{A.19}$$

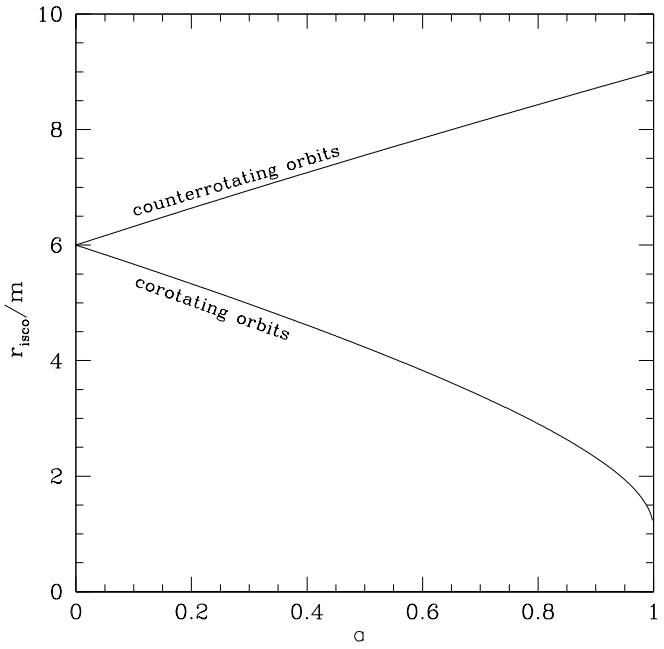

Figure A.1: Radii of the innermost stable circular orbit around a rotating BH, as function of the spin parameter a, for counter-rotating and co-rotating orbits.

which expresses the fraction of energy released by matter spiralling in towards the BH through a succession of almost circular orbits. Graphically depicted, see Figure 2.2, expression (A.19) shows that accretion of matter into slowly rotating BHs has moderate efficiency for both counter- and co-rotating matter.

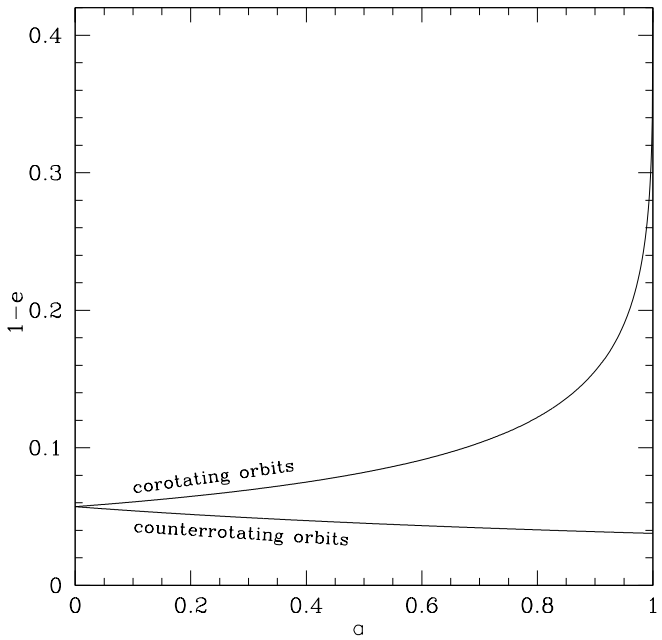

Figure A.2: The binding energy per unit rest mass $1 - \tilde{e}$ at the LSO as function of the spin parameter a, for counter-rotating and co-rotating orbits in the equatorial plane of the Kerr BH.

Bibliography

M. A. Abramowicz, X. Chen, S. Kato, J.-P. Lasota, and O. Regev. *ApJ*, 438:L37–L39, January 1995.

J. Aird, K. Nandra, E. S. Laird, A. Georgakakis, M. L. N. Ashby, P. Barmby, A. L. Coil, J.-S. Huang, A. M. Koekemoer, C. C. Steidel, and C. N. A. Willmer. *MNRAS*, 401: 2531–2551, February 2010.

D. M. Alexander, F. E. Bauer, W. N. Brandt, D. P. Schneider, A. E. Hornschemeier, C. Vignali, A. J. Barger, P. S. Broos, L. L. Cowie, G. P. Garmire, L. K. Townsley, M. W. Bautz, G. Chartas, and W. L. W. Sargent. *AJ*, 126:539–574, August 2003.

D. M. Alexander, G. Chartas, F. E. Bauer, W. N. Brandt, C. Simpson, and C. Vignali. *MNRAS*, 357:L16–L20, February 2005.

D. M. Alexander, R.-R. Chary, A. Pope, F. E. Bauer, W. N. Brandt, E. Daddi, M. Dickinson, D. Elbaz, and N. A. Reddy. *ApJ*, 687:835–847, November 2008.

R. Antonucci. *ARA&A*, 31:473–521, 1993.

A. Babić, L. Miller, M. J. Jarvis, T. J. Turner, D. M. Alexander, and S. M. Croom. A&A, 474:755–762, November 2007.

J. G. Baker, S. T. McWilliams, J. R. van Meter, J. Centrella, D.-I. Choi, B. J. Kelly, and M. Koppitz. *PhRvD*, 75(12):124024–+, June 2007.

D. R. Ballantyne, J. E. Everett, and N. Murray. *ApJ*, 639:740–752, March 2006a.

D. R. Ballantyne, Y. Shi, G. H. Rieke, J. L. Donley, C. Papovich, and J. R. Rigby. *ApJ*, 653: 1070–1088, December 2006b.

X. Barcons, F. J. Carrera, M. T. Ceballos, M. J. Page, J. Bussons-Gordo, A. Corral, J. Ebrero, S. Mateos, J. A. Tedds, M. G. Watson, D. Baskill, M. Birkinshaw, T. Boller, N. Borisov, M. Bremer, G. E. Bromage, H. Brunner, A. Caccianiga, C. S. Crawford, M. S. Cropper, R. Della Ceca, P. Derry, A. C. Fabian, P. Guillout, Y. Hashimoto, G. Hasinger, B. J. M. Hassall, G. Lamer, N. S. Loaring, T. Maccacaro, K. O. Mason, R. G. McMahon, L. Mirioni, J. P. D. Mittaz, C. Motch, I. Negueruela, J. P. Osborne, F. Panessa, I. Pérez-Fournon, J. P. Pye, T. P. Roberts, S. Rosen, N. Schartel, N. Schurch, A. Schwope, P. Severgnini, R. Sharp, G. C. Stewart, G. Szokoly, A. Ullán, M. J. Ward, R. S. Warwick, P. J. Wheatley, N. A. Webb, D. Worrall, W. Yuan, and H. Ziaeepour. A&A, 476:1191–1203, December 2007.

A. J. Barger, L. L. Cowie, R. F. Mushotzky, Y. Yang, W.-H. Wang, A. T. Steffen, and P. Capak. *AJ*, 129:578–609, February 2005.

C. M. Baugh, C. G. Lacey, C. S. Frenk, G. L. Granato, L. Silva, A. Bressan, A. J. Benson, and S. Cole. *MNRAS*, 356:1191–1200, January 2005.

M. C. Begelman, R. D. Blandford, and M. J. Rees. *Reviews of Modern Physics*, 56:255–351, April 1984.

M. C. Begelman, M. Volonteri, and M. J. Rees. *MNRAS*, 370:289–298, July 2006.

M. C. Bentz, B. M. Peterson, R. W. Pogge, and M. Vestergaard. *ApJ*, 694:L166–L170, April 2009.

E. Berti and M. Volonteri. *ApJ*, 684:822–828, September 2008.

R. D. Blandford and D. G. Payne. *MNRAS*, 199:883–903, June 1982.

R. D. Blandford and R. L. Znajek. *MNRAS*, 179:433–456, May 1977.

A. Bongiorno, G. Zamorani, I. Gavignaud, B. Marano, S. Paltani, G. Mathez, P. Møller, J. P. Picat, M. Cirasuolo, F. Lamareille, D. Bottini, B. Garilli, V. Le Brun, O. Le Fèvre,

D. Maccagni, R. Scaramella, M. Scodeggio, L. Tresse, G. Vettolani, A. Zanichelli, C. Adami, S. Arnouts, S. Bardelli, M. Bolzonella, A. Cappi, S. Charlot, P. Ciliegi, T. Contini, S. Foucaud, P. Franzetti, L. Guzzo, O. Ilbert, A. Iovino, H. J. McCracken, C. Marinoni, A. Mazure, B. Meneux, R. Merighi, R. Pellò, A. Pollo, L. Pozzetti, M. Radovich, E. Zucca, E. Hatziminaoglou, M. Polletta, M. Bondi, J. Brinchmann, O. Cucciati, S. de la Torre, L. Gregorini, Y. Mellier, P. Merluzzi, S. Temporin, D. Vergani, and C. J. Walcher. A&A, 472:443–454, September 2007.

R. G. Bower, A. J. Benson, R. Malbon, J. C. Helly, C. S. Frenk, C. M. Baugh, S. Cole, and C. G. Lacey. *MNRAS*, 370:645–655, August 2006.

R. G. Bower, I. G. McCarthy, and A. J. Benson. *MNRAS*, 390:1399–1410, November 2008.

R. G. Bower, I. Vernon, M. Goldstein, A. J. Benson, C. G. Lacey, C. M. Baugh, S. Cole, and C. S. Frenk. *MNRAS*, 407:2017–2045, October 2010.

B. J. Boyle, T. Shanks, and B. A. Peterson. *MNRAS*, 235:935–948, December 1988.

B. J. Boyle, T. Shanks, S. M. Croom, R. J. Smith, L. Miller, N. Loaring, and C. Heymans. *MNRAS*, 317:1014–1022, October 2000.

W. N. Brandt and G. Hasinger. *ARA&A*, 43:827–859, September 2005.

J. M. Bromley, R. S. Somerville, and A. C. Fabian. *MNRAS*, 350:456–472, May 2004.

A. Cattaneo, J. Blaizot, D. H. Weinberg, D. Kereš, S. Colombi, R. Davé, J. Devriendt, B. Guiderdoni, and N. Katz. *MNRAS*, 377:63–76, May 2007.

S. Chandrasekhar. *The mathematical theory of black holes*. 1983.

E. Churazov, M. Gilfanov, and M. Revnivtsev. *MNRAS*, 321:759–766, March 2001.

S. Cole, A. Aragon-Salamanca, C. S. Frenk, J. F. Navarro, and S. E. Zepf. *MNRAS*, 271: 781–+, December 1994.

S. Cole, C. G. Lacey, C. M. Baugh, and C. S. Frenk. *MNRAS*, 319:168–204, November 2000.

A. Comastri. In A. J. Barger, editor, *Supermassive Black Holes in the Distant Universe*, volume 308 of *Astrophysics and Space Science Library*, pages 245–+, August 2004.

A. Comastri, G. Setti, G. Zamorani, and G. Hasinger. A&A, 296:1–+, April 1995.

L. L. Cowie, A. J. Barger, M. W. Bautz, W. N. Brandt, and G. P. Garmire. *ApJ*, 584:L57–L60, February 2003.

S. M. Croom, T. Shanks, B. J. Boyle, R. J. Smith, L. Miller, N. S. Loaring, and F. Hoyle. *MNRAS*, 325:483–496, August 2001.

S. M. Croom, R. J. Smith, B. J. Boyle, T. Shanks, L. Miller, P. J. Outram, and N. S. Loaring. *MNRAS*, 349:1397–1418, April 2004.

S. M. Croom, B. J. Boyle, T. Shanks, R. J. Smith, L. Miller, P. J. Outram, N. S. Loaring, F. Hoyle, and J. da Ângela. *MNRAS*, 356:415–438, January 2005.

S. M. Croom, G. T. Richards, T. Shanks, B. J. Boyle, R. G. Sharp, J. Bland-Hawthorn, T. Bridges, R. J. Brunner, R. Cannon, D. Carson, K. Chiu, M. Colless, W. Couch, R. de Propris, M. J. Drinkwater, A. Edge, S. Fine, J. Loveday, L. Miller, A. D. Myers, R. C. Nichol, P. Outram, K. Pimbblet, I. Roseboom, N. Ross, D. P. Schneider, A. Smith, C. Stoughton, M. A. Strauss, and D. Wake. *MNRAS*, 392:19–44, January 2009a.

S. M. Croom, G. T. Richards, T. Shanks, B. J. Boyle, M. A. Strauss, A. D. Myers, R. C. Nichol, K. A. Pimbblet, N. P. Ross, D. P. Schneider, R. G. Sharp, and D. A. Wake. *MNRAS*, 399:1755–1772, November 2009b.

D. J. Croton, V. Springel, S. D. M. White, G. De Lucia, C. S. Frenk, L. Gao, A. Jenkins, G. Kauffmann, J. F. Navarro, and N. Yoshida. *MNRAS*, 365:11–28, January 2006.

J. da Ângela, T. Shanks, S. M. Croom, P. Weilbacher, R. J. Brunner, W. J. Couch, L. Miller, A. D. Myers, R. C. Nichol, K. A. Pimbblet, R. de Propris, G. T. Richards, N. P. Ross, D. P. Schneider, and D. Wake. *MNRAS*, 383:565–580, January 2008.

C. Dalla Vecchia, R. G. Bower, T. Theuns, M. L. Balogh, P. Mazzotta, and C. S. Frenk. *MNRAS*, 355:995–1004, December 2004.

G. De Lucia, V. Springel, S. D. M. White, D. Croton, and G. Kauffmann. *MNRAS*, 366: 499–509, February 2006.

T. Di Matteo, V. Springel, and L. Hernquist. *Nat*, 433:604–607, February 2005.

C. Done and A. Kubota. *MNRAS*, 371:1216–1230, September 2006.

C. Done, M. Gierliński, and A. Kubota. A&A Rev., 15:1–66, December 2007.

E. Donoso, P. N. Best, and G. Kauffmann. *MNRAS*, 392:617–629, January 2009.

E. Donoso, C. Li, G. Kauffmann, P. N. Best, and T. M. Heckman. *MNRAS*, 407:1078–1089, September 2010.

G. Efstathiou, G. Lake, and J. Negroponte. *MNRAS*, 199:1069–1088, June 1982.

X. Fan, V. K. Narayanan, R. H. Lupton, M. A. Strauss, G. R. Knapp, R. H. Becker, R. L. White, L. Pentericci, S. K. Leggett, Z. Haiman, J. E. Gunn, Ž. Ivezić, D. P. Schneider, S. F. Anderson, J. Brinkmann, N. A. Bahcall, A. J. Connolly, I. Csabai, M. Doi, M. Fukugita, T. Geballe, E. K. Grebel, D. Harbeck, G. Hennessy, D. Q. Lamb, G. Miknaitis, J. A. Munn, R. Nichol, S. Okamura, J. R. Pier, F. Prada, G. T. Richards, A. Szalay, and D. G. York. *AJ*, 122:2833–2849, December 2001.

X. Fan, M. A. Strauss, D. P. Schneider, R. H. Becker, R. L. White, Z. Haiman, M. Gregg, L. Pentericci, E. K. Grebel, V. K. Narayanan, Y.-S. Loh, G. T. Richards, J. E. Gunn, R. H. Lupton, G. R. Knapp, Ž. Ivezić, W. N. Brandt, M. Collinge, L. Hao, D. Harbeck, F. Prada, J. Schaye, I. Strateva, N. Zakamska, S. Anderson, J. Brinkmann, N. A. Bahcall, D. Q. Lamb, S. Okamura, A. Szalay, and D. G. York. *AJ*, 125:1649–1659, April 2003.

X. Fan, J. F. Hennawi, G. T. Richards, M. A. Strauss, D. P. Schneider, J. L. Donley, J. E. Young, J. Annis, H. Lin, H. Lampeitl, R. H. Lupton, J. E. Gunn, G. R. Knapp, W. N. Brandt, S. Anderson, N. A. Bahcall, J. Brinkmann, R. J. Brunner, M. Fukugita, A. S. Szalay, G. P. Szokoly, and D. G. York. *AJ*, 128:515–522, August 2004.

N. Fanidakis, C. M. Baugh, A. J. Benson, R. G. Bower, S. Cole, C. Done, and C. S. Frenk. *MNRAS*, pages 1547–+, October 2010.

L. Ferrarese and D. Merritt. *ApJ*, 539:L9–L12, August 2000.

F. Fiore, M. Brusa, F. Cocchia, A. Baldi, N. Carangelo, P. Ciliegi, A. Comastri, F. La Franca, R. Maiolino, G. Matt, S. Molendi, M. Mignoli, G. C. Perola, P. Severgnini, and C. Vignali. A&A, 409:79–90, October 2003.

A. S. Font, R. G. Bower, I. G. McCarthy, A. J. Benson, C. S. Frenk, J. C. Helly, C. G. Lacey, C. M. Baugh, and S. Cole. *MNRAS*, 389:1619–1629, October 2008.

M. Fukugita and P. J. E. Peebles. *ApJ*, 616:643–668, December 2004.

K. Gebhardt, R. Bender, G. Bower, A. Dressler, S. M. Faber, A. V. Filippenko, R. Green, C. Grillmair, L. C. Ho, J. Kormendy, T. R. Lauer, J. Magorrian, J. Pinkney, D. Richstone, and S. Tremaine. *ApJ*, 539:L13–L16, August 2000.

I. M. George, T. J. Turner, H. Netzer, K. Nandra, R. F. Mushotzky, and T. Yaqoob. *Astrophys. J. Suppl.*, 114:73–+, January 1998.

G. Ghisellini, R. Della Ceca, M. Volonteri, G. Ghirlanda, F. Tavecchio, L. Foschini, G. Tagliaferri, F. Haardt, G. Pareschi, and J. Grindlay. *MNRAS*, 405:387–400, June 2010.

R. Giacconi, A. Zirm, J. Wang, P. Rosati, M. Nonino, P. Tozzi, R. Gilli, V. Mainieri, G. Hasinger, L. Kewley, J. Bergeron, S. Borgani, R. Gilmozzi, N. Grogin, A. Koekemoer, E. Schreier, W. Zheng, and C. Norman. *Astrophys. J. Suppl.*, 139:369–410, April 2002.

R. Gilli, G. Risaliti, and M. Salvati. A&A, 347:424–433, July 1999.

R. Gilli, A. Comastri, and G. Hasinger. A&A, 463:79–96, February 2007.

V. Gonzalez-Perez, C. M. Baugh, C. G. Lacey, and C. Almeida. *MNRAS*, 398:497–514, September 2009.

A. D. Goulding and D. M. Alexander. *MNRAS*, 398:1165–1193, September 2009.

A. D. Goulding, D. M. Alexander, J. R. Mullaney, J. M. Gelbord, R. C. Hickox, M. Ward, and M. G. Watson. *MNRAS*, pages 1757–+, November 2010.

A. W. Graham and S. P. Driver. *MNRAS*, 380:L15–L19, September 2007.

Z. Haiman. *ApJ*, 613:36–40, September 2004.

N. Häring and H.-W. Rix. *ApJ*, 604:L89–L92, April 2004.

G. Hasinger. *Nuclear Physics B Proceedings Supplements*, 132:86–96, June 2004.

G. Hasinger. A&A, 490:905–922, November 2008.

G. Hasinger, B. Altieri, M. Arnaud, X. Barcons, J. Bergeron, H. Brunner, M. Dadina, K. Dennerl, P. Ferrando, A. Finoguenov, R. E. Griffiths, Y. Hashimoto, F. A. Jansen, D. H. Lumb, K. O. Mason, S. Mateos, R. G. McMahon, T. Miyaji, F. Paerels, M. J. Page, A. F. Ptak, T. P. Sasseen, N. Schartel, G. P. Szokoly, J. Trümper, M. Turner, R. S. Warwick, and M. G. Watson. A&A, 365:L45–L50, January 2001.

G. Hasinger, T. Miyaji, and M. Schmidt. A&A, 441:417–434, October 2005.

J. F. Hawley and J. H. Krolik. *ApJ*, 641:103–116, April 2006.

T. M. Heckman, G. Kauffmann, J. Brinchmann, S. Charlot, C. Tremonti, and S. D. M. White. *ApJ*, 613:109–118, September 2004.

P. C. Hewett, C. B. Foltz, and F. H. Chaffee. *ApJ*, 406:L43–L46, April 1993.

P. F. Hopkins, L. Hernquist, T. J. Cox, T. Di Matteo, B. Robertson, and V. Springel. *ApJ*, 630:716–720, September 2005a.

P. F. Hopkins, L. Hernquist, P. Martini, T. J. Cox, B. Robertson, T. Di Matteo, and V. Springel. *ApJ*, 625:L71–L74, June 2005b.

P. F. Hopkins, L. Hernquist, T. J. Cox, B. Robertson, and V. Springel. *Astrophys. J. Suppl.*, 163:50–79, March 2006.

P. F. Hopkins, G. T. Richards, and L. Hernquist. *ApJ*, 654:731–753, January 2007.

S. Ichimaru. *ApJ*, 214:840–855, June 1977.

L. Jiang, X. Fan, D. C. Hines, Y. Shi, M. Vestergaard, F. Bertoldi, W. N. Brandt, C. L. Carilli, P. Cox, E. Le Floc'h, L. Pentericci, G. T. Richards, G. H. Rieke, D. P. Schneider, M. A. Strauss, F. Walter, and J. Brinkmann. *AJ*, 132:2127–2134, November 2006.

L. Jiang, X. Fan, F. Bian, J. Annis, K. Chiu, S. Jester, H. Lin, R. H. Lupton, G. T. Richards, M. A. Strauss, V. Malanushenko, E. Malanushenko, and D. P. Schneider. *AJ*, 138:305–311, July 2009.

L. Jiang, X. Fan, W. N. Brandt, C. L. Carilli, E. Egami, D. C. Hines, J. D. Kurk, G. T. Richards, Y. Shen, M. A. Strauss, M. Vestergaard, and F. Walter. *Nat*, 464:380–383, March 2010.

G. Kauffmann and M. Haehnelt. *MNRAS*, 311:576–588, January 2000.

B. C. Kelly, M. Vestergaard, X. Fan, P. Hopkins, L. Hernquist, and A. Siemiginowska. *ApJ*, 719:1315–1334, August 2010.

A. R. King. *MNRAS*, 402:1516–1522, March 2010.

A. R. King, S. H. Lubow, G. I. Ogilvie, and J. E. Pringle. *MNRAS*, 363:49–56, October 2005.

A. R. King, J. E. Pringle, and J. A. Hofmann. *MNRAS*, 385:1621–1627, April 2008.

S. M. Koushiappas, J. S. Bullock, and A. Dekel. *MNRAS*, 354:292–304, October 2004.

J. D. Kurk, F. Walter, X. Fan, L. Jiang, D. A. Riechers, H.-W. Rix, L. Pentericci, M. A. Strauss, C. Carilli, and S. Wagner. *ApJ*, 669:32–44, November 2007.

J. D. Kurk, F. Walter, X. Fan, L. Jiang, S. Jester, H.-W. Rix, and D. A. Riechers. *ApJ*, 702: 833–837, September 2009.

F. La Franca, F. Fiore, C. Vignali, A. Antonelli, A. Comastri, P. Giommi, G. Matt, S. Molendi, G. C. Perola, and F. Pompilio. *ApJ*, 570:100–113, May 2002.

F. La Franca, F. Fiore, A. Comastri, G. C. Perola, N. Sacchi, M. Brusa, F. Cocchia, C. Feruglio, G. Matt, C. Vignali, N. Carangelo, P. Ciliegi, A. Lamastra, R. Maiolino, M. Mignoli, S. Molendi, and S. Puccetti. *ApJ*, 635:864–879, December 2005.

C. D. P. Lagos, S. A. Cora, and N. D. Padilla. *MNRAS*, 388:587–602, August 2008.

C. D. P. Lagos, N. D. Padilla, and S. A. Cora. *MNRAS*, 395:625–636, May 2009.

C. d. P. Lagos, C. G. Lacey, C. M. Baugh, R. G. Bower, and A. J. Benson. *ArXiv e-prints*, November 2010.

Y. Li, L. Hernquist, B. Robertson, T. J. Cox, P. F. Hopkins, V. Springel, L. Gao, T. Di Matteo, A. R. Zentner, A. Jenkins, and N. Yoshida. *ApJ*, 665:187–208, August 2007.

N. I. Libeskind, S. Cole, C. S. Frenk, and J. C. Helly. *MNRAS*, 368:1381–1391, May 2006.

G. Lodato and P. Natarajan. *MNRAS*, 371:1813–1823, October 2006.

D. MacDonald and K. S. Thorne. *MNRAS*, 198:345–382, January 1982.

K. J. Mack, J. P. Ostriker, and M. Ricotti. *ApJ*, 665:1277–1287, August 2007.

J. Magorrian, S. Tremaine, D. Richstone, R. Bender, G. Bower, A. Dressler, S. M. Faber, K. Gebhardt, R. Green, C. Grillmair, J. Kormendy, and T. Lauer. *AJ*, 115:2285–2305, June 1998.

R. Mahadevan. *ApJ*, 477:585–+, March 1997.

R. K. Malbon, C. M. Baugh, C. S. Frenk, and C. G. Lacey. *MNRAS*, 382:1394–1414, December 2007.

D. Marchesini, A. Celotti, and L. Ferrarese. *MNRAS*, 351:733–744, June 2004.

A. Marconi and L. K. Hunt. *ApJ*, 589:L21–L24, May 2003.

A. Marconi, G. Risaliti, R. Gilli, L. K. Hunt, R. Maiolino, and M. Salvati. *MNRAS*, 351: 169–185, June 2004.

A. Martínez-Sansigre, S. Rawlings, M. Lacy, D. Fadda, F. R. Marleau, C. Simpson, C. J. Willott, and M. J. Jarvis. *Nat*, 436:666–669, August 2005.

I. G. McCarthy, J. Schaye, T. J. Ponman, R. G. Bower, C. M. Booth, C. Dalla Vecchia, R. A. Crain, V. Springel, T. Theuns, and R. P. C. Wiersma. *MNRAS*, 406:822–839, August 2010.

R. J. McLure and J. S. Dunlop. *MNRAS*, 331:795–804, April 2002a.

R. J. McLure and J. S. Dunlop. *MNRAS*, 331:795–804, April 2002b.

K. Menou and Z. Haiman. *ApJ*, 615:130–134, November 2004.

D. Merritt, M. Milosavljević, M. Favata, S. A. Hughes, and D. E. Holz. *ApJ*, 607:L9–L12, May 2004.

M. Milosavljević and D. Merritt. *ApJ*, 563:34–62, December 2001.

T. Miyaji, G. Hasinger, and M. Schmidt. A&A, 369:49–56, April 2001.

R. Narayan and I. Yi. *ApJ*, 428:L13–L16, June 1994.

I. D. Novikov and K. S. Thorne. In C. Dewitt & B. S. Dewitt, editor, *Black Holes (Les Astres Occlus)*, pages 343–450, 1973.

I. D. Novikov, A. G. Polnarev, A. A. Starobinskii, and I. B. Zeldovich. A&A, 80:104–109, November 1979.

H. Parkinson, S. Cole, and J. Helly. *MNRAS*, 383:557–564, January 2008.

O. H. Parry, V. R. Eke, and C. S. Frenk. *MNRAS*, 396:1972–1984, July 2009.

E. Piconcelli, E. Jimenez-Bailón, M. Guainazzi, N. Schartel, P. M. Rodríguez-Pascual, and M. Santos-Lleó. *MNRAS*, 351:161–168, June 2004.

M. J. Rees. In G. R. Riegler & R. D. Blandford, editor, *The Galactic Center*, volume 83 of *American Institute of Physics Conference Series*, pages 166–176, 1982.

M. J. Rees and J. P. Ostriker. *MNRAS*, 179:541–559, June 1977.

C. S. Reynolds. *MNRAS*, 286:513–537, April 1997.

G. T. Richards, S. M. Croom, S. F. Anderson, J. Bland-Hawthorn, B. J. Boyle, R. De Propris, M. J. Drinkwater, X. Fan, J. E. Gunn, Ž. Ivezić, S. Jester, J. Loveday, A. Meiksin, L. Miller, A. Myers, R. C. Nichol, P. J. Outram, K. A. Pimbblet, I. G. Roseboom, N. Ross, D. P. Schneider, T. Shanks, R. G. Sharp, C. Stoughton, M. A. Strauss, A. S. Szalay, D. E. Vanden Berk, and D. G. York. *MNRAS*, 360:839–852, July 2005.

G. T. Richards, M. A. Strauss, X. Fan, P. B. Hall, S. Jester, D. P. Schneider, D. E. Vanden Berk, C. Stoughton, S. F. Anderson, R. J. Brunner, J. Gray, J. E. Gunn, Ž. Ivezić, M. K. Kirkland, G. R. Knapp, J. Loveday, A. Meiksin, A. Pope, A. S. Szalay, A. R. Thakar, B. Yanny, D. G. York, J. C. Barentine, H. J. Brewington, J. Brinkmann, M. Fukugita, M. Harvanek, S. M. Kent, S. J. Kleinman, J. Krzesiński, D. C. Long, R. H. Lupton, T. Nash, E. H. Neilsen, Jr., A. Nitta, D. J. Schlegel, and S. A. Snedden. *AJ*, 131:2766–2787, June 2006.

D. Richstone, E. A. Ajhar, R. Bender, G. Bower, A. Dressler, S. M. Faber, A. V. Filippenko, K. Gebhardt, R. Green, L. C. Ho, J. Kormendy, T. R. Lauer, J. Magorrian, and S. Tremaine. *Nat*, 395:A14+, October 1998.

G. Risaliti, R. Maiolino, and M. Salvati. *ApJ*, 522:157–164, September 1999.

N. P. Ross, Y. Shen, M. A. Strauss, D. E. Vanden Berk, A. J. Connolly, G. T. Richards, D. P. Schneider, D. H. Weinberg, P. B. Hall, N. A. Bahcall, and R. J. Brunner. *ApJ*, 697: 1634–1655, June 2009.

R. Salvaterra, F. Haardt, and A. Ferrara. *MNRAS*, 362:L50–L54, September 2005.

A. G. Sánchez, C. M. Baugh, W. J. Percival, J. A. Peacock, N. D. Padilla, S. Cole, C. S. Frenk, and P. Norberg. *MNRAS*, 366:189–207, February 2006.

M. Schmidt and R. F. Green. *ApJ*, 269:352–374, June 1983.

M. Schmidt, D. P. Schneider, and J. E. Gunn. *AJ*, 110:68–+, July 1995.

J. D. Schnittman and J. H. Krolik. *ApJ*, 712:908–924, April 2010.

N. I. Shakura and R. A. Sunyaev. A&A, 24:337–355, 1973.

F. Shankar, P. Salucci, G. L. Granato, G. De Zotti, and L. Danese. *MNRAS*, 354:1020–1030, November 2004.

S. L. Shapiro. *ApJ*, 620:59–68, February 2005.

Y. Shen, M. A. Strauss, N. P. Ross, P. B. Hall, Y.-T. Lin, G. T. Richards, D. P. Schneider, D. H. Weinberg, A. J. Connolly, X. Fan, J. F. Hennawi, F. Shankar, D. E. Vanden Berk, N. A. Bahcall, and R. J. Brunner. *ApJ*, 697:1656–1673, June 2009.

D. Sijacki, V. Springel, and M. G. Haehnelt. *MNRAS*, 400:100–122, November 2009.

C. Simpson. *MNRAS*, 360:565–572, June 2005.

E. P. Smith and T. M. Heckman. *ApJ*, 348:38–47, January 1990.

R. S. Somerville, P. F. Hopkins, T. J. Cox, B. E. Robertson, and L. Hernquist. *MNRAS*, 391: 481–506, December 2008.

M. Spaans and J. Silk. *ApJ*, 652:902–906, December 2006.

D. N. Spergel, L. Verde, H. V. Peiris, E. Komatsu, M. R. Nolta, C. L. Bennett, M. Halpern, G. Hinshaw, N. Jarosik, A. Kogut, M. Limon, S. S. Meyer, L. Page, G. S. Tucker, J. L. Weiland, E. Wollack, and E. L. Wright. *Astrophys. J. Suppl.*, 148:175–194, September 2003.

D. N. Spergel, R. Bean, O. Doré, M. R. Nolta, C. L. Bennett, J. Dunkley, G. Hinshaw, N. Jarosik, E. Komatsu, L. Page, H. V. Peiris, L. Verde, M. Halpern, R. S. Hill, A. Kogut, M. Limon, S. S. Meyer, N. Odegard, G. S. Tucker, J. L. Weiland, E. Wollack, and E. L. Wright. *Astrophys. J. Suppl.*, 170:377–408, June 2007.

V. Springel, T. Di Matteo, and L. Hernquist. *MNRAS*, 361:776–794, August 2005a.

V. Springel, S. D. M. White, A. Jenkins, C. S. Frenk, N. Yoshida, L. Gao, J. Navarro, R. Thacker, D. Croton, J. Helly, J. A. Peacock, S. Cole, P. Thomas, H. Couchman, A. Evrard, J. Colberg, and F. Pearce. *Nat*, 435:629–636, June 2005b.

A. T. Steffen, A. J. Barger, L. L. Cowie, R. F. Mushotzky, and Y. Yang. *ApJ*, 596:L23–L26, October 2003.

T. Tanaka and Z. Haiman. *ApJ*, 696:1798–1822, May 2009.

R. J. Thacker, E. Scannapieco, and H. M. P. Couchman. *ApJ*, 653:86–100, December 2006.

E. Treister and C. M. Urry. *ApJ*, 652:L79–L82, December 2006.

S. Tremaine, K. Gebhardt, R. Bender, G. Bower, A. Dressler, S. M. Faber, A. V. Filippenko, R. Green, C. Grillmair, L. C. Ho, J. Kormendy, T. R. Lauer, J. Magorrian, J. Pinkney, and D. Richstone. *ApJ*, 574:740–753, August 2002.

Y. Ueda, M. Akiyama, K. Ohta, and T. Miyaji. *ApJ*, 598:886–908, December 2003.

C. M. Urry and P. Padovani. PASP, 107:803–+, September 1995.

R. V. Vasudevan and A. C. Fabian. *MNRAS*, 381:1235–1251, November 2007.

M. Vestergaard. *ApJ*, 571:733–752, June 2002.

M. Vestergaard and P. S. Osmer. *ApJ*, 699:800–816, July 2009.

M. Vestergaard and B. M. Peterson. *ApJ*, 641:689–709, April 2006.

M. Volonteri and M. J. Rees. *ApJ*, 633:624–629, November 2005.

M. Volonteri and M. J. Rees. *ApJ*, 650:669–678, October 2006.

M. Volonteri, M. Sikora, and J.-P. Lasota. *ApJ*, 667:704–713, October 2007.

M. Volonteri, G. Lodato, and P. Natarajan. *MNRAS*, 383:1079–1088, January 2008.

D. A. Wake, S. M. Croom, E. M. Sadler, and H. M. Johnston. *MNRAS*, 391:1674–1684, December 2008.

A. Wandel. *ApJ*, 565:762–772, February 2002.

S. J. Warren, P. C. Hewett, and P. S. Osmer. *ApJ*, 421:412–433, February 1994.

S. D. M. White and C. S. Frenk. *ApJ*, 379:52–79, September 1991.

S. D. M. White and M. J. Rees. *MNRAS*, 183:341–358, May 1978.

C. J. Willott, X. Delfosse, T. Forveille, P. Delorme, and S. D. J. Gwyn. *ApJ*, 633:630–637, November 2005.

C. J. Willott, L. Albert, D. Arzoumanian, J. Bergeron, D. Crampton, P. Delorme, J. B. Hutchings, A. Omont, C. Reylé, and D. Schade. *AJ*, 140:546–560, August 2010a.

C. J. Willott, P. Delorme, C. Reylé, L. Albert, J. Bergeron, D. Crampton, X. Delfosse, T. Forveille, J. B. Hutchings, R. J. McLure, A. Omont, and D. Schade. *AJ*, 139:906–918, March 2010b.

C. Wolf, L. Wisotzki, A. Borch, S. Dye, M. Kleinheinrich, and K. Meisenheimer. A&A, 408:499–514, September 2003.

M. G. Yates, L. Miller, and J. A. Peacock. *MNRAS*, 240:129–166, September 1989.

Q. Yu and Y. Lu. *ApJ*, 689:732–754, December 2008.

Q. Yu and S. Tremaine. *MNRAS*, 335:965–976, October 2002.